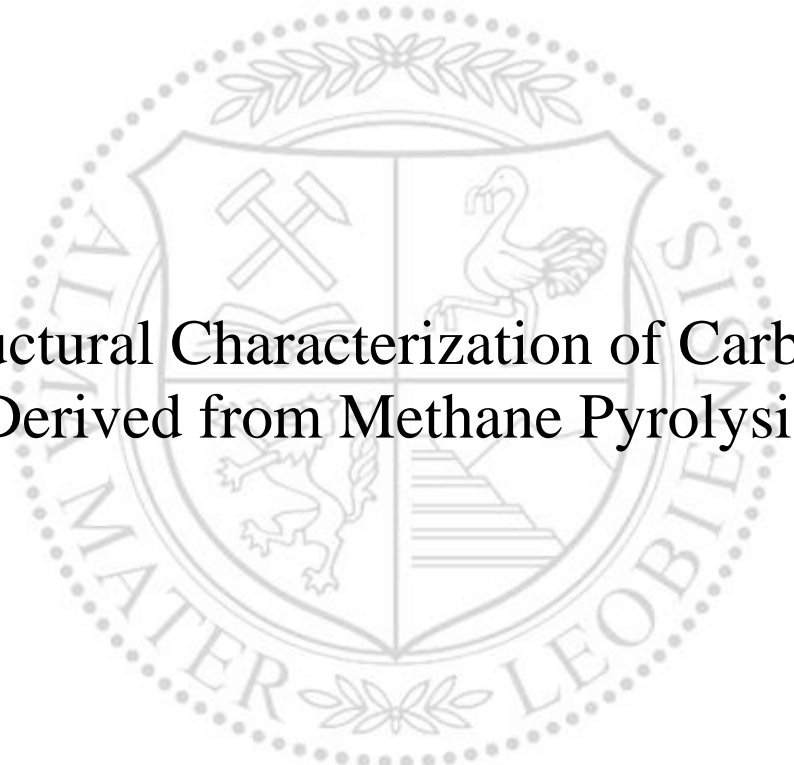




Institute of Physics

Master's Thesis

The background features a large, faint watermark of the University of Leoben seal. The seal is circular and contains a shield with four quadrants: top-left shows crossed hammers, top-right shows a stork, bottom-left shows a rampant lion, and bottom-right shows a staircase. The text 'MONTAN UNIVERSITÄT LEOBEN' is written around the perimeter of the seal.

Structural Characterization of Carbons  
Derived from Methane Pyrolysis

Florian Knabl, BSc

March 2021



**AFFIDAVIT**

I declare on oath that I wrote this thesis independently, did not use other than the specified sources and aids, and did not otherwise use any unauthorized aids.

I declare that I have read, understood, and complied with the guidelines of the senate of the Montanuniversität Leoben for "Good Scientific Practice".

Furthermore, I declare that the electronic and printed version of the submitted thesis are identical, both, formally and with regard to content.

Date 04.03.2021

---

Signature Author  
Florian Knabl

# Acknowledgment

First and foremost, I wish to express my sincere appreciation to my acting co-supervisor Dr.mont. MSc Nikolaos Kostoglou for his endless support at all times.

I wish to express my deepest gratitude to both Univ.-Prof. Mag. et Dr.rer.nat. Oskar Paris and Univ.-Prof. DI Dr.mont. Christian Mitterer for placing their trust on me and for their most valuable contributions to this thesis. Even in times of an ongoing pandemic and social distancing, you were never far away.

Working for two chairs was an outstanding experience as I got to collaborate with many exciting people. My gratitude goes out to Mag. et Dr.rer.nat. Rainer Lechner, Mag. et Dr.rer.nat. Gerhard Popovski, Mohammadtaha Honaramooz, MSc, Sebastian Stock, BSc, Heide Kirchberger and Nadine Aichberger from the Institute of Physics as well as Mag. Velislava Terziyska, Florian Frank, MSc, Yvonne Moritz, MSc, Gerhard Hawranek and Silvia Pölzl from the Chair of Functional Materials and Material Systems.

I would further like to recognize the invaluable contributions made by many colleagues from all around Montanuniversität Leoben. This includes DI Dr.mont. Andreas Egger and DI Dr.mont. Christian Berger from the Chair of Physical Chemistry, DI Dr.mont. Tamara Ebner from the Chair of Nonferrous Metallurgy as well as Univ.-Prof. DI Dr.techn. Johannes Schenk, DI Daniel Ernst, DI Oday Daghagheleh, DI Dr.mont. Daniel Spreitzer, and DI Dr.mont. Peter Presoly from the Chair of Ferrous Metallurgy.

I would like to thank DI Markus Mitteregger, MBA and his team from RAG Austria AG. My thesis contributes only a small part to the overall research project, which would not have been possible without their support and funding. Furthermore, I would like to acknowledge DI Robert Obenaus-Emler for managing the project here at the Montanuniversität Leoben.

Finally I would like to thank my girlfriend Johanna as well as my friends Tobias, Maximilian, Michael, and Pia for their invaluable support.

# Abstract

The world is currently facing the enormous task of massively reducing the carbon dioxide emissions for energy production within the next decades. Switching to hydrogen as an energy carrier is a possible approach for a sustainable and climate-neutral energy production. Hydrogen may be produced without carbon dioxide emissions by means of methane pyrolysis which yields large quantities of carbon as a complementary product. To allow a large-scale application of methane pyrolysis, this carbon must be put to use. In this thesis, carbons derived from three different laboratory-scaled methane pyrolysis processes were investigated using advanced characterization techniques including X-ray diffraction, small-angle X-ray scattering, gas sorption analysis, thermogravimetric analysis, and Raman spectroscopy.

The carbon phase derived from a liquid metal process utilizing a catalyst of Cu and Ni was reported to be turbostratic carbon. The plasma process yielded a mixture of graphite and turbostratic carbon with a BET area of up to  $75.8 \text{ m}^2 \text{ g}^{-1}$ . Graphite was reported from a fixed bed process using reduced iron ore as a catalyst. Contrary to multiple literature studies no other allotropic forms of carbons were detected, such as graphene, carbon nanotubes or carbon fibers. All carbons contained significant amounts of impurities in a range between 31.4 wt% and 89.7 wt%. Carbon purity must be increased in future studies for the carbon product to be marketable. Many potential high-tech applications of carbon require a nanoporous structure combined with a large specific surface area. This may be achieved in a subsequent activation step and should be investigated in future research.

# Zusammenfassung

Die Welt steht momentan vor der enormen Aufgabe, die Kohlendioxid-Emissionen für die Energieproduktion in den nächsten Jahrzehnten drastisch zu reduzieren. Ein möglicher Ansatz für eine nachhaltige und klimaneutrale Energieproduktion ist ein Wechsel zu Wasserstoff als Energieträger. Wasserstoff kann ohne Ausstoß von Kohlendioxid durch Methanpyrolyse erzeugt werden. Dabei werden große Mengen an Kohlenstoff als Nebenprodukt erzeugt. Um den großflächigen Einsatz der Methanpyrolyse zu ermöglichen, muss dieser Kohlenstoff einer Verwendung zugeführt werden.

In dieser Arbeit wurden Kohlenstoffe aus drei unterschiedlichen Methanpyrolyse-Prozessen unter der Verwendung fortschrittlicher Charakterisierungsmethoden wie Röntgendiffraktometrie, Kleinwinkelstreuung, Gas-Sorptions-Analyse, thermogravimetrische Analyse und Raman-Spektroskopie untersucht.

Bei der Kohlenstoffphase, die aus einem Flüssigmetall-Prozess unter der Verwendung eines Katalysators aus Cu und Ni hergestellt wurde, handelte es sich um turbostratischen Kohlenstoff. Der Plasma-Prozess lieferte eine Mischung aus Graphit und turbostratischem Kohlenstoff mit einer BET-Oberfläche von bis zu  $75.8 \text{ m}^2 \text{ g}^{-1}$ . Unter der Verwendung von reduziertem Eisenerz als Katalysator in einem Festbettreaktor wurde Graphit produziert. Im Gegensatz zu mehreren Literaturarbeiten konnten keine weiteren allotropen Formen von Kohlenstoff wie Graphen, Kohlenstoffnanoröhren oder Kohlenstofffasern, nachgewiesen werden. Alle Kohlenstoffe beinhalten signifikante Mengen an Verunreinigungen in einem Bereich von 31.4 Gew% bis 89.7 Gew%. Die Reinheit der Kohlenstoffe muss in zukünftigen Untersuchungen gesteigert werden, um ein marktfähiges Kohlenstoffprodukt zu erhalten.

Viele mögliche High-Tech-Anwendungen von Kohlenstoff benötigen eine nanoporöse Struktur sowie eine große spezifische Oberfläche. Das kann durch einen nachgelagerten Aktivierungsschritt erfolgen und sollte in zukünftigen Forschungsarbeiten untersucht werden.

# Contents

<b>1</b>	<b>Introduction and Theoretical Background</b>	<b>1</b>
1.1	Hydrogen production by methane pyrolysis . . . . .	2
1.2	Carbons derived from methane pyrolysis . . . . .	4
1.3	Potential applications for carbons derived from methane pyrolysis . . . . .	9
1.4	Experimental methods for carbon characterization . . . . .	11
<b>2</b>	<b>Experimental</b>	<b>19</b>
2.1	Samples . . . . .	19
2.2	Experimental methods . . . . .	21
2.2.1	Optical microscopy . . . . .	21
2.2.2	Powder dispersion studies . . . . .	21
2.2.3	Poured bulk density measurements . . . . .	21
2.2.4	Scanning electron microscopy (SEM) and energy dispersive X-ray spectroscopy (EDS) . . . . .	21
2.2.5	X-ray diffractometry . . . . .	22
2.2.6	Small angle X-ray scattering (SAXS) . . . . .	23
2.2.7	Raman spectroscopy . . . . .	24
2.2.8	Thermogravimetric analysis (TGA) and differential scanning calorimetry (DSC) . . . . .	26
2.2.9	Gas sorption analysis . . . . .	27
<b>3</b>	<b>Results</b>	<b>29</b>
3.1	Results from basic characterization methods . . . . .	29
3.2	Sample morphology and chemical composition . . . . .	31
3.3	Results from X-ray diffraction experiments . . . . .	33
3.4	Results from Raman spectroscopy . . . . .	44
3.5	Results from small-angle X-ray scattering . . . . .	46
3.6	Carbon content and inorganic impurities . . . . .	47
3.7	Gas sorption analysis and BET area . . . . .	50

<b>4 Discussion and Outlook</b>	<b>54</b>
4.1 Discussion of results . . . . .	54
4.2 Improved characterization procedure for future work . . . . .	58
4.3 Outlook . . . . .	61
<b>References</b>	<b>63</b>

# 1 Introduction and Theoretical Background

Climate change is an urgent topic that requires drastic and extensive action in order to keep global warming well below 2 °C as agreed upon in the Paris Agreement [1]. In order to achieve this goal, the European Commission has published the *European Green Deal*, which is a growth strategy that aims to "transform the EU into a fair and prosperous society, with a modern, resource-efficient and competitive economy". The ultimate goal for the European Union is to become climate-neutral by 2050 [2].

One of the key industrial sectors to deliver the Green Deal is the production of "clean" hydrogen ( $H_2$ ), that is produced without emission of greenhouse gases (GHG) like carbon dioxide ( $CO_2$ ). While the European Commission favors electrolysis as the technology of choice to produce hydrogen in the future, other hydrogen production technologies at lower technological readiness levels are considered as well. This includes "hydrogen production from marine algae, from direct solar water splitting, or from pyrolysis processes with solid carbon as side product" [3].

This thesis deals with the solid carbon derived from such a pyrolysis process, in particular methane ( $CH_4$ ) pyrolysis. Methane is a temporary substitute for natural gas, which is supposed to be the raw material for an extensive production of carbon in large-scale industrial applications. Hydrogen is the main product from methane pyrolysis. However, large quantities of carbon arise as a by-product. A sustainable approach should be adapted for utilizing the carbon rather than depositing it.

The goal of this thesis is to fully characterize and understand the products obtained from three different laboratory-scale methane pyrolysis processes developed at Montanuniversität Leoben. The research questions to be answered are: What phases are present in the obtained products? If carbon is present, what carbon allotrope and morphology was obtained? What is the carbon content of the individual samples? What is the specific surface area of the samples? Are the produced carbons nanoporous? In order to answer these questions, a methodology for carbon characterization was developed within this thesis. The research hypothesis is that the three methane pyrolysis processes could yield high-purity carbon products.

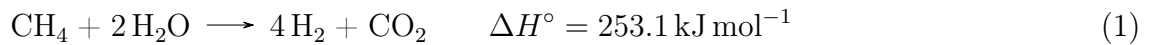
The first chapter of this thesis establishes fundamentals of the methane pyrolysis process. It gives a synoptic overview of carbons as a class of materials as well as their potential applications. The chapter concludes with a brief section on the characterization techniques employed in this thesis. The second chapter describes the samples derived from three different methane pyrolysis processes as well as the associated experimental parameters. The third chapter presents the results and the concluding chapter discusses



the results and gives an outlook on future work.

## 1.1 Hydrogen production by methane pyrolysis

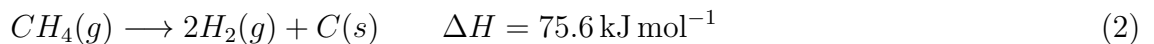
The global annual production of hydrogen was 60 million tons in 2013 [4, 5]. The dominant production process with an annual market share of 40% of the world's H<sub>2</sub> production is the steam methane reforming (SMR) process [6, 7]. Hydrogen is also produced as a by-product of chemical processes such as chlor-alkali production. Water electrolysis represents only a small fraction of total hydrogen production [6, 7]. The SMR process can be expressed using this equation:



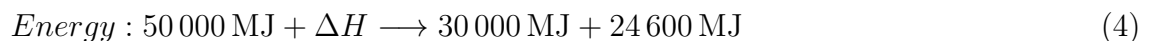
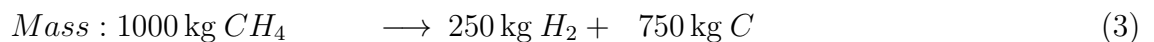
The SMR process yields a significant carbon dioxide footprint per unit of hydrogen produced. Therefore, intense research regarding carbon capture and storage (CCS) - also known as carbon sequestration - is performed to mitigate this challenge [7, 8].

In order to combat climate change non-oxidizing processes need to be employed to obtain large amounts of hydrogen required for a hydrogen economy. One possibility that is investigated is methane pyrolysis, also known as thermal decomposition of methane (TDM), which was investigated heavily in recent years as suggested by multiple review articles released in recent years. [5, 9–16].

Methane decomposition is a moderately endothermic reaction. If there is no catalyst present, temperatures of 1200 °C or higher are required to obtain a reasonable yield. By using a catalyst the temperature required for the process can be significantly reduced [10]. Methane pyrolysis is performed according to the following equation [17]:



Schneider et al. [17] provided the following two equations showing the mass and energy (caloric value-related) on either side of the equation with  $\Delta H = 4600 \text{ MJ}$ :



Judging from the perspective of mass balance, carbon is the main product of this joint production, making up 75% of the total mass. It is reasonable to try to find ways of utilizing the by-product carbon in order to achieve economic viability of the methane pyrolysis process [17].

Various methane pyrolysis processes were suggested in literature and performed in laboratory-scaled experiments. Methane pyrolysis processes may be divided into three main categories with various subcategories according to Fig. 1 [17]. In case of thermal decomposition, high temperatures well above 1200 °C are required. In plasma decomposition processes, very high temperatures beyond 2000 °C are generated using a plasma torch. In case of catalytic decomposition, the catalyst is supposed to decrease the energy barrier for the reaction, causing improved reaction kinetics and allowing to use lower operating temperatures, thereby making the process economically more viable. A common problem with solid catalysts is the blocking of the catalyst (catalyst poisoning) due to the carbon product depositing on the surface of the catalyst [17].

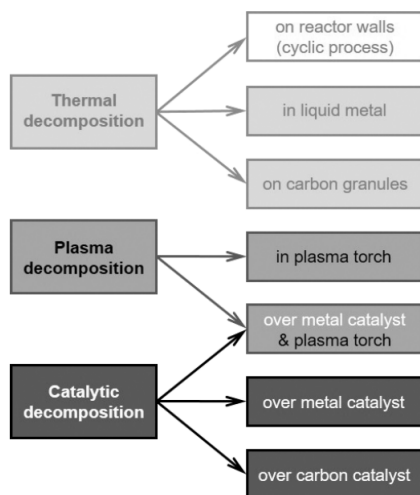


Figure 1: Overview of methane pyrolysis processes. Reproduced from Schneider et al. [17] (CC BY-NC-ND 4.0, no modifications were made).

It should be noted that most theoretical considerations and laboratory-scale experiments only consider methane as a gaseous source for producing hydrogen and carbon. The potential industry-scale feedstock is natural gas, which consists of a mixture of different hydrocarbons (including methane) and possibly impurities like nitrogen, carbon dioxide, and hydrogen sulfide. Using natural gas instead of methane would cause side-reactions that would influence all major parameters of the process. Therefore, results obtained from experimental setups utilizing pure methane should not be directly compared to the ones derived for natural gas [17].

## 1.2 Carbons derived from methane pyrolysis

This chapter gives an overview of the chemical element carbon along with the most important carbon allotropes. In the second part of this chapter the state of the art regarding carbons derived from methane pyrolysis is reviewed.

Carbon is the most versatile element in the periodic table. It can be found in 95% of all known chemical compounds. Carbon is the cornerstone of organic chemistry as it is able to form long chains and bonds readily to elements that may be more or less electronegative compared to carbon.

Pure carbon displays an enormous diversity. The most famous carbon allotropes are diamond and graphite. These two materials are very different from each other with the first one being extremely hard, an electrical insulator, and transparent while the latter is soft, electrically conducting, and has a shiny black color. Many other forms of carbon allotropes, including amorphous carbon, carbon nanotubes, graphene, and fullerenes exist. An overview is given in Fig. 2 [18].

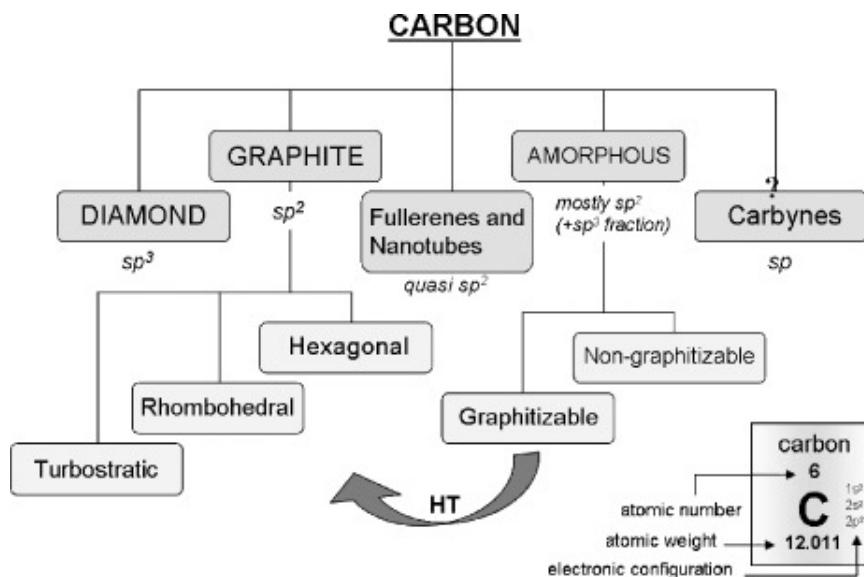


Figure 2: Allotropes of the element carbon. Reprinted with permission from Falcao [18, 19]; copyright 2007 Journal of Chemical Technology & Biotechnology.

Diamond is a carbon allotrope based on  $sp^3$ -hybridized bonding. In this type of bonding each carbon atoms bonds covalently to the three atoms surrounding it, thus forming a three-dimensional array of tetrahedrons. The angle between the bonds is  $109.5^\circ$ . This gives rise to the diamond structure, a specific type of a cubic unit cell [18].

Single-layer graphene is the newest member in the family of carbon allotropes [20, 21]. Single-layer graphene, or simply graphene, is made up of a basic two-dimensional hexagonal lattice of  $sp^2$ -hybridized carbon atoms. A small number of graphene layers

stacked on top of each other are referred to as few-layer graphene.

Graphite consists of flat layers of graphene stacked on top of each other. Within the layers carbon atoms are bonded covalently using  $sp^2$ -hybridized bonds. Each carbon atom bonds to three other carbon atoms within the layer thus forming a hexagonal pattern. The un-hybridized  $2p_z$  orbital forms a delocalized  $\pi$  bond, which gives rise to outstanding electric and thermal conductivity within the layer. Weak Van der Waals forces are acting between the layers. The crystal structure of graphite is the hexagonal crystal structure. In this case, graphene layers are stacked on top of each other in a regular ABABAB sequence with a defined interlayer distance  $d_{002}$  of 3.354 Å (see Fig. 3) [22]. The rhombohedral form of graphite features an ABCABC stacking sequence.

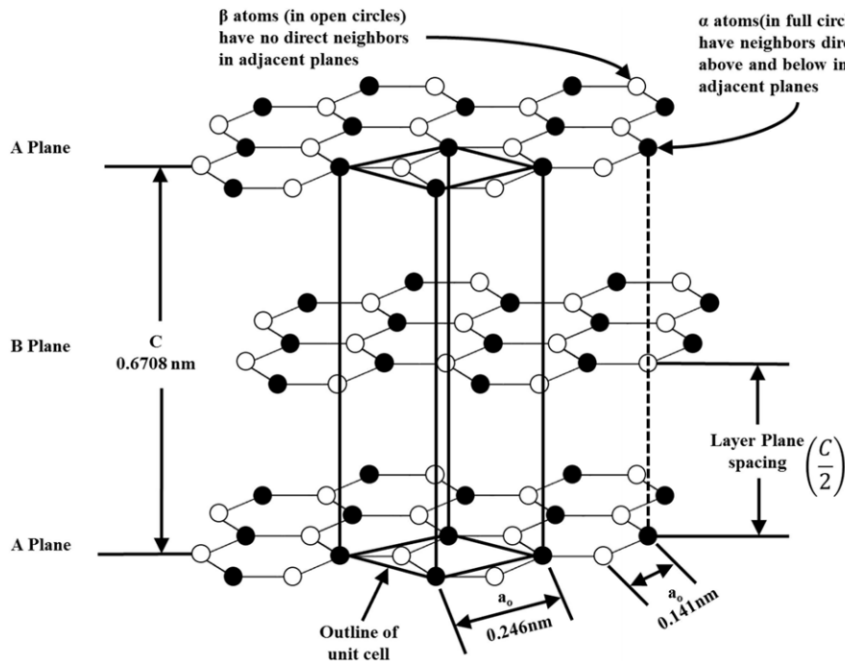


Figure 3: Crystal structure of hexagonal graphite. The ABABAB stacking sequence as well as the unit cell are depicted. Reprinted with permission from Delhaes [22]; copyright 2001 Taylor & Francis Informa UK Ltd - Books.

Turbostratic carbon is a special type of carbon in which graphene layers are not stacked in an ordered fashion, but relative rotations and translations between adjacent layers exist. Turbostratic carbon must not be confused with graphite. Turbostratic carbon features an increased interlayer distance compared to hexagonal graphite [18]. This property should, however, not be used to classify between graphite and turbostratic carbon [23]. As discovered by Warren [24], turbostratic carbon only shows in-plane reflections of the type  $(hk0)$  and reflections from the stacking order of the type  $(00l)$ .

Crystallographic parameters used to describe graphite and turbostratic carbons include the crystal length  $L_a$  which is the average crystal length in the a-direction of the

unit cell, so in in-plane direction. Another parameter is the crystal length  $L_c$  which describes the average crystal length in the stacking direction, so along the c-direction of the unit cell. The interlayer distance  $d_{002}$  describes the average stacking distance between graphene sheets. Turbostratic carbon displays an increased interlayer distance  $d_{002}$  compared to graphite. This parameter should, however, not be used to classify between turbostratic carbon and graphite [23]. The crystallographic parameters of a graphitic crystallite are summarized in Fig. 4 [25].

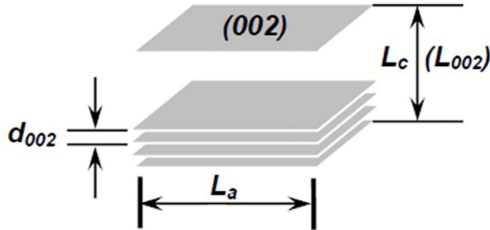


Figure 4: Crystallographic parameters of a schematic graphitic crystallite. Reproduced from Silva et al. [25] (CC BY-NC-ND 4.0, no modifications were made).

Fullerenes are a class of molecules including the  $C_{60}$  and the  $C_{70}$  molecules. They consist of both hexagons and pentagons of carbon atoms. The discoverers of the  $C_{60}$  molecule named it Buckminsterfullerene after the architect Buckminster Fuller, who designed geodesic domes with a similar geometry to the  $C_{60}$  molecule. The geometry of a  $C_{60}$  molecule reminds of a soccer ball, resulting in the informal name buckyball.

A single graphene sheet may be rolled into a cylindrical shape to form a carbon nanotube (CNT). Both single-walled carbon nanotubes (SWCNT) and multi-walled carbon nanotubes (MWCNT) are reported in literature. CNTs may be open-ended or closed-ended. The later was found to consist of fullerene-like caps. The smallest diameter reported in a SWCNT corresponds to the diameter of the  $C_{60}$  molecule, the most common type of fullerene molecules. Both fullerenes and carbon nanotubes, while based on the two-dimensional  $sp^2$ -hybridized graphene sheet, do not consist of pure  $sp^2$  bonds [18].

Amorphous carbons consist mostly of  $sp^2$ -hybridized carbon atoms along with a significant amount of  $sp^3$  carbon atoms. There is a lack of long-range ordering. Amorphous carbons are usually prepared through pyrolysis of organic polymers or hydrocarbon precursors at temperatures below 1500 °C [18]. It has to be noted that there is no clean distinction in literature between turbostratic carbon and amorphous carbon.

Amorphous carbons may be categorized into "soft carbons" and "hard carbons". Soft carbons develop a graphitic structure while heating from 1500 °C to 3000 °C and are subsequently known as graphitizable carbons. This is possible due to low amounts of crosslinking between oriented areas of  $sp^2$  sheets. Soft carbons are commonly derived

from liquid or gaseous precursors and include carbons from petroleum pitch, some carbon fibers and carbon black [18]. Hard carbons have a highly disordered structure with mostly isotropic properties <sup>1</sup>. These carbons do not develop a graphitic structure even at prolonged heat treatments at 3000 °C and are thus referred to as non-graphitizable carbons. They originate from solid precursors like polymers (e.g. Polyacrylonitrile), resins, and biomass. Examples include most activated carbons as well as biochars [18].

Various types of carbon may be obtained from natural resources (mineral graphite), through pyrolysis (i.e. carbon black), chemical vapor deposition (pyrolytic graphite) or through sputtering (diamond-like carbon coatings). Organic precursors include methane, various hydrocarbons, rayon, petroleum fractions, and plant-based carbons. Polyacrylonitrile is the most frequent precursor for carbon fiber production [26].

As seen in Eq. 2 and Eq. 3, hydrogen and carbon are the products of the methane pyrolysis process. Separation of hydrogen and carbon is easy due to the gaseous nature of hydrogen. Describing the quality of the hydrogen product may be done by analyzing the purity of the gas. Assessing the quality of the carbon is a more demanding task. The morphology of the carbon depends strongly on reaction conditions like temperature and catalyst used. Keipi et al. [5] provided a comprehensive literature review on this topic. Fig. 5 is a graphical representation of the main type of carbon product obtained from the methane pyrolysis process as a function of the catalyst type and the reaction temperature. Various carbon products including graphite-like carbon (graphite), carbon black, amorphous turbostratic carbon, nanotubes and filamentous carbon were reported [5]. Metal-based catalysts tend to yield filamentous carbon structures, while thermal decomposition yields carbon black or graphite. Metal catalysts were used in conjunction with the lowest process temperatures, carbon-based catalysts were employed at intermediate temperatures and processes without catalysts utilized the highest temperature ranges. However, as seen in Fig. 5, temperature regions overlap [5]. It has to be noted that Fig. 5 is a strongly simplified representation as catalyst performance is strongly influenced by the method of catalyst synthesis, the nature of the catalyst support material, the amount of active metal catalyst, and the catalyst particle size [5, 11].

As the samples investigated within this thesis were derived from three particular methane pyrolysis processes, a more in-depth literature review of the liquid metal process, the plasma-assisted process and the fixed bed process using an Fe-based catalyst is given.

The **liquid metal methane pyrolysis process** was first mentioned in a patent

---

<sup>1</sup>One notable exception are Polyacrylonitrile-based carbon fibers that are hard carbons, yet highly oriented and thus not isotropic. Cellulose fibers are another example of highly ordered carbons. The order of the carbon does not only depend on the precursor, but also on the processing during production (e.g. stretching of fibers during the high temperature pyrolysis).

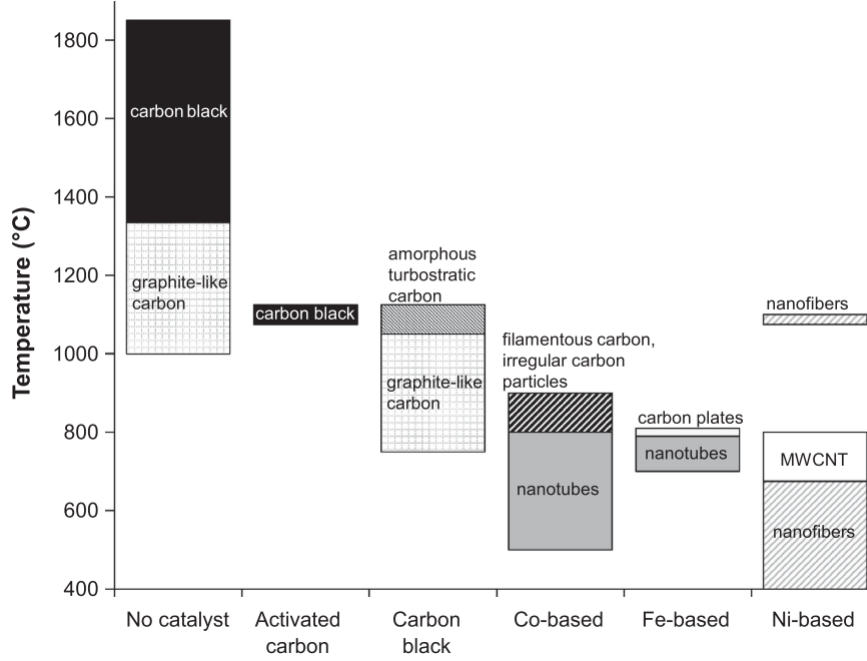


Figure 5: Graphical representation of the main type of carbon product obtained from the methane pyrolysis process as a function of catalyst type and reaction temperature. It has to be noted that in most cases the catalyst particles were small ( $\mu\text{m}$  and sub- $\mu\text{m}$  scale). Reproduced with permission from Keipi et al. [5]; copyright 2016 Elsevier Ltd.

by Tyrer in 1931 suggesting liquid iron as the molten metal [27]. In 1999, Steinberg suggested a metal bath process utilizing tin [28]. Subsequently, multiple studies were conducted using liquid tin [29–32]. Further molten metals that were investigated include Ga [33], Mg [34], multiple mixtures of different metals, in particular Ni-Bi [35], a mixture of Cu-Bi [36], Pb [29, 37], a mixture of Pb-Bi [37], and a mixture of Ni-Bi with a salt layer on top of the metal bath [38]. Concepts utilizing salt baths including  $\text{MnCl}_2\text{-KCl}$  [39] and mixtures of  $\text{MnCl}_2\text{-KCl}$  with iron [40] were proposed. Most studies focus on the effect of the molten bath on the reaction kinetics and subsequently include rather brief sections on carbon characterization or none at all [28, 31, 32, 36]. Reviews on the topic were given by Parkinson et al. [14] and Parfenov et al. [15].

A **plasma-assisted process** for the co-production of hydrogen and carbon black via cracking of methane was first proposed by Fulcheri and Schwob in 1995 [41]. Multiple studies on similar plasma-assisted processes with a methane feedstock reported carbon black [42–44], carbon nanotubes [45], nanostructured sheet-like carbons [46], nano carbon powders [47], amorphous carbon aerosols [48], few-layer graphene nanosheets [49], graphene flakes [50], and well-defined spherical carbon particles [51]. Some papers focused on plasma process parameters and did not characterize the carbon product [52, 53]. In 2009, Muradov et al. reported light and fluffy carbon aerosols with a sponge-like microstructure and a BET area of up to  $150\text{ m}^2\text{ g}^{-1}$  using a non-thermal plasma [48]. In

2015, Zhang, Cao, and Cheng reported a radio-frequency induction thermal plasma process yielding few-layer graphene nanosheets [49]. It has to be noted, however, that this research focused on the production of few-layer graphene rather than a co-production of hydrogen and solid carbon. In 2020, Shavelkina et al. reported graphene flakes synthesized in a plasma jet created by a DC plasma torch [50]. Similarly to some earlier studies, Shavelkina et al. did not focus on hydrogen production.

Multiple **fixed bed methane pyrolysis processes** using Fe-based catalysts were described in the literature [54–60]. In 2001, Shah, Panjala, and Huffman reported the co-production of hydrogen and carbon based on methane pyrolysis in a fixed bed reactor using Fe-based catalysts on  $\text{Al}_2\text{O}_3$  [54]. For process temperatures of 700–800 °C, carbon nanotubes nucleated by Fe nanoparticles were reported. For 900 °C amorphous carbon, carbon flakes, and carbon fibers were reported. Konieczny et al. prepared an Fe-based catalyst for methane pyrolysis through reduction of magnetite ( $\text{Fe}_3\text{O}_4$  for subsequent application in a fixed bed reactor [55]. The experiments were conducted between 800 and 900 °C and yielded carbon nanofibers. In 2011, Pinilla et al. reported on methane pyrolysis experiments conducted in a fixed bed reactor utilizing Fe-based catalysts on  $\text{Al}_2\text{O}_3$  and MgO [56]. For temperatures around 700 °C carbon nanotubes were reported. For increased temperatures of 800 °C carbon nanofilaments and graphitic carbon was reported. Awadallah et al. reported multi-walled carbon nanotubes derived from a fixed bed methane pyrolysis process using MgO catalysts covered with mixtures of Fe, Ni, and Co [57]. Pudukudy and Yaakob published two studies on Fe-based catalysts for methane pyrolysis. The first study utilized Fe-based catalyst supported on  $\text{SiO}_2$  microflakes and yielded aggregated graphene sheets [58]. The second study reported graphene sheets with a fluffy appearance synthesized using Fe and Ni on MgO nanoparticles [59]. In 2020, Torres, Pinilla, and Suelves reported on methane pyrolysis experiments using Fe-Co on  $\text{Al}_2\text{O}_3$  as catalyst [60]. Multiple studies claimed that the catalyst performance was influenced by multiple factors including catalyst particle size, catalyst support, and the type of catalyst (e.g. metal) used [5, 11].

### 1.3 Potential applications for carbons derived from methane pyrolysis

According to Eq. 4, large amounts of the heating value of  $\text{CH}_4$  are not utilized. When using methane or natural gas as fuel, this heating value is released and  $\text{CO}_2$  is produced. In case of methane pyrolysis, the heating value not utilized must be compensated somehow. There are two basic options in this direction: The first option is an economic benefit due to reduced costs for  $\text{CO}_2$  emissions in case a  $\text{CO}_2$  tax is introduced or  $\text{CO}_2$  allowances have



to be purchased. Alternatively, the carbon product may be sold to make the methane pyrolysis process economically more viable [5]. The second path is investigated in this chapter.

Carbon selling prices for various carbon products are depicted in Fig. 6 along with the hydrogen selling price as a function of the carbon selling price for both methane pyrolysis (TCD - thermocatalytic decomposition) and steam methane reforming (SMR) [7]. The break-even point for methane pyrolysis is reached at a selling price of \$350/ton carbon. In 2008, Muradov and Veziroglu [7] reported selling prices of \$310-460/ton for metallurgical coke, and significantly higher selling prices for various other forms of carbon as depicted in Fig. 6 [7]. Keipi et al. reported prices of €500-4000/ton for carbon black, €1500/ton for activated carbons, €200-400/ton for industrial-grade MWCNTs and €150/ton for metallurgical coke in 2016 [5].

In 2008, Muradov and Veziroglu [7] estimated that the "annual worldwide consumption of all carbon products amounts to only 15 - 20 million tons, and it is unlikely that there will be any dramatic increase in these traditional carbon utilization areas in the near future". In 2016, Keipi et al. reported significantly larger annual production volumes of different types of carbon compared to Muradov and Veziroglu: 8.1 - 9.4 million tons of carbon black, 1.9 million tons of activated carbon, 500 million tons of metallurgical coke. An estimate of 12000 tons of carbon nanotubes for 2016 was given [5]. If the global annual hydrogen production of 60 million tonnes in 2013 were to be replaced by the methane pyrolysis process, 180 million tonnes of carbon would be produced based on Eq. 2 [4, 5]. The individual markets for those carbon products are significantly smaller than the 180 million tons of possible carbon product, except for metallurgical coke. The latter would, however, cause the emission of CO<sub>2</sub> in the metallurgical reduction step of metal production [5].

Due to the limited sizes of current carbon markets, new applications for the pyrolysis-derived carbons are required. Possible applications include building or construction materials, direct carbon fuel cells, and soil amendment (i.e. substitute for biochar) [5]. The International Biochar Initiative defines biochar as a solid material produced from organic feedstock carbonization [61]. Typical feedstocks include wood, plant leaves, and crop residue [62]. Potential structural applications for carbons derived from methane pyrolysis include carbon-carbon composites and carbon fiber composites. Carbon-based products may be used as an additive for cement [7]. This could yield large reductions in CO<sub>2</sub> emissions currently caused by the cement required for concrete production. Potential high-tech applications include materials for electrochemical energy storage, water purification, selective gas separation and gas storage. All these applications require a nanoporous structure

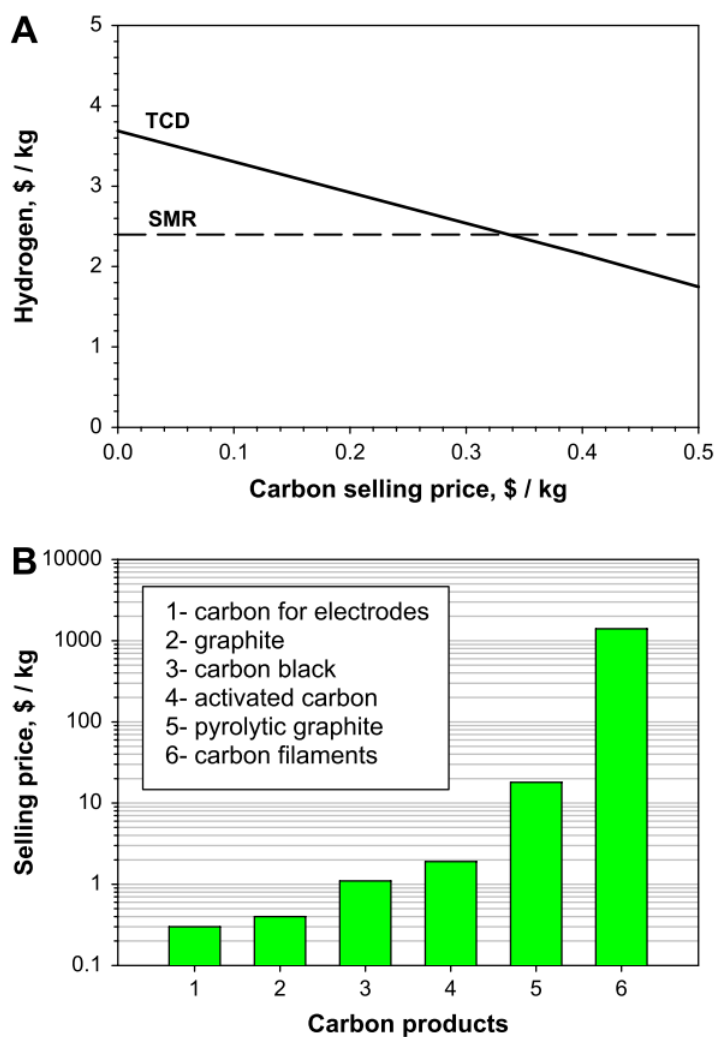


Figure 6: Economics of hydrogen production through steam methane reforming (SMR) and methane pyrolysis (thermocatalytic decomposition - TCD), based on natural gas. (A) hydrogen selling price as a function of carbon selling price; (B) selling price of different carbon products as reported in 2008. Reproduced with permission from Muradov and Veziroglu [7]; copyright 2008 International Association for Hydrogen Energy.

with a large specific surface area [11, 63, 64]. This might be achieved in a subsequent activation step. In case a  $\text{CO}_2$  tax were to be implemented, it might be economically viable to not utilize the carbon at all, and consequently deposit it as waste.

#### 1.4 Experimental methods for carbon characterization

The aim of this chapter is to give a brief summary of the theoretical background of the experimental methods employed to characterize the carbons investigated in this thesis. The list of techniques includes:

- scanning electron microscopy (SEM)

- energy-dispersive X-ray spectroscopy (EDS)
- X-ray diffraction (XRD, also referred to as wide angle X-ray scattering (WAXS))
- small angle X-ray scattering (SAXS)
- Raman spectroscopy
- gas sorption analysis
- differential scanning calorimetry (DSC) combined with thermogravimetric analysis (TGA)

An excellent review of scanning electron microscopy and energy-dispersive X-ray spectroscopy is given by Goldstein et al. [65]. The following two paragraphs strongly follow the content given in this book. **Scanning electron microscopy (SEM)** is a technique that creates magnified images which reveal microscopic-scale information on the size, shape, composition, and other properties of a specimen. The basic operation principle of a scanning electron microscope involves the creation of a finely focused beam of energetic electrons emitted from an electron source. The energy range of the electrons in such a beam is typically between 0.1 and 30 keV. After emission from the the source and acceleration to a high energy, the electron beam diameter is reduced and the focused beam scans the specimen in a raster pattern. The electron beam is modified by apertures, magnetic and/or electrostatic lenses, and electromagnetic coils. The interaction of the electron beam with the specimen yields either high-energy backscattered electrons (BSEs) or low-energy secondary electrons (SEs). Both types of electrons escape the surface and are subsequently measured in specific detectors. For each individual raster scan location, the detected intensity is used to determine the gray level at the corresponding location, thus forming an individual pixel. The specimen must be placed in a vacuum to minimize unwanted scattering of beam electrons as well as BSEs and SEs with atoms and molecules of atmospheric gases. Furthermore specimen must have a minimum electric conductivity to avoid the accumulation of charge on the specimen surface. If the specimen is electrically insulating, a conductive coating must be applied prior to the measurement [65].

**Energy-dispersive X-ray spectroscopy (EDS)** is an analytical technique for elemental analysis of specimen. The interaction of an electron beam with the specimen produces an X-ray spectrum consisting of two contributions. The first contribution are characteristic X-rays, whose specific energies provide a fingerprint specific to each element. The presence of H and He cannot be determined using EDS, as the energy of the

characteristic X-rays of these two elements is too low to be detected. The second contribution stems from continuum X-rays, which form a background beneath the characteristic X-rays. Quantitative analysis presents significant challenges because of mutual peak interferences that can occur between certain combinations of elements [65]. Consequently, EDS was used qualitatively rather than quantitatively within this thesis.

XRD and SAXS are both scattering techniques utilizing a single wavelength of X-rays as an incident beam. The intensity of the diffracted beam is recorded as a function of the scattering angle, or more generally, the scattering vector. In practice the most important difference is the length scale that is investigated using these techniques. XRD allows to investigate matter on the atomic scale ( $10^{-10}$  m) in order to determine properties like the crystal structure of a given material, while SAXS allows to investigate properties of nanometer-sized structures, commonly in the range of 1 to 100 nm.

In **X-ray diffraction**, scattering of the incident beam occurs on different crystallographic planes of the crystal. Constructive interference of the scattered beams into specific directions occurs when the Bragg condition is fulfilled according to Eq. 5 [66]. In this equation,  $n$  is a positive integer number,  $\lambda$  is the wavelength of the X-rays,  $d$  is the interplanar distance, and  $\theta$  is the angle of incidence with respect to the diffraction plane. The angle between the diffracted beam and the transmitted beam is always  $2\theta$  and known as the diffraction angle [66]. Typical diffraction angles recorded during an XRD experiment range from  $10^\circ$  to  $100^\circ$ . For more extensive information on XRD, the interested reader is referred to an excellent textbook on the fundamentals of X-ray diffraction written by Cullity [66] or to a book written by Zolotoyabko [67].

$$n\lambda = 2d \sin(\theta) \tag{5}$$

In **small angle X-ray scattering**, the scattering vector  $\vec{q}$  is used to present data rather than the scattering angle  $\theta$ . The transformation into  $q$  space is performed according to Eq. 6 [68]. This yields a description that is independent of the wavelength of the incident beam. Both descriptions (using the scattering angle  $\theta$  or the length of the scattering vector  $q$ ) are equivalent and may be converted into each other. Typical scattering angles in SAXS experiments range from  $0.1^\circ$  to  $10^\circ$ .

$$q = |\vec{q}| = \frac{4\pi \sin(\theta)}{\lambda} \tag{6}$$

In order to obtain a SAXS signal there must be at least two phases present that exhibit a difference in electron density (e.g. a metal matrix with precipitates or any matrix material with a pore structure). Measurement data is typically presented as intensity over

the length of the scattering vector  $q$ . Once the sample is measured, the two-dimensional intensity data is analyzed. In case of isotropic samples the scattering may be described equivalently using a one-dimensional scattering profile. The scattering background is subtracted prior to the actual data interpretation. More details on the SAXS data measured in this thesis is given in chapter 2.2.6. Since SAXS is a quite sophisticated technique, the interested reader is referred to the books written by Glatter and Kratky [69], Feigin and Svergun [70], and Schnablegger and Singh [68] for a more comprehensive review of the topic.

**Raman spectroscopy** is a spectroscopic technique typically used to determine vibrational modes of molecules and solid materials. It is often applied to measure structural "fingerprints" by which molecules may be identified. A quantitative analysis is also possible as shown in chapter 2.2.7. When light interacts with matter, elastic and inelastic scattering effects may occur. In case of inelastic Raman scattering, the scattered photon can be of either lower (Stokes Raman scattering) or higher (anti-Stokes Raman scattering) energy than the incoming photon [71]. This change in energy corresponds to a change in the wavelength of the outgoing photon. The shift in wavelength is converted to the so-called Raman shift  $\Delta\tilde{\nu}$  according to Eq. 7, where  $\lambda_0$  is the wavelength of the incoming photon and  $\lambda_1$  is the wavelength of the outgoing photon. Measurement data is usually presented as intensity over Raman shift  $\Delta\tilde{\nu}$ . The Raman shift  $\Delta\tilde{\nu}$  is usually given in units of  $\text{cm}^{-1}$ .

$$\Delta\tilde{\nu} = \left( \frac{1}{\lambda_0} - \frac{1}{\lambda_1} \right) \quad (7)$$

Interpretation of Raman spectra for carbon is based on three typical features known as the G, D, and G'(2D) bands, which lie around 1560, 1360 and 2700  $\text{cm}^{-1}$ , respectively. In strongly simplified terms, the G peak is related to C-C stretching within the graphene plane, while the D peak is related to defects and would not occur at all, if the material were to lack any kind of defects within infinitely extended graphene layers. Detailed theoretical derivations and extensive explanations on the topic are given by Ferrari and Robertson and Ferrari [72, 73]. Several papers deal with the actual interpretation of Raman spectra of various carbon-based materials [74–78]. An excellent summary of experimental data is given by Cuesta et al., ranging from disordered to highly ordered samples [79]. The ratio of the D/G band intensities is commonly used to estimate the crystallite size  $L_a$  in carbons [74, 80]. The main feature in the second-order overtone is labeled G'(2D) band in this thesis. For highly ordered materials this band may split into two separate bands [79]. According to Cuesta et al. there is "no second-order spectrum present and the first-order one are approximately equivalent and overlap" for turbostratic materials [79].

**Gas sorption analysis** is an important method for the characterization of porous solids and fine powders. The term adsorption is defined as the enrichment of molecules, atoms and ions in the close vicinity of an interface [81]. When the molecules of the adsorptive penetrate the surface layer and enter the structure of the bulk solid, the term absorption is used. A clear distinction between those two cases is not always possible. The term sorption is more generalized and describes both phenomena [81].

During a gas sorption experiment, the total amount of gas adsorbed is measured as a function of pressure  $p$  or relative pressure  $p/p_0$ , where  $p_0$  is the saturation vapor pressure of the bulk gas at the adsorption temperature. If the experiment is performed at a temperature below the critical point of the gas, the relative pressure  $p/p_0$  is used rather than absolute values of pressure. This is the case for the most common type of experiment which is  $N_2$  adsorption/desorption at 77.3 K. The goal of the experiment is to measure the adsorption and desorption isotherms. Based on this data, various methods may be employed to determine the adsorbed amount, the specific surface area, and the pore size distribution of a given sample.

As described by Thommes et al. [81], a static volumetric method was used to perform the gas sorption experiments in this thesis. In this method, a defined amount of gas (the adsorbate) is released into a confined volume containing the sample. While adsorption of gas molecules on the external sample surface and the internal pore structure takes place, the pressure drops until an equilibrium is established. Based on the difference in pressure before and after adsorption, the amount of adsorbed gas can be calculated using the ideal gas law. In the case of  $N_2$  experiments, this is performed for various pressures until a pressure slightly below the saturation vapor pressure is reached. The whole procedure is performed at a constant temperature. The *dead space* inside the confined volume known as *sample cell* is determined prior to the actual measurement using helium. Prior to the determination of an adsorption isotherm, all physisorbed species attached to the surface of the sample should be removed. This is achieved by outgassing the sample at elevated temperatures under vacuum for a defined amount of time. A typical outgassing procedure for carbons is performed at 250 °C for 24 h [82]. Other gases used besides nitrogen at 77 K include argon at 87 K and carbon dioxide at 273 K. The later is a suitable choice for carbonaceous materials (e.g. biochar) with very narrow micropores and complex pore networks. Krypton at 77 K is another choice for non-porous materials [81].

In the context of physisorption, pores are classified according to their pore width. A *nanopore* is defined to be smaller than 100 nm. Porous materials are further classified into three categories according to their size. Macroporous materials consist of pores with a pore width larger than 50 nm. Mesoporous materials contain pores in the pore width

range of 2-50 nm. Microporous materials consist of pores with a pore width below 2 nm. Micropores can be further classified into super-micropores with widths between 0.7-2 nm and ultra-micropores with widths smaller than 0.7 nm.

The International Union of Pure and Applied Chemistry (IUPAC) provides a classification for adsorption isotherms, which are closely related to the pore structure of the material [81]. This is depicted in Fig. 7. Type I isotherms are given by microporous solids for which micropore filling of narrow micropores of molecular dimensions occurs at a very low relative pressure  $p/p_0$ . Type II isotherms are given by physisorption of gases on non-porous materials. Adsorption in such materials occurs through unrestricted monolayer-multilayer adsorption up to high  $p/p_0$ . Type IV isotherms correlate with mesoporous adsorbents. Capillary condensation gives rise to the shape of the adsorption isotherm. At low  $p/p_0$ , a monolayer is formed on the mesopore walls followed by pore condensation. This is a phenomenon, whereby a gas condensates to a liquid-like phase in a pore at a pressure  $p$  less than the saturation pressure  $p_0$  of the bulk liquid [83]. Capillary condensation may or may not be accompanied by a hysteresis loop. More details on this phenomenon is given by Thommes et al. [81].

The Brunauer-Emmett-Teller (BET) method is commonly used to determine the specific surface area of a given material. The method is based on the physical adsorption of gas molecules on a solid surface. The theoretical background of the BET method has several weaknesses, as it is only applicable to multilayer adsorption and requires gases, that do not chemically react with the surface groups. Further assumptions that the BET method is based on include that the adsorption occurs on a homogenous surface, that no lateral interactions between gas molecules occur, that the upper layer is in an equilibrium with the gas phase, and that the number of layers becomes infinite at the saturation pressure. Therefore, the area determined using the BET method is called BET area rather than specific surface area. The BET method consists of two steps. In the first step the physisorption isotherm is transformed into the BET plot according to Eq. 8. To determine the monolayer capacity  $n_m$ , the linear region of this plot is used, which typically lies within a relative pressure range of 0.05 - 0.30 for non-porous, macroporous and mesoporous materials. The relative pressure range is typically shifted to lower values for microporous materials. The parameter  $n$  is the specific amount adsorbed at the relative pressure  $p/p_0$  and  $C$  is the BET constant.

$$\frac{p/p_0}{n(1 - p/p_0)} = \frac{1}{n_m C} + \frac{C - 1}{n_m C} (p/p_0) \quad (8)$$

In a second step, the BET area  $a_s(BET)$  is calculated using the molecular cross-sectional area  $\sigma_m$  of the adsorbate molecule (e.g. 126 nm<sup>2</sup> for nitrogen at 77 K) according to Eq. 9,

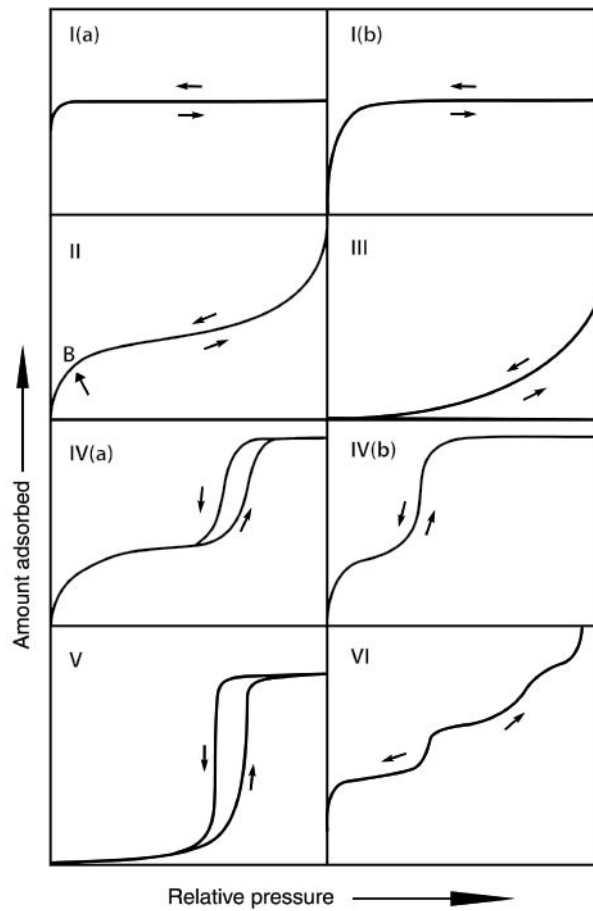


Figure 7: Classification of physisorption isotherms according to the IUPAC Technical Report published in 2015 [81]. Reproduced with permission from Thommes et al. [81]; copyright 2015 De Gruyter.



where  $m$  is the sample mass and  $N_A$  is the Avogadro constant [81].

$$a_s(BET) = \frac{n_m N_A \sigma_m}{m} \quad (9)$$

Novel procedures were developed to allow accurate and comprehensive pore structural analysis. These advanced procedures include Density Functional Theory (DFT) kernels and Grand Canonical Monte Carlo (GCMC) simulations to determine particularly pore size distributions over a wide range of pore sizes [81].

**Differential scanning calorimetry (DSC)** is a thermoanalytical technique in which the difference in the amount of heat required to increase the temperature of a sample and a reference crucible is measured as a function of temperature [84]. The heat flow is measured indirectly and is proportional to the difference in temperature between the sample and a reference. Depending on the sign of the heat difference, the heat flow may be exothermal or endothermal. Measurements may be performed in inert atmosphere or vacuum which allows to determine phase transformations. Synthetic air may be used in order to determine the oxidization behavior of the sample (e.g. exothermal reaction due to formation of gaseous CO<sub>2</sub>) [84]. **Thermogravimetric analysis (TGA)** is a technique where the mass change of a sample is measured as a function of temperature, while the sample is subject to a controlled temperature program in a controlled atmosphere. It is commonly used to study polymeric materials and the oxidation behavior of metals. In this thesis, it is mostly used to determine the volatile fractions of powders in an oxidizing atmosphere. The measurement data obtained in DSC and TGA experiments depends on the total amount of sample mass due to kinetic effects. Sample mass should therefore be kept in a similar range to maintain comparability between measurements [85].

## 2 Experimental

The aim of this chapter is to give the reader an overview of the samples and the techniques used to perform the characterization of the samples. The synthesis of the samples is not described in detail, as the methane pyrolysis processes utilized at Montanuniversität Leoben were performed by research groups at the Institute of Non-Ferrous Metallurgy and the Institute of Ferrous Metallurgy. Those processes will be described in theses and papers in the future to come.

### 2.1 Samples

Various carbon-rich powder samples were investigated within this thesis. Two powders served as reference materials. Sample R1 is a mineral graphite produced by Grafitbergbau Kaisersberg GmbH (GBKB). Sample R2 is biochar that was produced through pyrolysis of biomass by Sonnenerde GmbH. Based on the available data provided by the manufacturer, R1 contains a carbon content of 40 to 50 wt% and an ash content of 48 to 58 wt%<sup>2</sup>. The plant-based biochar was produced through a pyrolysis process at 600 °C in the absence of oxygen. The carbon content was stated to be 69 wt%<sup>3</sup> and a specific surface area of roughly 300 m<sup>2</sup> g<sup>-1</sup> was claimed. Further constituents of sample R2 include water (32.2 wt%), Na<sub>2</sub>O (0.5 wt%), K<sub>2</sub>O (1.4 wt%), Ca (2.5 wt%), and Mg (0.1 wt%). The sum of all constituents adds up to 105.8 wt%. This challenges the reliability of the product data sheet. Both reference samples are commercially available and serve as benchmarks.

Samples A, B1, B2, and C were obtained from different laboratory-scaled methane pyrolysis processes performed at Montanuniversität Leoben. Sample A was derived from a liquid metal process using a mixture of 90 wt% Cu and 10 wt% Ni at 1250 °C as a liquid catalyst. In an earlier experiment liquid Zn was introduced into the reactor chamber. After the experiment, it was replaced by Cu and Ni. Zn was detected in subsequent EDS measurements of sample A, and thus was most likely not fully removed from the chamber. The deployment of a liquid catalyst prevents catalyst deactivation due to carbon formation. A lab-scaled induction furnace was used. The process gases were blown into the reaction chamber from the bottom of the crucible. A mixture of CH<sub>4</sub> and N<sub>2</sub> was used with the later providing additional flushing of the process chamber. The carbon was transported with the exhaust gas and collected in a filter system of the reactor.

Samples B1 and B2 were both derived from thermal pyrolysis using a plasma-based process, where a DC-plasma with a transferred arc was used. During the production of

---

<sup>2</sup>Based on the data sheet provided by GBKB, it is assumed that "%" refers to wt%.

<sup>3</sup>Based on the data sheet provided by Sonnenerde GmbH, it is assumed that "%" refers to wt%.

sample B1 the ratio of the two process gases Ar and CH<sub>4</sub> was varied in an unknown manner<sup>4</sup>, thus carbon production parameters were not constant throughout the experiment. In sample B2 a fixed ratio of 50 vol% Ar and 50 vol% CH<sub>4</sub> was used.

Sample C was derived from a fixed bed process. The experiment was performed in a lab-scaled vertical reactor with an inner diameter of 78 mm. Electrical heating was utilized to establish a process temperature of 800 °C. Reduced iron ore pellets with a diameter of roughly 12 mm were used as a catalyst with the carbon growing on top of these spherical pellets. Separation of catalyst and carbon was performed by mechanically removing the carbon.

A summary of all samples characterized in this thesis is given in Table 1. It has to be noted that all pyrolysis-derived carbons are produced in laboratory-scaled experiments using commercially available methane rather than natural gas. These test runs were focused on establishing appropriate operating parameters (e.g. process temperature, gas flow, ratio of gases used, types of catalyst used) in order to achieve a reasonable process performance (e.g. hydrogen yield, hydrogen purity, methane conversion ratio). The very first carbon samples obtained from reasonably stable processes were investigated within this thesis. Meeting certain minimum process performance parameters is a prerequisite for methane pyrolysis to become a large-scale industrial production process for hydrogen. There was no focus on obtaining certain allotropes or morphologies of carbon in these primary investigations.

The goal of this thesis is to investigate carbon samples obtained in early stages of the methane pyrolysis process development in order to obtain a very first profile of carbon properties. This would allow to give directions in which to further develop the process with certain applications for the carbons in mind.

Table 1: Overview of samples investigated in this thesis.

Sample ID	Origin
R1	mineral graphite (commercially available)
R2	biochar (commercially available)
A	liquid metal process
B1	plasma process
B2	plasma process
C	fixed bed process

<sup>4</sup>The goal was establishing a stable process rather than producing carbon.

## 2.2 Experimental methods

This chapter contains an overview of the experimental methods performed at the Montanuniversität Leoben and employed in this thesis.

### 2.2.1 Optical microscopy

An optical investigation of the samples was carried out using an Axio Lab.A1 optical microscope by Zeiss. Micrographs were taken using an Axiocam 105 color microscope camera by Zeiss. Image processing was done using the software package ZEN (version 2.5, blue edition) by Zeiss.

### 2.2.2 Powder dispersion studies

Powder dispersion studies were performed using distilled water and ethanol. About 20 mg of powder were dispersed in 20 mL of distilled water and ethanol respectively. Glass vials were used to mix the samples with the distilled water or ethanol. The samples were shaken manually and placed in an ultrasonic bath for 10 min to establish a uniform mixing of powder and liquid. Digital photographs were taken after mixing as well as after 1, 7, and 28 days to investigate the dispersion behavior.

### 2.2.3 Poured bulk density measurements

Poured bulk density measurements were obtained by weighting a defined volume of the sample using a plastic vial with a defined volume ( $V = 2 \text{ mL}$ ). Each powder was poured into the plastic vial and then the sample mass  $m$  was determined using a precision scale. As no compaction step was performed, the poured density of the sample was calculated as  $\rho_{bulk} = m/V$ . It has to be noted that no standardized procedure was applied. Therefore, poured bulk density data may be used in a qualitative way only (e.g. to establish a relative ranking of samples).

### 2.2.4 Scanning electron microscopy (SEM) and energy dispersive X-ray spectroscopy (EDS)

Scanning electron microscopy (SEM) was performed with an Tescan CLARA scanning electron microscope. All micrographs were taken in secondary electron contrast mode using an acceleration voltage of 10 keV. For chemical analysis in-SEM energy dispersive X-ray spectroscopy (EDS) was performed. Prior to the measurements a sputter-coating

with gold was applied to ensure the minimum electric conductivity required to perform SEM and EDS investigations and to avoid potential charging effects during imaging.

### 2.2.5 X-ray diffractometry

Laboratory X-ray diffraction (XRD) experiments during this thesis were performed on a Bruker D8 Advance Eco using a voltage of 40 kV and a current of 25 mA. The samples were placed on a rotating measurement tray for obtaining improved statistics and measured using  $Cu K_\alpha$  radiation with a wavelength  $\lambda$  of 1.5418 Å. Measurements were carried out in a diffraction angle  $2\theta$  range from  $10^\circ$  to  $90^\circ$  with a step size of  $0.01^\circ$  and 2 s exposure time resulting in a total measurement time of roughly 4.5 hours per sample.

The powder diffraction files 4+ (PDF4+) database by the International Center of Diffraction Data (ICDD) was used to obtain diffraction patterns of various compounds. Peak fitting for determining peak positions and Full Width at Half Maximum (FWHM) values was carried out using the software package Origin 2020 (version 9.7.0.188). Gaussian functions were applied to determine the  $2\theta$  angles and the FWHM values for (002), (100), (004), and (110) peaks of carbon in a similar manner as reported in literature [86]. Turbostratic carbons do not display (101), (112), and (102) peaks [24, 75].

Crystallographic parameters that may be determined from the diffraction pattern include the crystal length  $L_a$ , the crystal length  $L_c$ , the interlayer distance  $d_{002}$ , and the interplanar distances  $d_{100}$  and  $d_{110}$ .

Scherrer's equation allows to calculate the crystallite sizes  $L_c$  and  $L_a$  based on the peak position and FWHM according to Eq. 10 [24, 74, 86]:

$$L_c(XRD) = \frac{0.89 \lambda}{FWHM_{002} \cos\theta_{002}} \quad (10a)$$

$$L_a(XRD) = \frac{1.84 \lambda}{FWHM_{100} \cos\theta_{100}} \quad (10b)$$

$$L_a(XRD) = \frac{1.84 \lambda}{FWHM_{110} \cos\theta_{110}} \quad (10c)$$

Bragg's law allows to calculate the interlayer spacing  $d_{002}$  according to Eq. 11.

$$d_{002} = \frac{\lambda}{2 \sin\theta_{002}} \quad (11)$$

Instrumental broadening has to be subtracted to obtain broadening from other sources including crystallite size. This was particularly important for Eq. 10. The X-ray diffractogram of a standard Corundum sample was collected. The Corundum reflections were peak-fitted using Gaussian functions. The results are given in Table 2. Because Gaussian functions were used for peak fitting of the carbon sample diffractograms, it was possible to subtract the influence of the instrumental broadening according to Eq. 12.

$$FWHM_{eff} = \sqrt{FWHM_{meas}^2 - FWHM_{ib}^2} \quad (12)$$

In this equation,  $FWHM_{meas}$  is the FWHM value obtained from the sample measurement,  $FWHM_{ib}$  is the contribution of instrumental broadening and  $FWHM_{eff}$  is the FWHM value used in subsequent calculations. Instrumental broadening varied over the  $2\theta$  range of the instrument, thus Corundum peaks close to the reflection angles of the (002), (100), (004), and (110) carbon peaks were used to subtract the instrumental broadening.

Table 2: X-ray diffraction data obtained from a Corundum sample for determining the instrumental broadening.

$2\theta$ (°)	$FWHM_{ib}$ (°)	(hkl)	Comment
25.60	0.097	(012)	Used as the value for the instrumental broadening for the (002) carbon peak
35.16	0.047	(104)	
43.36	0.049	(113)	Used as the value for the instrumental broadening for the (100) carbon peak
52.56	0.054	(024)	Used as the value for the instrumental broadening for the (004) carbon peak
57.50	0.057	(116)	Used as the value for the instrumental broadening for the (110) carbon peak
61.31	0.057	(018)	

### 2.2.6 Small angle X-ray scattering (SAXS)

Small-angle X-ray scattering (SAXS) experiments were performed on an N8 Horizon laboratory SAXS instrument from the company Bruker AXS using  $Cu K_\alpha$  radiation with a wavelength  $\lambda$  of 1.5418 Å, a voltage of 50 kV and a current of 100 µA. Silver behenate was used to calibrate the device due to its large number of sharp peaks in the range below  $2\theta = 20^\circ$  [87]. The samples were poured on sticky tape and then inserted into the sample chamber. Vacuum was applied and 2D SAXS patterns were collected at three different measurement points for each sample. This allowed to estimate whether local variations within each individual sample were present. Each point was measured for 500 s. The software MULIP SAXS-2D provided by Gerhard Popovski of the Montanuniversität Leoben was used to perform the azimuthal integration of the 2D SAXS data. The tape was measured independently and subtracted from the sample measurements. The intensity detected for the tape was significantly smaller than the intensity for the tape with the sample. Therefore it would have been possible to neglect the influence of the tape rather

than subtract it. Fig. 8 depicts three scattering curves recorded for sample R1 with the azimuthal integration already performed.

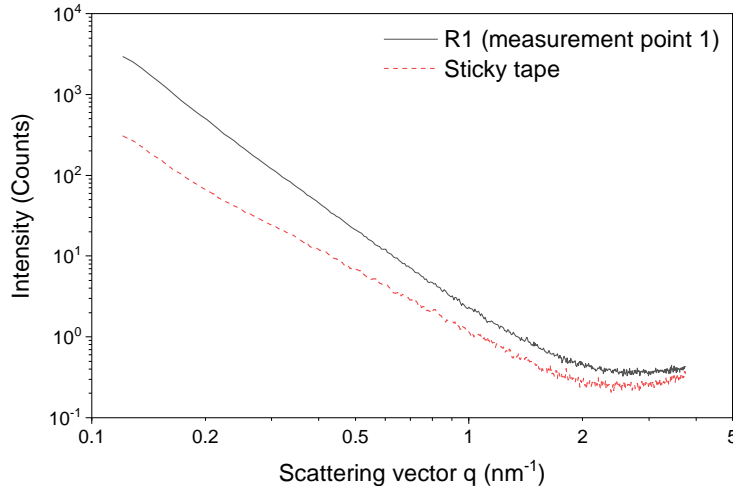


Figure 8: Results of the SAXS measurement of sample R1 and the sticky tape.

### 2.2.7 Raman spectroscopy

Raman spectra were recorded using a Jobin Yvon LABRAM confocal Raman spectrometer. A frequency-doubled Nd-YAG laser ( $\lambda_0 = 532.02 \text{ nm}$ ) was used. Raman shifts were obtained from  $100 \text{ cm}^{-1}$  to  $3500 \text{ cm}^{-1}$  using a Peltier-cooled slow scan-CCD matrix-detector. Samples were measured in 3 cycles using 20 s exposure time for each cycle. The experiments were performed at room temperature. An Olympus BX 40 microscope fitted with a  $\times 10$  and a  $\times 100$  long-working distance objective lens was used to perform laser focusing and sample viewing prior to the actual measurement. Three consecutive Raman measurements were carried out at the same spot in the sample. No change in the Raman spectra was detected during three repeated measurements indicating that the local energy density did not influence or destroy the microstructure of the sample. To illustrate the D band, G band, and G'(2D) band positions, the Raman spectrum of sample R1 is given in Fig. 9.

In literature, Raman spectra of carbonaceous materials are used to determine crystallite size  $L_a$ . Tuinstra and Koenig reported an empirical relationship between the crystallite size  $L_a$  obtained from XRD and the intensity ratios of the D and G bands in disordered non-graphitic carbons [80]:

$$\frac{I_D}{I_G} \propto \frac{1}{L_a} \quad (13)$$

Knight and White refined this formula by taking the wavelength of the laser  $\lambda_0$  into

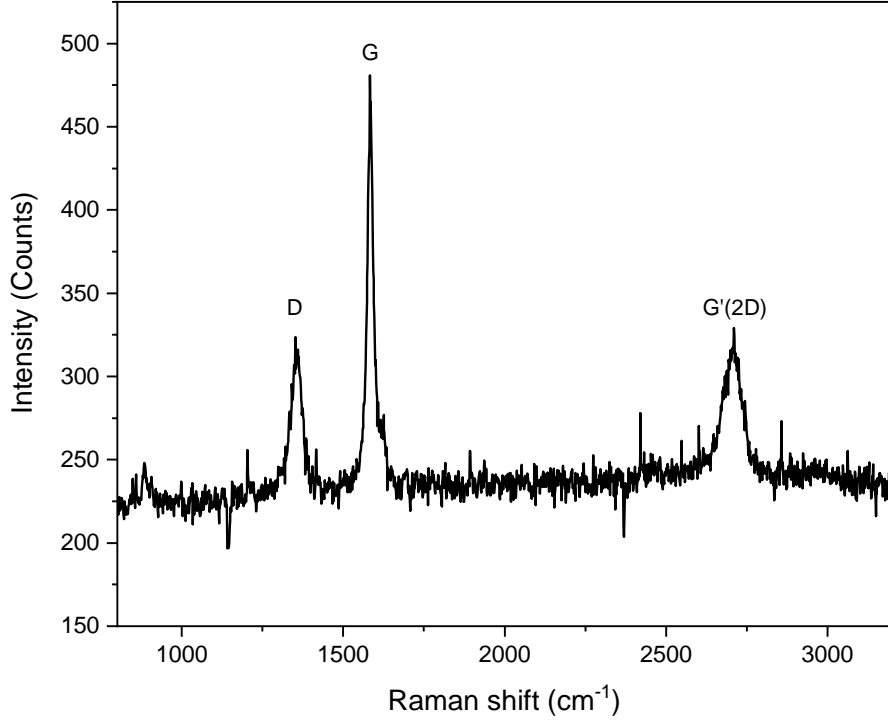


Figure 9: Raman spectrum of sample R1. D, G, and G'(2D) peaks are clearly visible. Relative intensities of peak heights or integrated areas are used to estimate the crystallite size  $L_a$ .

account [88]:

$$\frac{I_D}{I_G} = \frac{C(\lambda_0)}{L_a} \quad (14)$$

In this formula  $C(\lambda_0)$  describes a wavelength-dependent factor. In accordance with Matthews et al., Eq. 15 was applied to determine  $C(\lambda_0)$ . The values used were  $C_0 = -12.6$  nm and  $C_1 = 0.033$  [89].

$$C(\lambda_0) = C_0 + \lambda_0 C_1 \quad (15)$$

As discussed by Zickler et al. many papers do not clearly state whether a ratio of peak intensities or integrated peak areas should be used [74]. In this thesis, calculations were performed for both peak intensities and integrated peak area ratios. Peak fitting was performed with the software MagicPlot (version 2.9.3) using a linear function for the background and Gaussian functions for the D, G, and G'(2D) bands. Various alternative approaches were applied in literature [90].



### 2.2.8 Thermogravimetric analysis (TGA) and differential scanning calorimetry (DSC)

Thermogravimetric analysis (TGA) and differential scanning calorimetry (DSC) were performed simultaneously on a DSC Setsys Evo 2400 device from the company Setaram. Synthetic air consisting of 20 vol% oxygen and 80 vol% nitrogen with a flow rate of  $16 \text{ mL min}^{-1}$  was used. Samples were placed in an  $\text{Al}_2\text{O}_3$  crucible with a volume of  $100 \mu\text{L}$ . Sample mass ranged from 5 mg to roughly 15 mg. All samples were treated according to the temperature profile depicted in Fig. 10. Heating was performed from room temperature to  $1500^\circ\text{C}$  using a constant heating rate of  $10 \text{ K min}^{-1}$ . The maximum temperature was held for 30 min. A cooling zone mirroring the heating zone concluded the measurement. For analytical purposes only the heating zone was considered. Prior to actual measurements a reference measurement was performed using an empty  $\text{Al}_2\text{O}_3$  crucible. The mass gain versus temperature curve and the heat flow versus temperature curve from this reference measurement were subtracted from all subsequent sample measurements in order to obtain heat flow and mass loss values that may be attributed to changes occurring within the sample only.

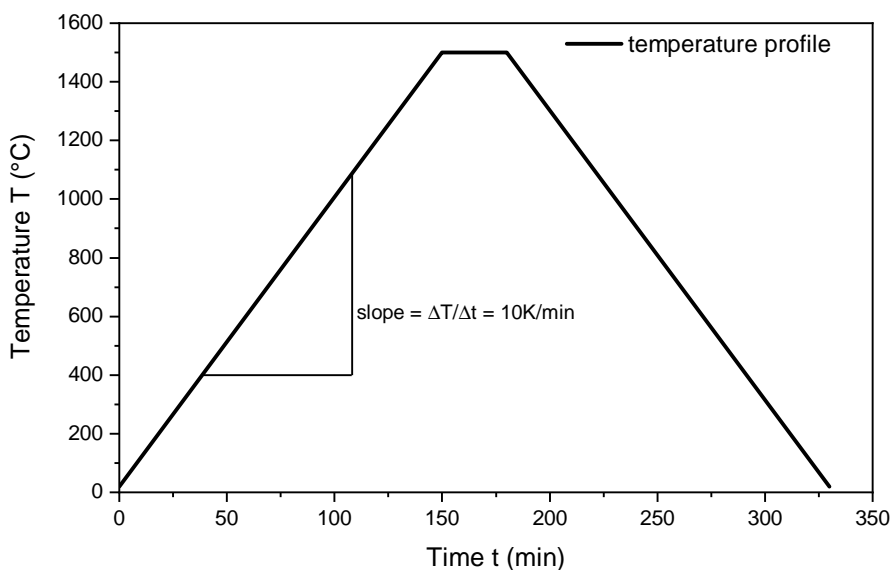


Figure 10: Temperature profile used for the TGA-DSC measurements.

It has to be noted that an error in the calibration of the device caused incorrect values of absolute heat flow and shifts in temperature data of about  $\pm 20^\circ\text{C}$ . Since all measurements were performed using the same erroneous calibration setting, heat flow data may not be used quantitatively, but may very well be used to establish qualitative relationships. For example, it is possible to rank the occurrence of phase transformations from the lowest temperature to the highest temperature. It is, however, not possible to give a precise value for said transformation temperatures. Mass values (e.g. carbon con-

tent, amount of inorganic residue) are not affected by the calibration error. To illustrate a TGA-DSC measurement sample R1 is depicted in Fig. 11. The carbon content was estimated to be 46.0 %. An exothermal peak was detected.

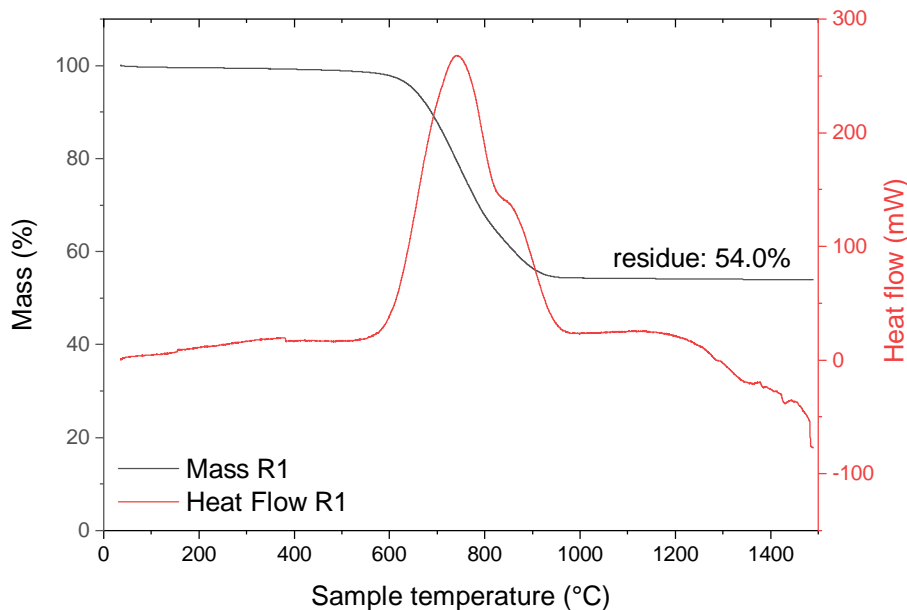


Figure 11: Result of the TGA-DSC measurement of sample R1. The mass loss is attributed to the combustion of carbon to form  $\text{CO}_2$ . The DSC data show an exothermal peak in heat flow. This might be explained by a bimodal particle size distribution within the sample.

### 2.2.9 Gas sorption analysis

Gas sorption experiments were performed using a Quantachrome Autosorb iQ3 gas sorption analyzer from Anton Paar. Nitrogen ( $\text{N}_2$ ) was used as an adsorbate for all samples except for sample R2 for which  $\text{CO}_2$  was used.

The  $\text{N}_2$  measurements were performed at a constant sample temperature of 77 K using liquid nitrogen as a cooling agent. Measurements were carried out from a relative pressure  $p/p_0 = 10^{-3}$  to slightly less than 1. Prior to the measurement all samples were degassed at 250 °C for 24 h under a vacuum ( $10^{-6}$  mbar). Samples were placed in sample cells made of glass. Prior to the sorption measurement a glass rod was inserted into the sample cell to minimize the free volume.

The experiments were conducted using the software AsiQWin (version 5.3) provided by Anton Paar. AsiQWin was used to calculate the Brunauer–Emmett–Teller (BET) area based on the multi-point BET method. Data points in the relative pressure range of  $p/p_0 = 0.12 - 0.30$  were used. It has to be noted that the BET area is not equivalent to, but may be used as an estimate for the specific surface area, especially for the case

of non-porous, macroporous, and mesoporous materials. Fig. 12 depicts the adsorption isotherm of sample R1 which displays a hysteresis loop due to condensation of nitrogen within mesopores.

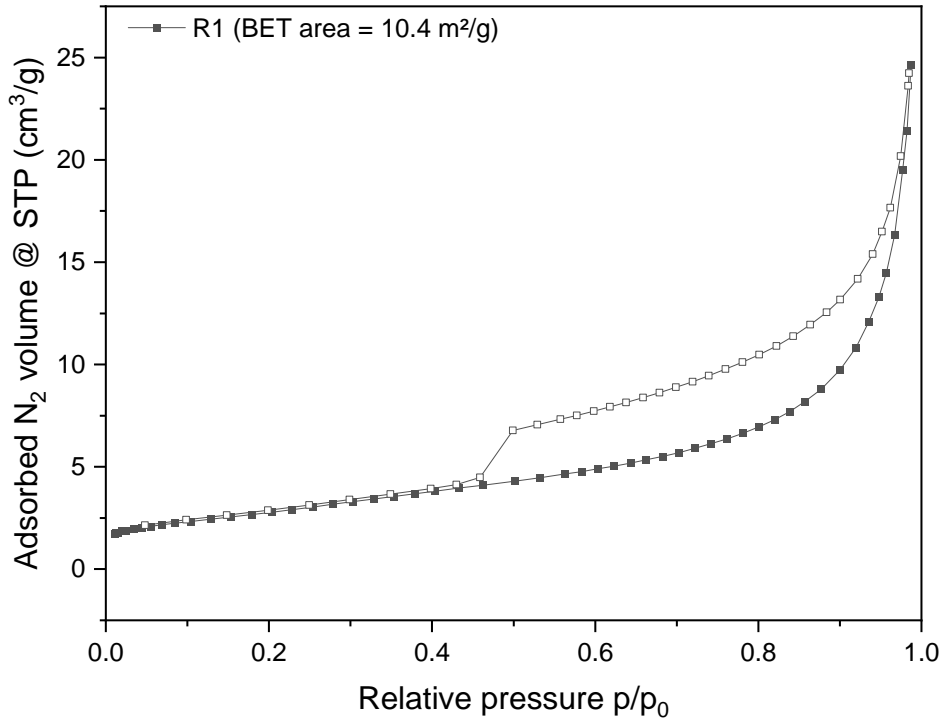


Figure 12: Gas sorption analysis data of sample R1. The measurement was performed using N<sub>2</sub> at 77 K. Solid symbols denote the adsorption branch, open symbols the desorption branch.

The biochar sample R2 was measured using CO<sub>2</sub> at 273 K. This was done because two measurements using N<sub>2</sub> at 77 K failed to record adsorption isotherm data. This was attributed to the typically small micropore sizes coupled with a tortuous pore network of biochars and slow kinetics of N<sub>2</sub> at 77 K. The experiment was performed using a cooling bath filled with a mixture of water and anti-freezing liquid, which was coupled with an external temperature controlling device. The sample preparation procedure was identical to the nitrogen experiments and the same software was used. The Grand Canonical Monte Carlo method was applied to extract the pore size distribution and give an estimate of the specific surface area [91].

### 3 Results

This chapter presents the results obtained for the six carbon-rich samples summarized in Table 1. The goal of this chapter is to provide important structural and compositional data of the investigated samples.

#### 3.1 Results from basic characterization methods

A quick poured bulk density estimate of the samples was obtained by weighting a defined volume of the sample. Sample R2 was ground using a mortar and a pestle prior to this and all subsequent investigations, as the biochar consisted of individual pellets that were too big for conventional methods requiring powder samples. The data presented in Fig. 13 allowed to establish a relative ranking between the samples. Quantitative statements cannot be made based on this data as no standardized procedure was applied. Sample C displays the highest poured bulk density and was later found to contain the largest quantities of metals. Sample B1 has the lowest poured bulk density which was found to correspond to a comparatively large specific surface area. Important factors determining the poured bulk density are the macroscopic appearance (e.g. aggregated particles), the particle size distribution, and the fractions of phases present (e.g. presence of metallic particles along with carbon particles).

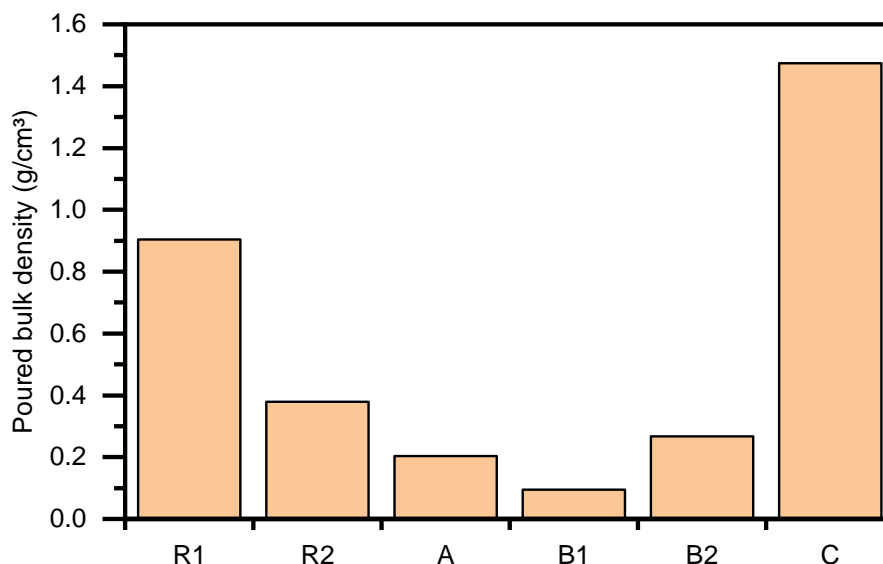


Figure 13: Comparison of poured bulk densities. No standardized procedure was used to determine the poured bulk density (data may be used quantitatively only).

Micrographs derived by optical microscopy are presented in Fig. 14. All samples were powders. Sample B1 and B2 were described as particularly fine powders. Due to the low

depth of field of an optical microscope, this method proved to be ineffective for characterization purposes, as it was not possible to distinguish between different phases based on color or particle shapes. A test run was performed to see whether a resin embedded polished specimen with a smooth, flat surface could be prepared. A suitable smoothness of the surface could not be achieved, neither using *DuroCit-3* from the company *Struers* nor *Demotec 70* as the embedding medium of the specimen. Individual particles broke loose from the embedding medium during the polishing process. This posed a significant challenge in specimen preparation that could not be solved within this thesis.

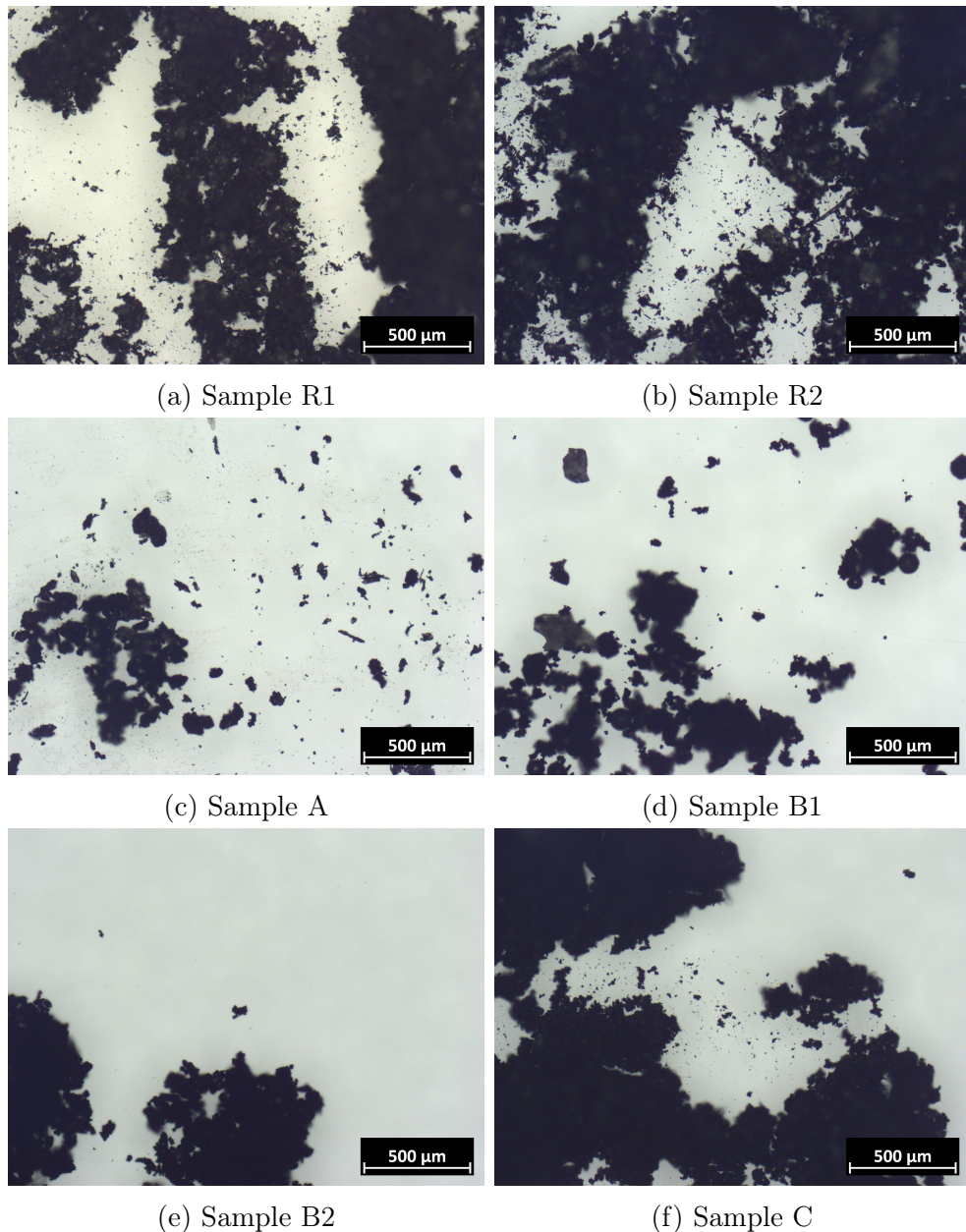


Figure 14: Comparison of various samples using the optical microscope.

For the dispersion studies, about 20 mg of sample were dispersed in about 20 mL of distilled water or ethanol. Photographs were taken right after mixing, after 1 day, after

2 days, and after 28 days to monitor the unmixing process. The results are depicted in Fig. 15. In distilled water unmixing finished for the samples R1, A, B1, and B2 within 1 day. In ethanol unmixing occurred at a slower rate and finished within 7 days for all samples. The dispersion behavior depends on the particle size distribution, on the phases present and on the surface groups which influence the wetting properties of the sample. Sample R2 displayed the slowest unmixing process in distilled water with a significant fraction of the powder still dispersed after 1 day. Sample C showed a distinct yellow color that faded slowly and was almost fully vanished after 28 days. Traces of iron were found in this sample (see Fig. 16) as orange-brownish deposits of iron oxide were visible in the glass vial. This is in good agreement with the poured bulk density measurements for which sample C had the largest poured bulk density. This is explained by iron particles with a high crystal density mixed together with carbon particles of a comparably low crystal density.

Barrie et al. [92] found that a dispersion of carbon black in an aqueous solution was not stable without the "addition of polymer to a level corresponding to a ratio of 50 mg of polymer per 13 m<sup>2</sup> of surface area (i.e. 15 wt% particles)" [92]. Stankovich et al. [93] reported stable graphitic nanoplatelets after coating the platelets in poly(sodium 4-styrenesulfonate). The graphitic nanoplatelets were synthesized via the reduction of exfoliated graphene oxide [93]. Wang et al. [34] found that graphene nanosheets that were "freshly prepared via chemical reduction are non-dispersable in aqueous solution". The graphene nanosheets floated on water when no surfactant was added. "However, on adding poly(sodium 4-styrenesulfonate) during the reduction process, hydrophilic graphene nanosheets were obtained, which could be well dispersed and formed a homogeneous aqueous solution" [34]. Tanvir, Biswas, and Qiao [94] mixed ethanol with roughly 1-5 wt% of graphite nanoparticles. The dispersion "maintained good suspension quality for at least several hours" [94].

## 3.2 Sample morphology and chemical composition

Fig. 17 and Fig. 18 depict the sample morphology as obtained from SEM. All micrographs were taken in secondary electron mode after a gold coating of the powder was applied to ensure an adequate electrical conductivity and avoid potential charging effects during imaging. EDS spectra were recorded in order to make qualitative statements on the elemental composition. Quantitative or semi-quantitative statements using EDS cannot be made for the samples presented within this thesis as the low energy of the carbon K characteristic X-ray at 282 eV, which implies a significant self-absorption. An example of a similar situation is given by Newbury and Ritchie [95].

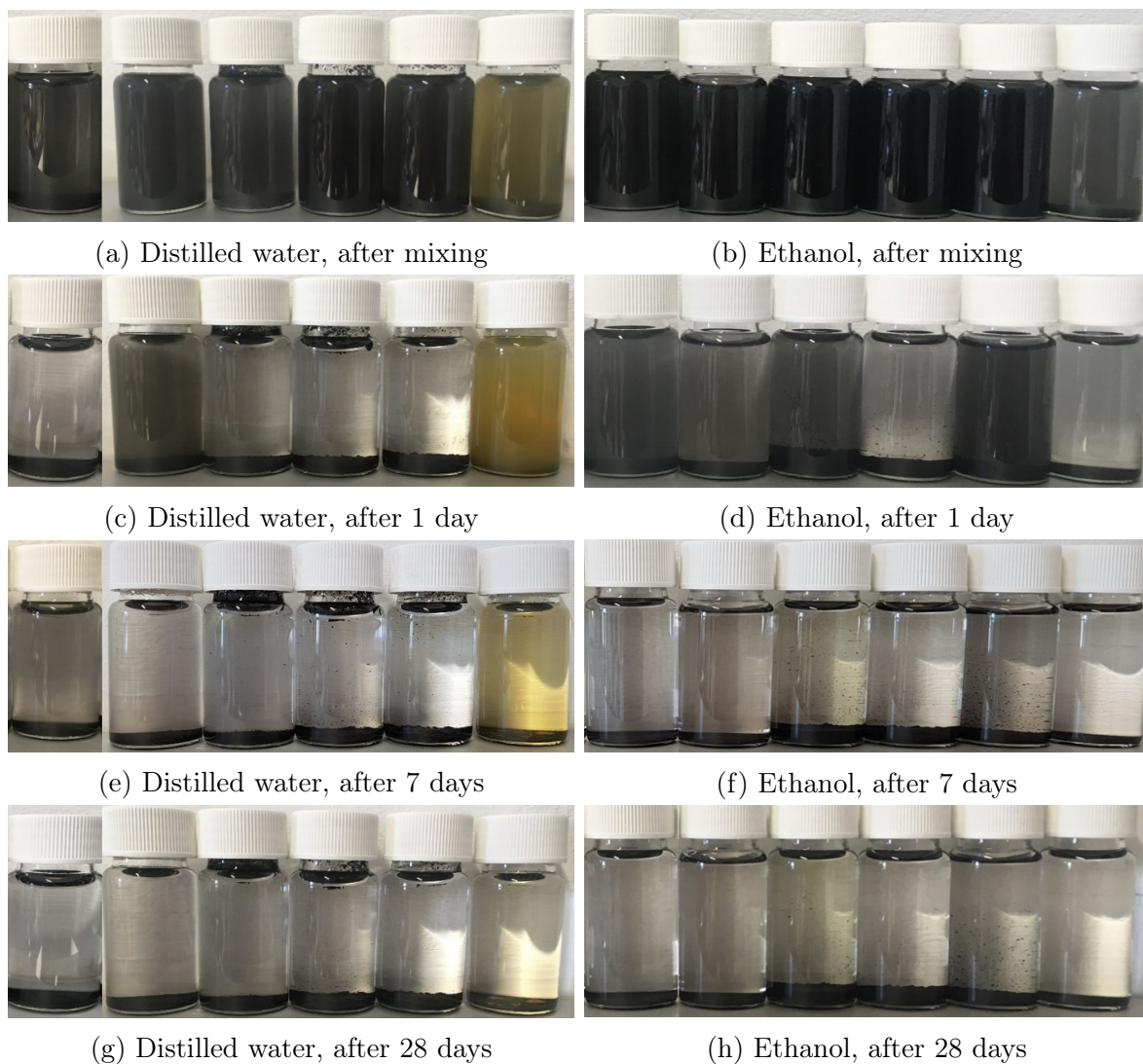


Figure 15: Dispersions of investigated samples using distilled water (left side) or ethanol (right side) as solvents. Photographs were taken right after mixing (a, b), after 1 day (c, d), after 7 days (e, f), and after 28 days (g, h). Sample order in all photographs from left to right: R1-R2-A-B1-B2-C.

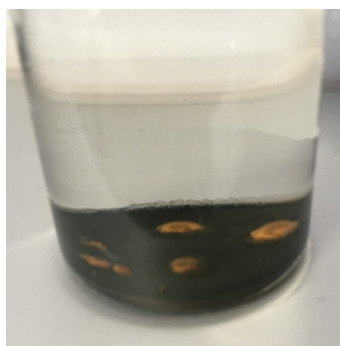


Figure 16: Dispersion of sample C in distilled water after 28 days. The yellow color present immediately after mixing faded slowly and disappeared completely after 28 days. The orange-brownish deposits that occurred on the bottom of the glass vial are caused by iron oxide formation ("rust").

Sample R1 consists of flake-like particles that display a broad particle size distribution. At high magnifications smaller particles that are attached to larger flakes are visible. Sample R2 consists of a wide variety of irregularly shaped particles. At high magnifications a ribbed structure is visible. This result was in good agreement with literature [96, 97].

Sample A consists of elongated particles. At higher magnifications fine, spherical particles that are fused to larger, elongated particles are visible. Samples B1 and B2 consist of agglomerated particles (i.e. particles that are fused together). Higher magnifications reveal fine, fluffy particles. In between particles, some filamentous structures are visible. In comparison, sample B1 appears to be more homogeneous than sample B2. Sample C again consists of agglomerated particles. At high magnification levels, the sample surface appears to be smooth when compared to all other samples and samples B1 and B2 in particular. The macroscopic appearance and the microscopic morphology are summarized in Table 3.

Table 3: Sample morphology and macroscopic appearance.

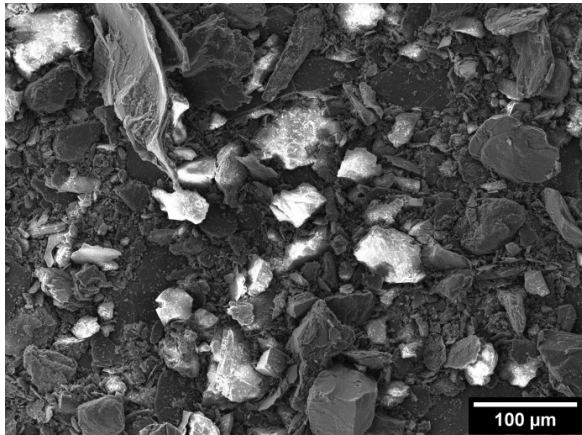
<b>Sample ID</b>	<b>Macroscopic appearance</b>	<b>Microscopic morphology (scanning electron microscopy)</b>
R1	powder	flake-like particles
R2	powder	irregularly shaped particles
A	powder	elongated particles
B1	fine powder	agglomerates
B2	fine powder	agglomerates
C	powder	agglomerates

Representative EDS spectra were collected for all samples and are given in Fig. 19. All EDS spectra showed a dominant peak associated with carbon. Both samples R1 and R2 displayed significant impurities of Si and O. Besides carbon, sample A contained significant amounts of Cu, Zn and O impurities. Sample B1 contained C, Fe, O and minor amounts of Cu. For sample B2 the elements C, O, Fe and Al were detected. For sample C the elemental composition included C, Fe, Si, and O. The elements detected using EDS are summarized in Table 4.

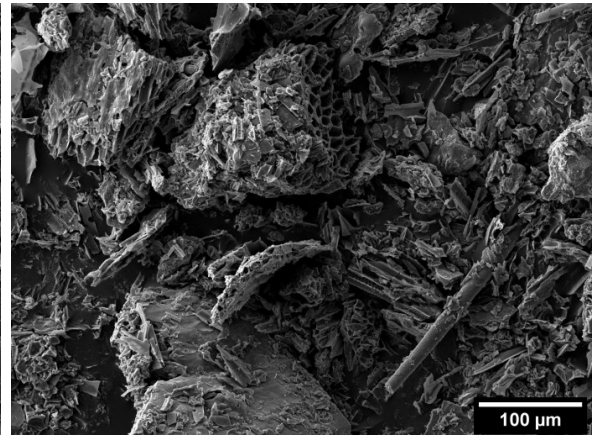
### 3.3 Results from X-ray diffraction experiments

X-ray diffraction experiments were performed for all samples. The obtained X-ray diffraction patterns were compared to the X-ray diffraction pattern of graphite according to the Powder Diffraction File (PDF) 00-056-0159 given in Table 5. In the powder XRD pattern of turbostratic carbon only  $(hk0)$  and  $(00l)$  reflections are present, while reflections with mixed indices including  $(101)$ ,  $(102)$ , and  $(112)$  do not occur [24].

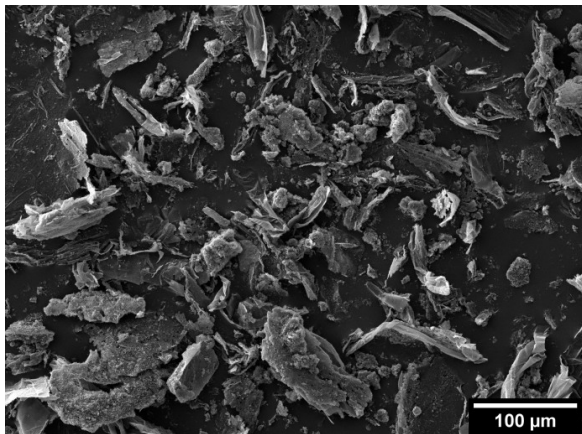




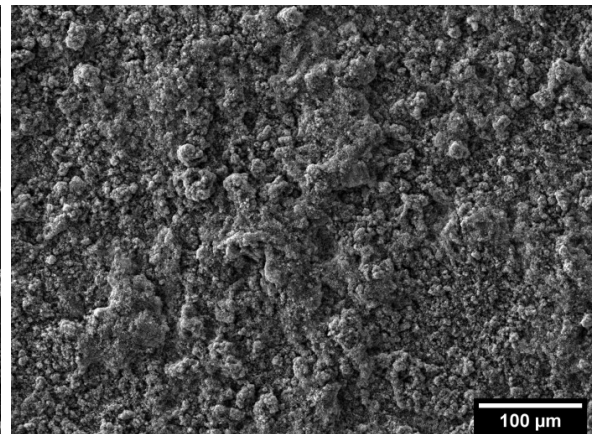
(a) Sample R1



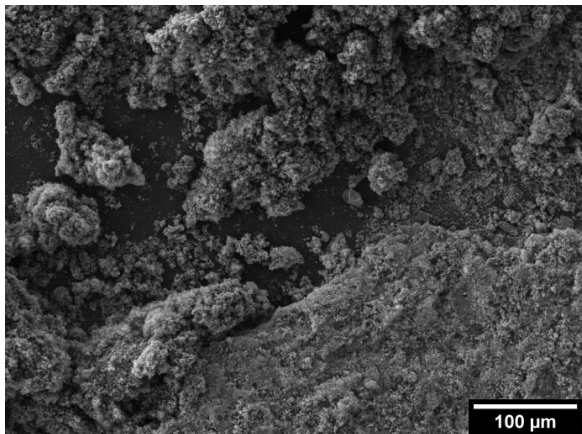
(b) Sample R2



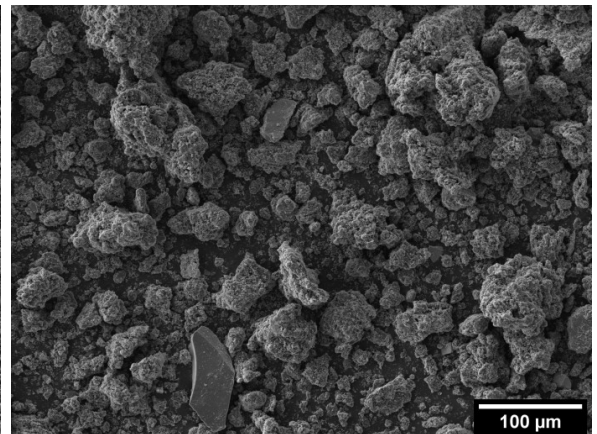
(c) Sample A



(d) Sample B1

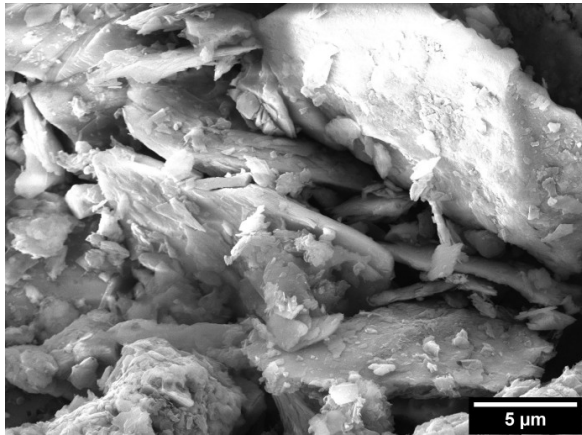


(e) Sample B2

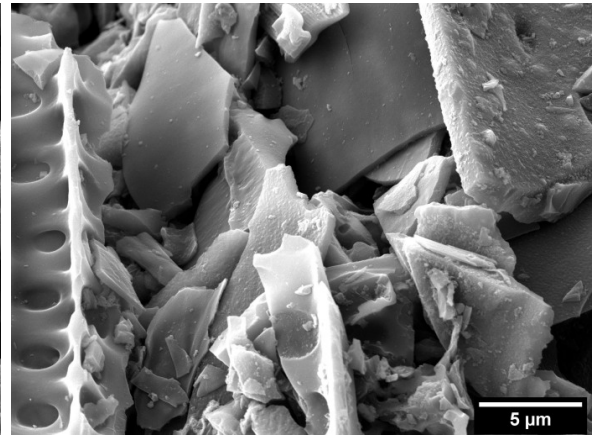


(f) Sample C

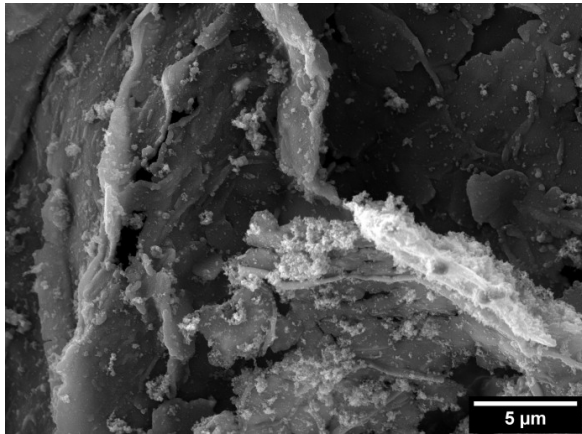
Figure 17: SEM micrographs taken at low magnification.



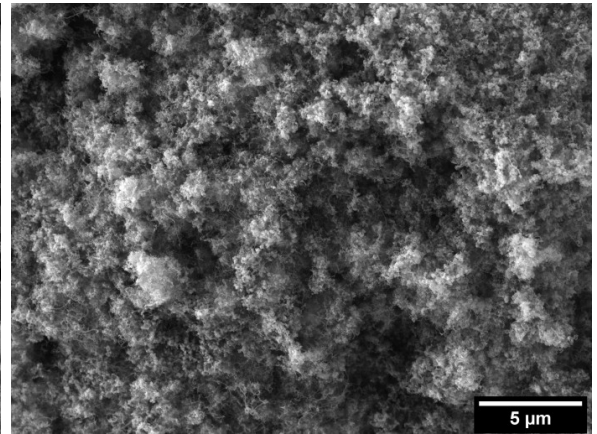
(a) Sample R1



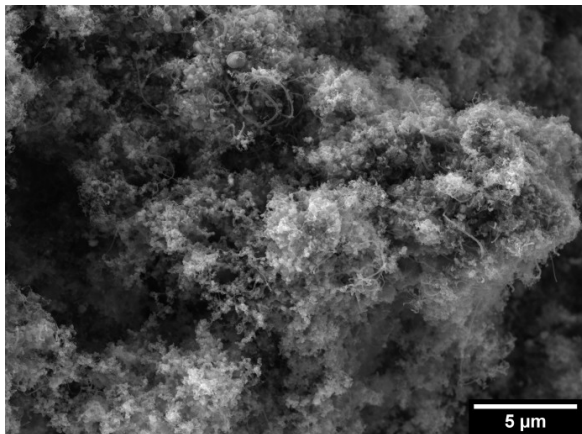
(b) Sample R2



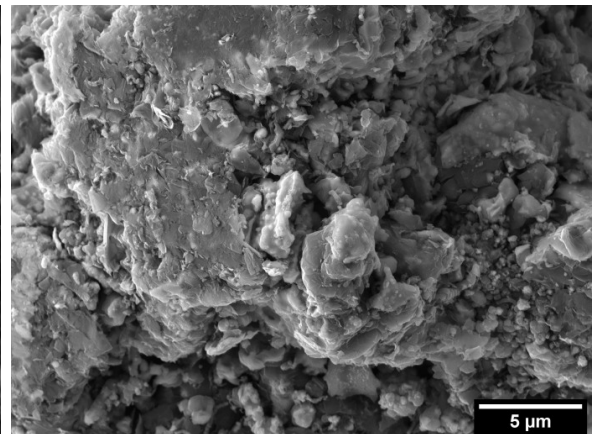
(c) Sample A



(d) Sample B1



(e) Sample B2



(f) Sample C

Figure 18: SEM micrographs taken at high magnification.

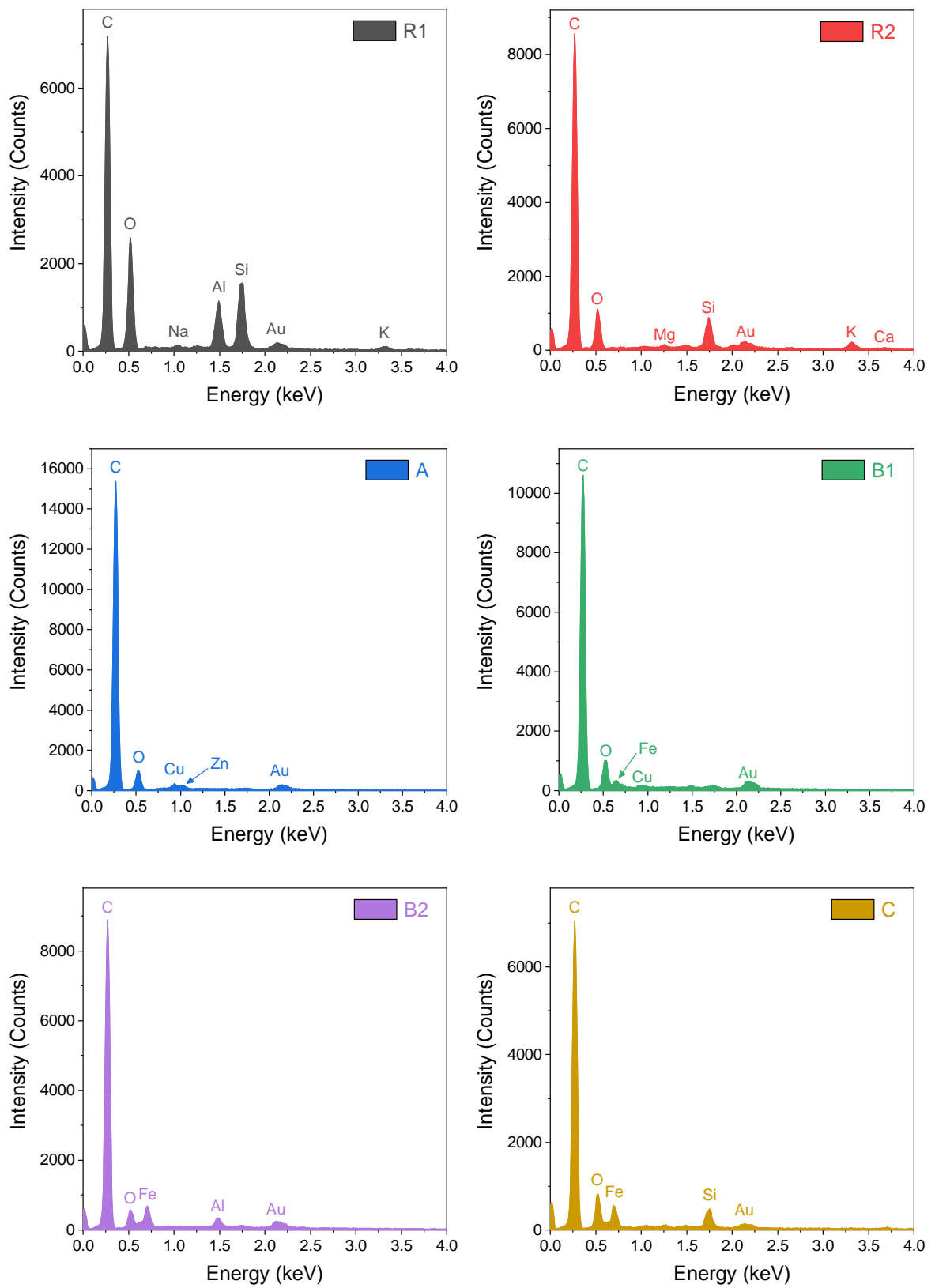


Figure 19: Representative EDS spectra.

Table 4: Elements detected using EDS. The elements were sorted according to their atomic number. It has to be noted that light elements (e.g. H) cannot be detected in EDS.

Sample ID	Elements detected
R1	C, O, Na, Al, Si, K
R2	C, O, Mg, Si, K, Ca
A	C, O, Cu, Zn
B1	C, O, Fe, Cu
B2	C, O, Al, Fe
C	C, O, Si, Fe

Table 5: Diffraction pattern of graphite according to Powder Diffraction File 00-056-0159.

$2\theta$ (°)	d (nm)	(hkl)	Intensity	Relationship to turbostratic carbon
26.54	0.3355	(002)	1.00	
42.36	0.2132	(100)	0.07	Corresponds to the (10) peak in turbostratic carbon
44.56	0.2032	(101)	0.06	Does not occur in turbostratic carbon
50.70	0.1799	(102)	0.01	
54.66	0.1678	(004)	0.07	Corresponds to the (11) peak in turbostratic carbon
77.49	0.1231	(110)	0.12	Does not occur in turbostratic carbon
83.62	0.1156	(112)	0.05	Does not occur in turbostratic carbon

Data from EDS and XRD were combined to determine the constituting phases for each sample. The obtained XRD diffractograms are depicted in Fig. 20. The main reflections of all detected phases are indicated with symbols. All samples consist of at least two phases. The marked carbon reflections correspond to the graphite peaks given in Table 5. A summary of the phase analysis results is given in Table 6. The shape of the carbon peaks and the presence of mixed ( $hkl$ ) peaks were used to classify between graphite and turbostratic carbon. This is summarized in Fig. 21.

Table 6: Results of phase analysis. Phases were detected based on XRD data. A pre-selection of possible phases was performed based on the results from EDS. All samples derived by methane pyrolysis contain significant amounts of impurity phases (i.e. phases that are not carbon).

Sample ID	Major impurity phases based on XRD data
R1	SiO <sub>2</sub>
R2	SiO <sub>2</sub>
A	Cu, Zn
B1	Fe, Fe <sub>3</sub> O <sub>4</sub>
B2	Fe, Fe <sub>3</sub> O <sub>4</sub>
C	Fe <sub>3</sub> C, Fe

Both samples R1 and R2 contain carbon along with quartz (SiO<sub>2</sub>). In both diffractograms sharp peaks related to quartz are visible. The diffractogram of sample R1 con-

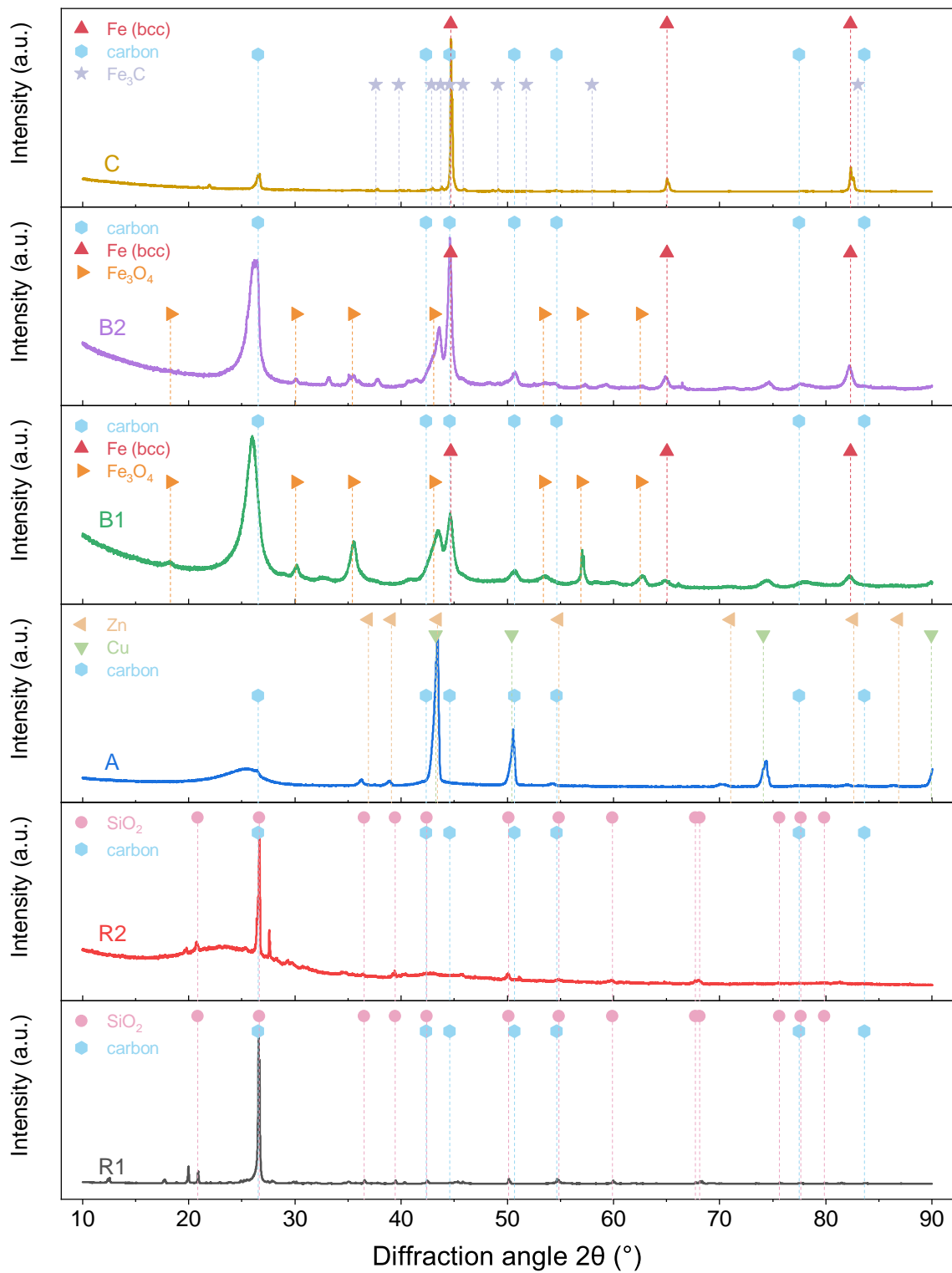


Figure 20: Comparison of X-ray diffractograms. All impurity phases are listed in Table 6.

tains sharp carbon peaks. The strongest reflections of both carbon and quartz overlap in sample R1, causing two almost indistinguishable sharp peaks. The (002) carbon peak of sample R2 is broad and shifted to lower  $2\theta$  angles. No further phases seem to be present based on the X-ray diffractogram.

The X-ray diffractogram of sample A is dominated by Cu reflections with smaller contributions from Zn and carbon. The metal bath used for carbon production contained 10 wt% Ni and Ni was detected in the EDS measurement. Despite that, no distinct peaks of Ni were detected. Ni might be present as a solid solution with the majority element Cu thus contribute to the peaks attributed to pure Cu. Similarly to sample R2 there is a broad (002) peak that is shifted to lower  $2\theta$  angles, indicating a low crystallinity of the sample.

The diffractogram of sample B1 is dominated by carbon with smaller contributions from Fe and  $\text{Fe}_3\text{O}_4$ . The diffractogram of sample B2 is dominated by the sharp (110) peak of Fe that overlaps with the (101) peak of carbon. Smaller contributions stem from other carbon peaks as well as from  $\text{Fe}_3\text{O}_4$ .

The diffractogram of sample C is dominated by iron. Despite the presence of oxygen in the EDS data, there is no evidence for the presence of iron oxides. Cementite ( $\text{Fe}_3\text{C}$ ) is present as a minor impurity. It has to be noted that cementite was not detected in samples B1 and B2 despite the presence of both constituting elements.

Further trace elements that were detected in the EDS measurements did not contribute to the diffraction pattern and are therefore not considered to be present as distinct phases.

Fig. 21 depicts the relevant carbon reflections that allow to **classify between graphite and turbostratic carbon**. Strong reflections from impurity phases were excluded by cutting off the data at a certain intensity.

For sample R1 the (002) carbon peak almost coincides with the (101) peak of  $\text{SiO}_2$ . A peak fitting procedure allowed to separate the two peaks using two Gaussian functions. The peak positions are in good agreement with the expected theoretical values according to PDF 00-056-0159 for graphite and PDF 01-077-1060 for  $\text{SiO}_2$ . The (002) carbon peak is sharp. The FWHM for the (100) carbon peak could not be determined as it overlaps with a  $\text{SiO}_2$  reflection. However, the peak is sharp and clearly visible. The mixed (101), and (112) carbon peaks are clearly visible. The weak (102) carbon peak is not clearly visible. The carbon phase of sample R1 is classified as graphite, due to the presence of mixed peaks and the sharp peak shapes present in the diffractogram.

Sample R2 displays a broad (002) carbon peak that must not be confused with the sharp and distinct (101) reflection of  $\text{SiO}_2$ . The asymmetric shape of the (002) carbon

peak clearly indicates turbostratic carbon. Despite the asymmetric shape, a Gaussian function was used to determine the FWHM of the (002) carbon peak. The (100) peak is broad. The (004) carbon peak could not be investigated as the peak overlaps with the (0 $\bar{2}$ 2) reflection of SiO<sub>2</sub>. The mixed (101), (102), and (112) carbon peaks are not visible. The carbon phase is thus classified as turbostratic carbon due to the asymmetric shape of the (002) carbon peak, a broad (100) carbon peak typically found in turbostratic carbons, and the lack of mixed carbon reflections.

The (002) peak of sample A is almost invisible in Fig. 20 due to the strong Cu reflections, but is clearly seen in Fig. 21. The (002) peak shape is shifted to lower  $2\theta$  angles and is more distinct compared to the (002) peak of sample R2, yet asymmetric in shape, indicating that the carbon phase is turbostratic carbon. A Gaussian function was used to determine the FWHM of the (002) carbon peak. The (100) and (101) peaks of carbon could not be evaluated as they overlap with the strong (111) Cu peak. Similarly, the (102) carbon peak overlaps with the strong (200) Cu peak. The (004) carbon peak has a symmetric shape and appears to be shifted to lower  $2\theta$  angles. Interlayer distances of 0.358 nm and 0.338 nm were calculated based on the peak positions of the (002) and the (004) carbon peak reflections. It was assumed that the (004) carbon peak data is less reliable, as there was no distinct peak for the (102) Zn reflection detected, which was expected to occur in the vicinity of the (004) carbon reflection. The (110) carbon peak is faintly visible but could not be analyzed, while the mixed (112) carbon peak could not be found. The carbon phase of sample A is classified as turbostratic carbon due to the asymmetric peak shape of the (002) carbon reflection and a lack of mixed index reflections.

Sample B1 displays a distinct (002) carbon peak, that was analyzed using a Gaussian function despite the asymmetric shape. The (100) and (101) carbon reflections could not be analyzed as they overlap with reflections from Fe<sub>3</sub>O<sub>4</sub> and Fe. The (102) carbon reflection is clearly visible and the peak shape is symmetric. No distinct (004) carbon peak is visible. The (110) carbon reflection is smeared out and the mixed (112) carbon peak is not visible. Sample B2 displays a more distinct (002) carbon peak compared to sample B1. The (110) carbon peak is visible, but is broad and poorly defined. All other carbon peaks of sample B2 are similar to those found for sample B1. For sample B1 and sample B2 no clear classification can be made based on X-ray diffraction data only.

Sample C displays a distinct, sharp and symmetric (002) carbon reflection indicating a graphitic structure. The (100) and (110) carbon peaks can not be analyzed due to the strong (110) iron reflection and multiple reflections from Fe<sub>3</sub>C. The weak (102) carbon peak is not visible. The (004), (110), and (112) and carbon peaks are clearly visible.

Sample C is conclusively classified as graphite due to a distinct and symmetric (002) carbon peak and due to the occurrence of the mixed (112) carbon reflection.

The diffraction angles of the (002) and (004) carbon peaks were determined to calculate the interlayer distance  $d_{002}$  (or the equivalent value  $2 d_{004}$  in case of the (004) peak). The FWHM of the (002) peak was determined to calculate the crystallite size  $L_c$ . The diffraction angles and the FWHM of the (100) and the (110) carbon peaks were determined to calculate the interplanar distances  $d_{100}$  and  $d_{110}$  as well as the crystallite size  $L_a$ . The contribution of the instrumental broadening to the experimentally obtained FWHM values ( $FWHM_{meas}$ ) was considered according to Eq. 12. The calculated interlayer distances  $d_{002}$  of samples R1 and C of 0.335 nm indicate a graphitic structure and are in good agreement with the equivalent values  $2 d_{004}$ . For sample A, the interlayer distance  $d_{002}$  of 0.358 nm and the equivalent  $2 d_{004}$  value of 0.338 nm do not agree with each other. It is assumed that the result of the (002) carbon peak is more reliable due to the much more pronounced shape of the peak and the lack of reflections of other phases in the same region of the X-ray diffractogram. The (004) carbon peak is in close vicinity of the (102) Zn reflection and thus considered less reliable.



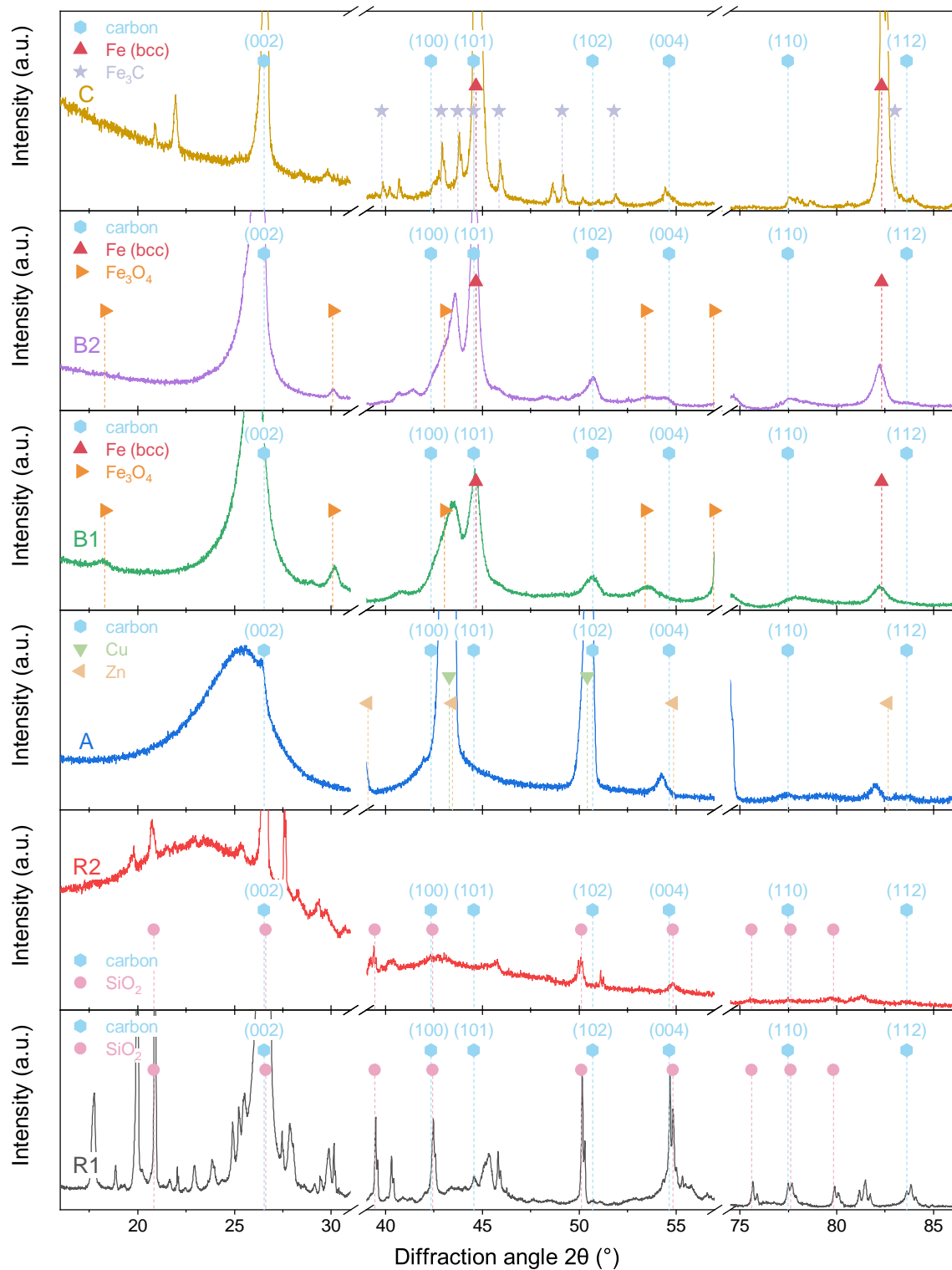


Figure 21: Detailed comparison of carbon reflections obtained in X-ray diffraction experiments.

Table 7: Results from X-ray diffraction experiments. Four carbon peaks were analyzed. The interlayer distance  $d_{002}$  was analyzed based on the (002) peak as well as by calculating  $2d_{004}$  (equivalent to  $d_{002}$ ) based on the (004) peak. Crystallite size  $L_c$  was calculated based on the (002) peak. Crystallite size  $L_a$  was calculated based on both (100) and (110) peaks of carbon. Some data could not be extracted due to overlaps with peaks of impurity phases.

Sample ID	(002) peak				(100) peak				(004) peak				(110) peak						
	$2\theta_{002}$ (°)	FWHM <sub>meas</sub> (°)	FWHM <sub>eff</sub> (°)	$d_{002}$ (nm)	$L_c$ (nm)	$2\theta_{100}$ (°)	FWHM <sub>meas</sub> (°)	FWHM <sub>eff</sub> (°)	$d_{100}$ (nm)	$L_a$ (nm)	$2\theta_{004}$ (°)	FWHM <sub>meas</sub> (°)	FWHM <sub>eff</sub> (°)	$2d_{004}$ (nm)	$2\theta_{110}$ (°)	FWHM <sub>meas</sub> (°)	FWHM <sub>eff</sub> (°)	$d_{110}$ (nm)	$L_a$ (nm)
R1	26.58	0.16	0.132	0.335	61.3	N/A	N/A	N/A	N/A	N/A	54.69	0.07	0.059	0.335	77.50	0.14	0.128	0.123	162.7
R2	23.07	6.67	6.670	0.385	1.2	42.70	3.23	3.234	0.212	5.4	N/A	N/A	N/A	N/A	N/A	N/A	N/A	N/A	N/A
A	24.88	4.13	4.129	0.358	1.9	N/A	N/A	N/A	N/A	N/A	54.26	0.39	0.387	0.338	N/A	N/A	N/A	N/A	N/A
B1	25.91	1.45	1.451	0.344	5.6	N/A	N/A	N/A	N/A	N/A	N/A	N/A	N/A	N/A	78.13	2.35	2.353	0.122	8.9
B2	26.10	1.17	1.168	0.341	6.9	N/A	N/A	N/A	N/A	N/A	N/A	N/A	N/A	N/A	77.72	1.24	1.237	0.123	16.9
C	26.55	0.42	0.412	0.335	19.6	N/A	N/A	N/A	N/A	N/A	54.50	0.39	0.389	0.336	77.62	0.39	0.382	0.123	54.6

### 3.4 Results from Raman spectroscopy

Raman spectra for all samples were recorded and are depicted in Fig. 22. The most striking distinction is the lack of the G'(2D) peak for both samples R2 and A. As claimed by Cuesta et al., no second-order spectrum is present for turbostratic materials [79]. In contrary, the presence of the G'(2D) peak in the samples R1, B1, B2 and C indicates a certain degree of three-dimensional order. The Raman spectra of sample B2 displays a G'(2D) peak that is shifted to slightly lower values compared to the other samples displaying the above mentioned peak.

A broad D band was observed for both R2 and A. In contrary, the four other samples displayed a rather sharp D peak of varying relative height. Since the D band is used as a measure of defects within the graphene layers, it can be ruled that samples R1 and A display the greatest amount of defects followed by sample B1 (when based on integrated peak area) [72, 73]. Rather small amounts of defects seem to be present in samples R1, B2, and C.

It was found that the G band is shifted to a slightly larger Raman shift for samples R2 and A. Ferrari and Robertson reported an increase in the G band position up to roughly  $1600 \text{ cm}^{-1}$  and an increase in the  $I_D/I_G$  ratio for "nanocrystalline carbons without a three-dimensional order" relative to the G band position of graphite [72]. This further confirms that samples R2 and A are turbostratic carbons. A decrease in the G band position and in the  $I_D/I_G$  ratio was expected for amorphous carbons, which contained mostly  $sp^2$  sites in "ring-like configurations consisting of five, six-, seven-, and eightfold disordered rings" [72].

Raman data was used to determine the positions of D, G, and G'(2D) bands. The peak intensity ratio as well as the ratio of the integrated peak areas were determined and used to estimate the crystallite size  $L_a$  according to Eq. 14. A summary of all quantitative results obtained from Raman spectroscopy is given in Table 8.

Table 8: Results of Raman spectroscopy. Crystallite size  $L_a$  is calculated based on peak height ( $L_{a,ph}$ ) and based on integrated peak area ( $L_{a,ipa}$ ).

Sample ID	Position D band ( $\text{cm}^{-1}$ )	Position G band ( $\text{cm}^{-1}$ )	Position G'(2D) band ( $\text{cm}^{-1}$ )	$(I_D/I_G)_{ph}$	$(I_D/I_G)_{ipa}$	$L_{a,ph}$ (nm)	$L_{a,ipa}$ (nm)
R1	1355.1	1586.0	2705.5	0.43	0.62	11.4	7.9
R2	1343.4	1600.4	N/A	0.88	3.11	5.6	1.6
A	1359.0	1604.3	N/A	0.86	2.66	5.8	1.9
B1	1347.3	1590.0	2695.0	0.97	1.13	5.1	4.4
B2	1348.6	1580.8	2691.1	0.35	0.64	14.2	7.8
C	1349.9	1582.4	2700.2	0.29	0.55	17.2	8.9

Fig. 23 shows the estimated average crystallize sizes  $L_a$  and  $L_c$ . The former is based on

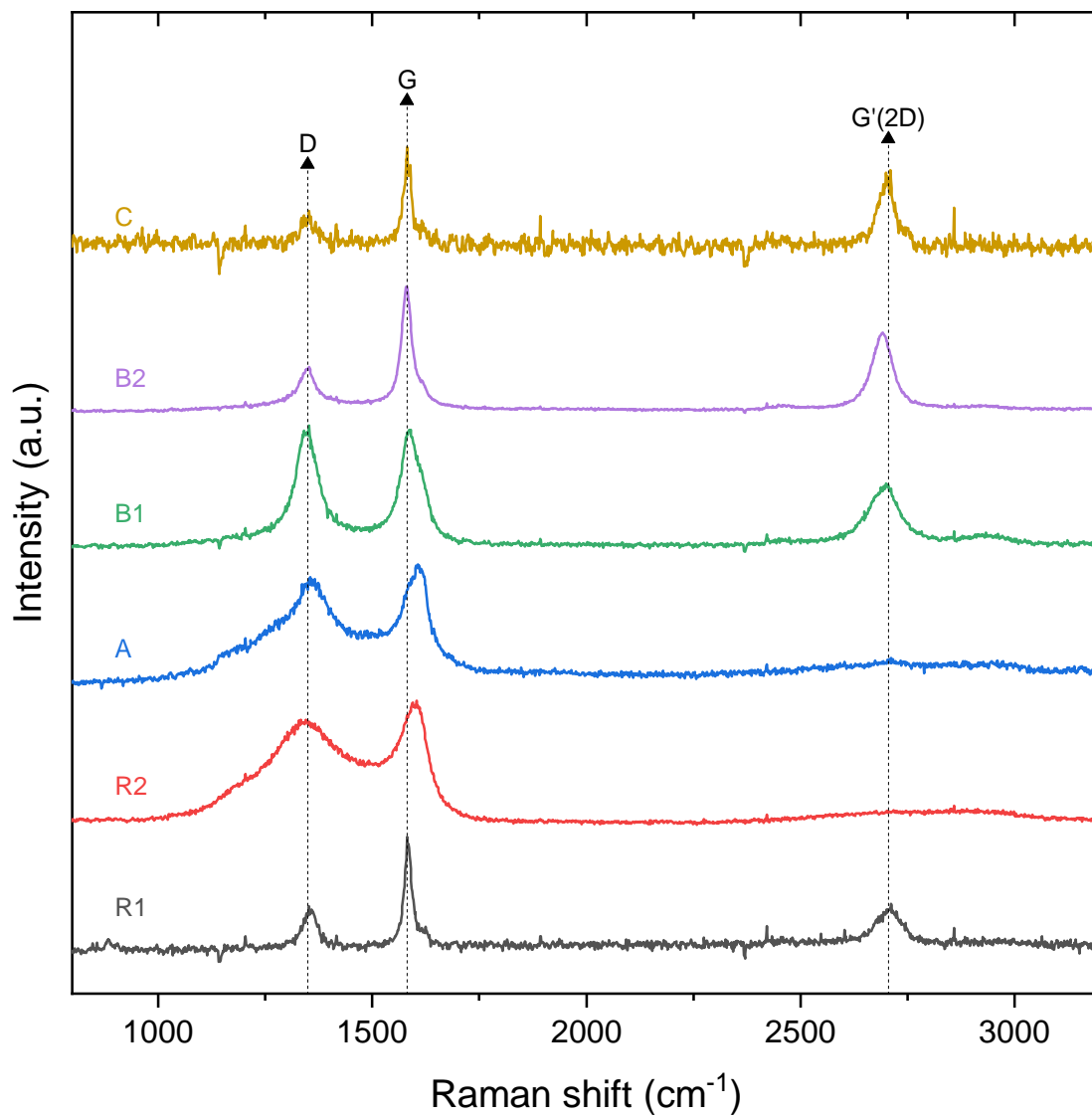


Figure 22: Comparison of Raman spectra. Black symbols denote the position of D, G and G'(2D) bands.

the analysis of two different carbon peaks in the respective X-ray diffractograms and two different evaluation procedures in Raman spectroscopy. The latter is based on XRD data only. X-ray diffraction yielded significantly larger crystallite sizes compared to Raman spectroscopy. The samples R2, A, B1, and B2 displayed a smaller range of  $L_a$  values, while The total range of  $L_a$  values was significantly smaller for samples R2, A, B1, and B2. Samples R2, A, and B1 display the lowest crystallite size  $L_a$  with average values between 2 and 5 nm. The estimates for  $L_c$  obtained from Scherrer's equation assign the largest crystallite size to sample R1 (61.3 nm) followed by sample C, similarly to the trends observed for  $L_a$ . The smallest value of 1.2 nm was obtained for sample R2, which is equal to roughly 4 graphene layers per crystallite.

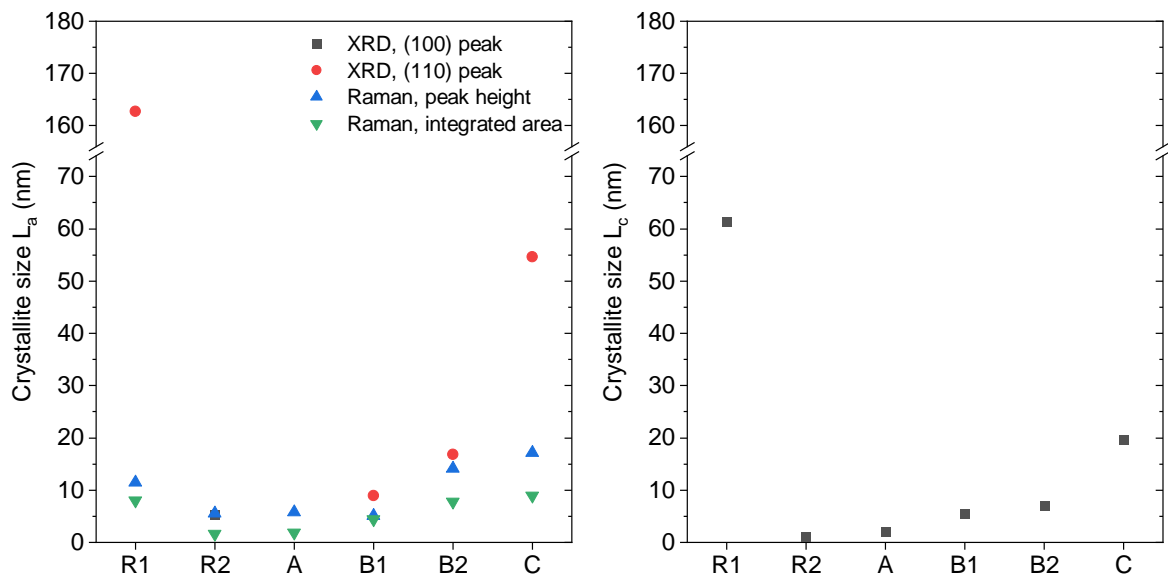


Figure 23: Crystallite sizes  $L_a$  (left) and  $L_c$  (right) based on XRD and Raman data.

### 3.5 Results from small-angle X-ray scattering

SAXS curves were recorded for all samples. As depicted in Fig. 24, all samples displayed rather featureless curves except for sample R2 which displayed a shoulder in the scattering curve. This indicates that there are no well-defined structures on the nanometer scale present, such as considerable amounts of nanopores or nanoparticles. This was later confirmed by gas sorption experiments. A power law function ( $I \propto q^{-x}$ ) was fitted to lower  $q$  values ( $q = 0.12 - 0.20 \text{ nm}^{-1}$ ) for all samples. It was found that the exponent  $x$  of the power law was slightly smaller than 4 for all samples. Porod's law suggests that scattering curves should follow a linear slope of  $q^{-3}$  or  $q^{-4}$  down to the constant background of the scattering curve [68].

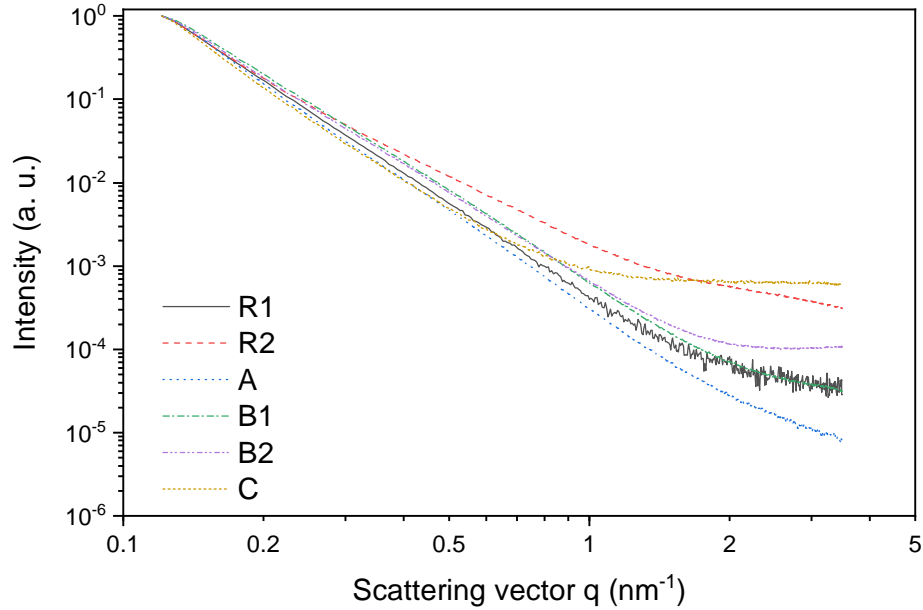


Figure 24: Experimental SAXS curves for all samples. The three measurements taken at different lateral positions were averaged. Sample R2 deviates from the rather featureless SAXS curves obtained for the other samples.

As depicted in Fig. 24, sample C displayed the strongest background and sample B2 displayed the second strongest background. It is assumed that this is related to the amount of iron in the individual samples, as the background is heavily influenced by the Fe fluorescence [98]. This may consequently be used to determine the Fe content implicitly. The largest amounts of iron impurities were in fact reported for samples C and B2. This will be discussed in chapter 3.6.

The power law function was assumed to arise mostly from the powder particles of the sample at the micrometer scale (see SEM micrographs in Fig. 17 and Fig. 18) and was subsequently subtracted from the measurement data. The remaining scattering signal is assumed to come from the nanometer scale, i.e. from nanoparticles or nanopores potentially present in the samples. A significant remaining SAXS intensity was only found for sample R2, while for all other samples the remaining signal after subtraction was negligible. This is depicted in Fig. 25. Therefore it is concluded that except for sample R2 all samples are rather structureless on length scales between 1 nm and 10 nm, which is the scale covered by SAXS measurements. Sample R2 is known to contain nanopores, which will be confirmed later on.

### 3.6 Carbon content and inorganic impurities

Fig. 26 shows the development of the sample mass as a function of temperature for various carbon samples in oxidizing atmosphere. The main mass loss occurred over a broad range

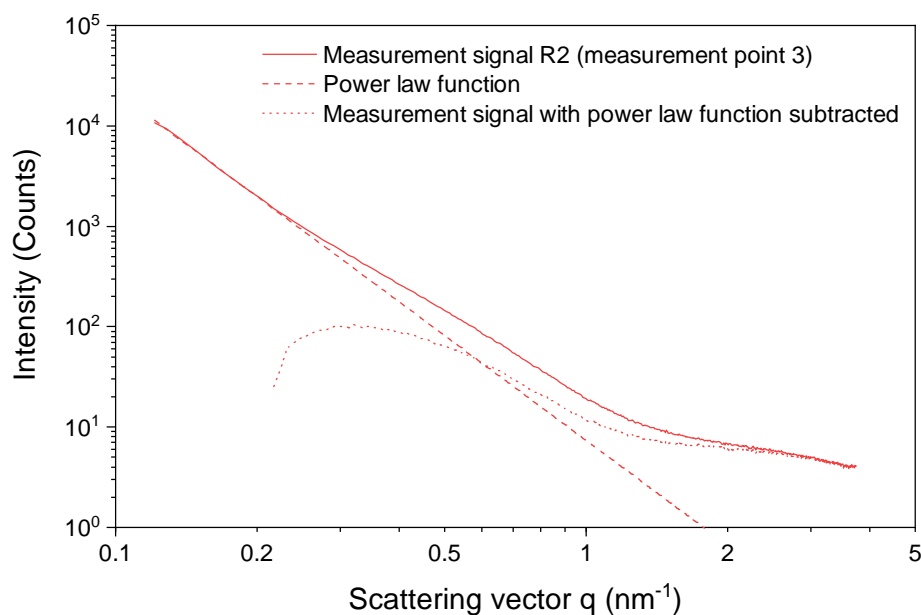


Figure 25: SAXS pattern for sample R2, measurement point 3. A power law was fitted at low  $q$  values (dashed blue line) and subtracted from the measurement data to obtain the contribution from the nanoparticles or nanopores (dotted blue line).

of temperatures from 400 °C to 1000 °C.

Sample C displays an increase in mass prior to the mass loss caused by carbon combustion. This is attributed to iron oxide formation as significant amounts of iron were detected both in EDS and XRD. A similar behavior with respect to mass gain prior to the main carbon combustion was reported by Pudukudy and Yaakob [58] when using an Fe-based catalyst. The carbon content was estimated as the difference between the total mass and the remnant. The mass loss up to 200 °C was excluded and attributed to adsorbed water. However, no significant mass loss due occurred up to 200 °C. Due to the mass increase at low temperatures, the carbon content of sample C was estimated as the difference between the maximum in recorded mass at roughly 600 °C and the remnant mass. Samples A, B1 and B2 displayed similar carbon purity levels which were determined to be between 61.7 and 68.6 wt% based on mass change. Both samples R1 and R2 displayed strikingly similar levels of carbon purity with 46.0 and 46.6 wt%, respectively. Actually, quartz may be considered to be the primary phase for both samples R1 and R2 rather than carbon, since it makes up more than half of both samples according to mass. However, it has to be noted that carbon combustion of sample R2 occurred at much lower temperatures compared to sample R1. This is explained by the much higher specific surface area of sample R2 as determined by gas sorption experiments (i.e. more surface sites available for oxidation). A similar behavior was reported for multi-walled carbon nanotubes. Multiple studies showed that a decrease in carbon nanotube diameter shifted the onset of carbon combustion to lower temperatures [99–102]. It is known from literature

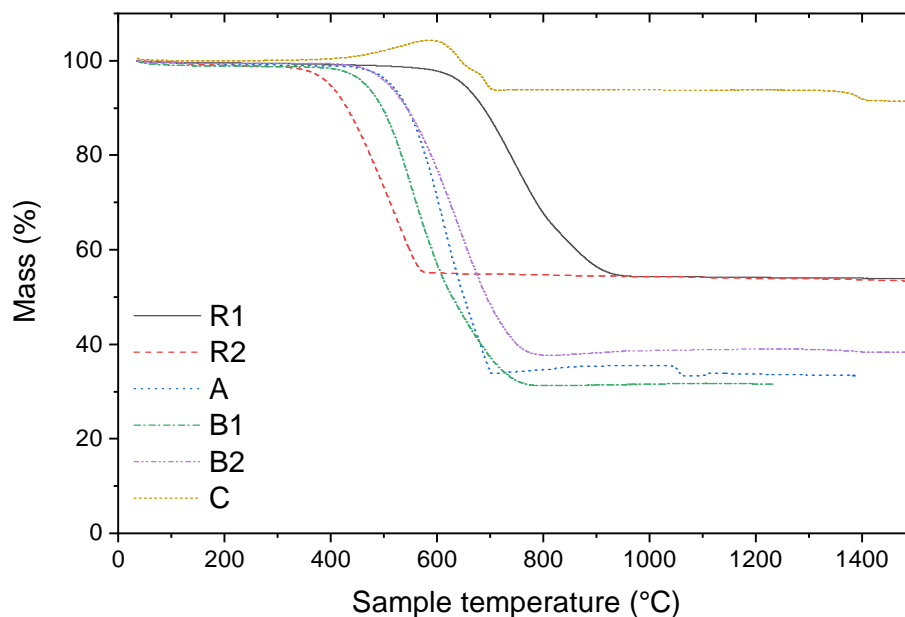


Figure 26: Mass as a function of temperature in oxidizing atmosphere. Heating was performed at  $10 \text{ K min}^{-1}$ . Mass loss is assigned to carbon combustion (i.e. formation of  $\text{CO}_2$ ).

that the temperature interval of carbon combustion is linked to the specific surface area as well as to the amount of disorder present within the sample, as an increased amount of atomic defects in the carbon structure make it more prone to oxidation [101, 103]. Multiple studies reported that amorphous carbons decompose at lower temperatures compared to graphitic particles. It has to be noted, however, that the oxidation temperature ranges of different forms of carbon are not well-defined [101, 103]. A summary of the carbon contents is given in Table 9. The residues were not analyzed. Thus, carbon bound in chemical compounds like iron carbide ( $\text{Fe}_3\text{C}$ ) was not considered for the carbon content (i.e. only the carbon in a free form).

Fig. 27 shows heat flow as a function of temperature for all aforementioned carbon samples. It has to be noted that absolute heat flow values may not be used due to the calibration error (see Chapter 2.2.8 for more details). A ranking may, however, be established within these samples. It was found that the onset of carbon combustion is shifted to lower temperatures the larger the specific surface area is (e.g. the largest specific surface area was detected for sample R2 for which carbon combustion occurred at the lowest temperature range).

For samples R1, A, B1 and C the exothermic reaction display a distinct peak over the reaction temperature range. It was reported by Dunens, MacKenzie, and Harris that the distribution of carbon nanotube products may be deducted from the oxidation peak width at half maximum [103]. A narrow peak width indicates a narrow product



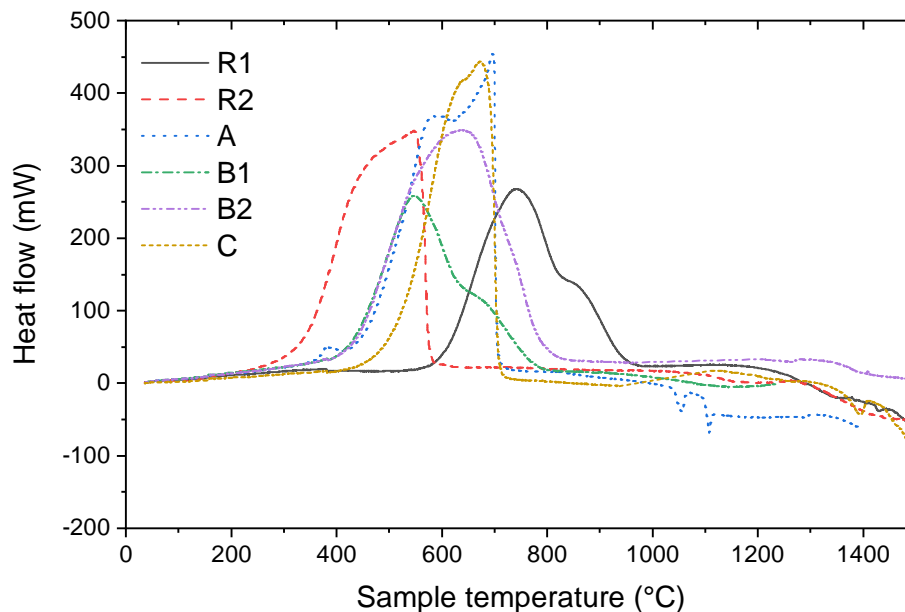


Figure 27: Heat flow as a function of temperature in oxidizing atmosphere. Heating was performed at  $10 \text{ K min}^{-1}$ . Exothermic reactions are associated with carbon combustion (i.e. formation of  $\text{CO}_x$ ).

distribution [103]. It has to be noted that no further analysis of this particular topic was performed due to the calibration error influencing the DSC measurement data in an unknown fashion. Crumpton et al. [104] showed that pure graphite is not stable beyond roughly  $950 \text{ }^\circ\text{C}$  in oxidizing atmosphere. Therefore it is assumed that reactions occurring beyond  $1000 \text{ }^\circ\text{C}$  may be attributed to reactions occurring within the impurity phases (e.g. distinctive endothermic reactions of sample A may be attributed to reactions of the main impurity phase Cu or the secondary impurity phase Zn).

### 3.7 Gas sorption analysis and BET area

Fig. 28 depicts the gas sorption behavior of the samples. All samples were measured using nitrogen at  $77 \text{ K}$  as an adsorbate with the exception of sample R2 for which carbon dioxide was used instead, as obtaining a nitrogen isotherm was not possible for this sample. Linear multi-point BET plots and the corresponding BET areas are given in Fig. 29.

All samples that were measured using  $\text{N}_2$  at  $77 \text{ K}$  displayed a mixed type II and type IV hysteresis loop based on the IUPAC classification [81]. This indicates that the investigated samples were non-porous with some capillary condensation most likely caused by particle bridging in inter-particle voids (i.e. empty space between the particles). The hysteresis loop is only weakly pronounced for all measured samples A, B1 and B2.

Based on the shape of the adsorption/desorption isotherms and the total amount of

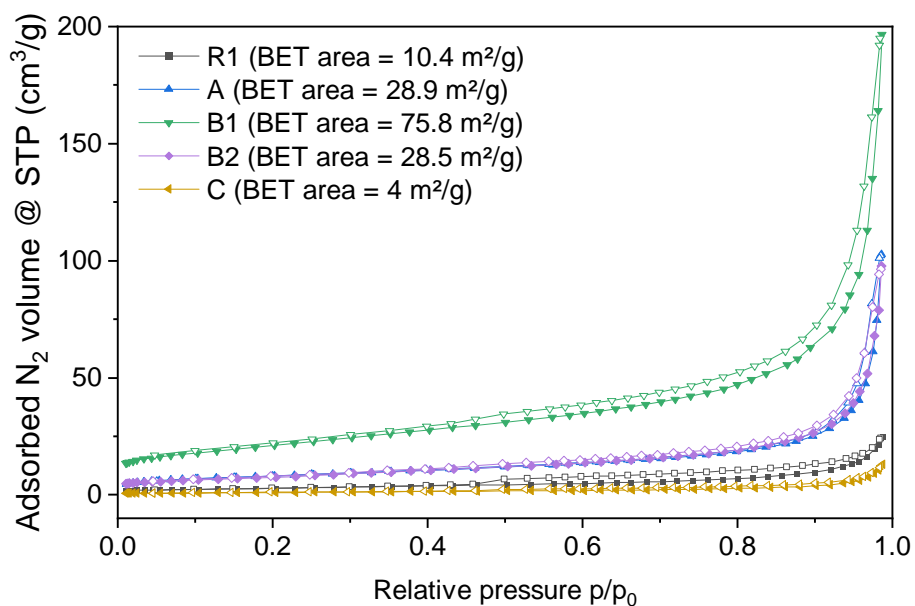


Figure 28: Results of sorption experiments using  $N_2$  at 77 K. Solid symbols denote the adsorption branch, empty symbols denote the desorption branch of the measurement. The largest BET area was calculated for sample B1 with  $75.8 \text{ m}^2 \text{ g}^{-1}$ .

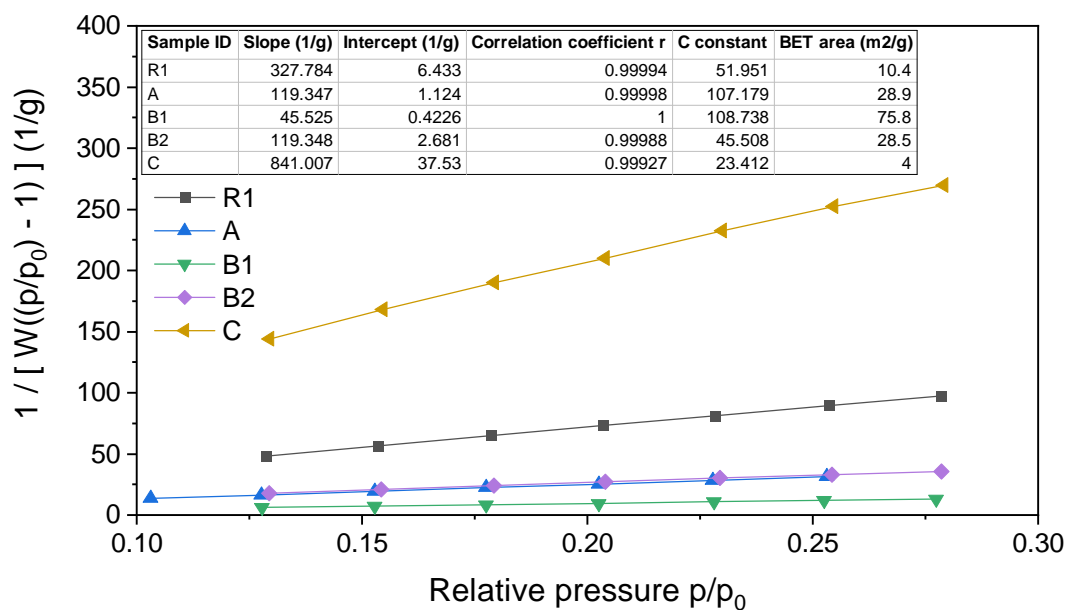


Figure 29: Linear multi-point BET plots for samples measured with  $N_2$  at 77 K.

specific surface area it was concluded that the samples do not display significant amounts of micro- or mesopores and may thus be described as non-porous (samples R1 and C) or macroporous at best (samples A and B2), as the low specific surface areas are attributed to the outer surface area of particles rather than an internal pore structure. Sample B1 might contain some micro- and mesopores. It is assumed that there is no internal pore structure present and that only external surfaces contribute to the overall BET area of samples R1, R2, A, B2, and C.

It has to be noted that the samples were measured as-delivered and no additional purification step was performed. Therefore the BET area is composed of a superposition of individual BET areas for each phase. This issue is particularly pronounced for sample C as depicted in Fig. 26. The amount of residue was estimated to be roughly 90 wt% consisting of iron and iron carbide. It is impossible to assess the contribution from each phase independently from each other. However, it has to be noted that due to the difference in crystal density the total amount of BET area is strongly limited by the purity of the sample (e.g. crystal densities of graphite and iron are  $2.26 \text{ g cm}^{-3}$  and  $7.87 \text{ g cm}^{-3}$ , respectively).

Multiple attempts at measuring sample R2 using  $\text{N}_2$  at 77 K were unsuccessful. It is assumed that no pressure equilibrium could be achieved due to the complex pore structure commonly found in biochars in combination with the very slow kinetics of  $\text{N}_2$  adsorption at 77 K. A similar issue was first reported by Rodriguez-Reinoso, de D. Lopez-Gonzalez, and Berenguer [105] in 1982. Six weeks of total measurement time were needed to obtain a full adsorption isotherm for a microporous carbon material with pore widths below 0.5 nm due to the extremely long times required for establishing an equilibrium. Jonge and Mittelmeijer-Hazeleger reported on "kinetic limitations when diffusing through the very small pores of biochar" when using  $\text{N}_2$  at 77 K [106]. Molecule size has to be taken into account as well.  $\text{CO}_2$  is capable of accessing smaller pores compared to  $\text{N}_2$ , as  $\text{CO}_2$  has a slightly smaller kinetic diameter which in combination with a higher adsorption temperature, enables higher diffusion rates and ultimately produces a better resolution of ultra-micropores (i.e. pore widths below 0.7 nm) [62, 107, 108]. It has to be noted that both  $\text{N}_2$  at 77 K and  $\text{CO}_2$  at 273 K measurements are suggested for a full characterization of biochars, as they have complementary analytical properties, especially with respect to micropores [62, 108].

A successful gas sorption experiment using  $\text{CO}_2$  at 273 K was performed. The results of the  $\text{CO}_2$  sorption experiment are depicted in Fig. 30. Both the adsorption isotherm and the differential pore volume of sample R2 are given.

The differential pore size distribution was calculated from the adsorption data us-

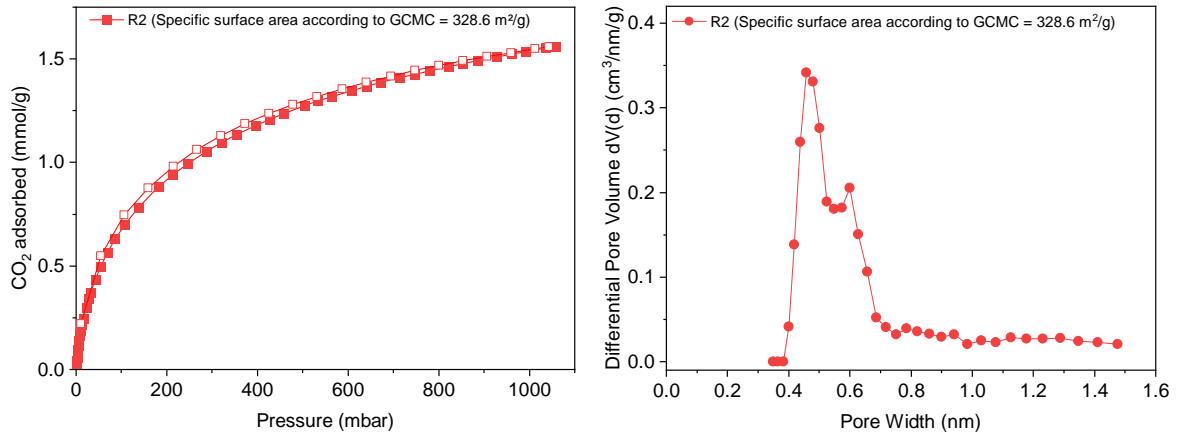


Figure 30: Results of sorption experiments using  $\text{CO}_2$  at 273 K. Adsorption isotherm of sample R2 (left, filled symbols denote the adsorption branch, empty symbols denote the desorption branch of the measurement), differential pore volume of sample R2 (right).

ing Grand Canonical Monte Carlo (GCMC) simulations, which is commonly applied to carbonaceous materials [109]. The differential pore size distribution of sample R2 ( see Fig. 30 shows a bimodal distribution of pore sizes with peaks at roughly 0.45 nm and 0.60 nm. This corresponds to ultra-microporosity and strengthened the hypothesis that due to the small pore sizes  $\text{N}_2$  could not be used successfully to record the adsorption isotherm. Based on GCMC simulations a specific surface area of  $328.6 \text{ m}^2 \text{ g}^{-1}$  was calculated. It has to be noted that  $\text{CO}_2$  measurements do not allow to estimate the specific surface area based on the multipoint BET method and should therefore not be compared directly. The BET surface areas obtained from  $\text{CO}_2$  isotherms are not very accurate in an absolute sense due to the high quadrupole moment of  $\text{CO}_2$  [110, 111].

It was found that a larger specific surface area correlates with the onset of carbon combustion at a lower temperature.

## 4 Discussion and Outlook

Within this thesis, four carbon-rich samples obtained from three different methane pyrolysis processes were investigated using advanced characterization methods and were compared to two reference materials of which one was a mineral graphite and the other was a biochar derived from the pyrolysis of biomass. It was found that all three laboratory-scaled methane pyrolysis processes yielded carbon-rich products with carbon contents between 10.3 wt% and 68.6 wt%. Impurity phases found within the samples stemmed either from the catalyst or from the reactor. The carbon allotrope detected in the metal bath process was turbostratic carbon, while the plasma-assisted process yielded a mixture of turbostratic carbon and graphite. Graphite was obtained from the fixed bed process. Based on the shape of the adsorption/desorption isotherms it was concluded that the samples are not micro- or mesoporous to a significant degree. The largest BET area detected from a carbon derived from methane pyrolysis was  $75.8 \text{ m}^2 \text{ g}^{-1}$ . A more detailed discussion of the results and a comparison to the state of the art is given in chapter 4.1. The carbon characterization methodology developed within this thesis is reviewed and an improved characterization procedure for future work is proposed in chapter 4.2. This study was the very first step with a limited amount of samples and processing parameters. It was shown that the structure of the carbon product strongly depends on the process parameters. An outlook on potential future studies is given in chapter 4.3.

### 4.1 Discussion of results

Table 9 gives an overview of the most important results obtained within this thesis.

Table 9: Summary of results.

Sample ID	Origin	Carbon allotrope	Surface area ( $\text{m}^2 \text{ g}^{-1}$ )	Carbon content (wt%)	Major impurity phases
R1	mineral graphite	graphite	10.4	46.0	$\text{SiO}_2$
R2	pyrolysis of biomass	turbostratic carbon	328.6	46.6	$\text{SiO}_2$
A	metal bath	turbostratic carbon	28.9	66.6	Cu, Zn
B1	plasma	graphite/ turbostratic carbon	75.8	68.6	Fe, $\text{Fe}_3\text{O}_4$
B2	plasma	graphite/ turbostratic carbon	28.5	61.7	Fe, $\text{Fe}_3\text{O}_4$
C	fixed bed	graphite	4.0	10.3	Fe, $\text{Fe}_3\text{C}$

Sample R1, a commercially available **mineral graphite**, was found to have an in-

terlayer distance  $d_{002}$  very close to the value of pure graphite. The X-ray diffractogram reveals a sharp, symmetric (0 0 2) carbon peak and mixed ( $h k l$ ) peaks are present. Raman data show the presence of the G'(2D) band and a comparatively weak D band indicates a graphitic structure with few defects. Thus, the carbon allotrope was classified as graphite. SEM micrographs reveal flake-like particles. A low specific surface area of  $10.4 \text{ m}^2 \text{ g}^{-1}$  was detected. TGA data show a carbon content of 46 wt%. The residue appears to consist of  $\text{SiO}_2$  and might actually be considered to be the primary phase as it constitutes more than half of the total sample mass.

Sample R2 is a **biochar** derived through pyrolysis of biomass at  $600^\circ\text{C}$ . SEM micrographs display a wide variety of irregularly shaped particles with a broad distribution of particle sizes. Determining a specific surface area using  $\text{N}_2$  was not possible.  $\text{CO}_2$  was used instead and a specific surface area of  $328.6 \text{ m}^2 \text{ g}^{-1}$  was calculated using the GCMC method. The specific surface area is close to the value of  $300 \text{ m}^2 \text{ g}^{-1}$  as provided in the product data sheet. The bimodal pore size distribution displays ultra-micropores with a pore width of roughly 0.45 nm and 0.60 nm. The asymmetric and broad (0 0 2) carbon peak and the broad (1 0 0) carbon peak in the X-ray diffractogram as well as the lack of a G'(2D) peak and a comparatively strong D band in the Raman spectrum indicate that the structure is a highly disordered turbostratic carbon. Based on a TGA experiment, a carbon content of 46.6 wt% was determined for sample R2. According to the product sheet obtained from the producer (Sonnenerde GmbH) sample R2 should consist of roughly 69 wt% of carbon and 32 wt% of water. Water was not detected at all based on the TGA data. It appears that the inorganic residue consists mostly of  $\text{SiO}_2$ , as the constituting elements are found in the EDS spectrum and the reflections of an  $\text{SiO}_2$  phase are clearly visible in the X-ray diffractogram. Based on the product sheet, the inorganic residue should make up less than 5 wt% of the sample mass. This is clearly contradicted by 53.4 wt% of inorganic residue measured in the TGA experiment.

Sample A was derived from a **metal bath process** using a Cu-Ni alloy at  $1250^\circ\text{C}$ . The carbon product was carried out with the exhaust gas and subsequently collected in a filter. The X-ray diffraction pattern of sample A reveals broad carbon peaks as well peaks related to Cu and Zn. No peaks related to Ni were discovered in the X-ray diffraction pattern. Similarly, no peak related to Ni was found in the EDS spectrum of sample A. The presence of Zn is attributed to an experiment carried out prior to the production of sample A, for which liquid Zn was used. A carbon content of roughly 66.6 wt% was determined based on TGA measurements. The lack of a G'(2D) peak in the Raman spectrum, the asymmetric shape of the (0 0 2) carbon peak and the lack of mixed ( $h k l$ ) peaks in the X-ray diffractogram yield the classification turbostratic carbon as the carbon allotrope present. The sample morphology is described by small, spherical

particles agglomerated on larger, elongated particles as shown in the SEM micrographs. The usage of Ni-based catalysts was expected to yield carbon fibers or possibly MWCNTs for sample A, while elongated particles made of turbostratic carbon were detected [58, 112–116]. However, these studies used solid catalysts in the form of nanoparticles rather than liquid ones. No literature study investigating a metal bath consisting of Cu and Ni was found. In 2019, Palmer et al. investigated a methane pyrolysis process using a molten Cu-Bi alloy, but did not report any data on the obtained carbon product [36]. In 2017, Upham et al. investigated the catalytic activity of various molten metal baths, including a mixture of Ni-Bi. Based on Raman spectroscopy and EDS measurements, graphitic carbon with roughly 92 at% carbon was reported, with Bi and Ni as impurity phases [35]. In this study, the carbon product was removed from the metal-gas interface, while sample A was carried out with the exhaust gas and collected in a filter system. Rahimi et al. reported a carbon content of roughly 68 wt% using X-ray fluorescence for carbon produced from a Ni-Bi bath with a layer of molten KBr on top of the liquid metal alloy [38]. It has to be noted, however, that washing steps were applied prior to the measurements. This is in a similar range as the 66.6 wt% carbon content reported for sample A. Based on multiple reports in literature it is assumed that a higher carbon content is possible and might be achieved from an improved carbon removal method [35, 38]. The morphology of the carbon product reported by Rahimi et al. was described as predominantly sheet-like [38], compared to rather elongated particles of sample A. It is unknown, whether carbon fibers may be obtained from the liquid metal process.

Samples B1 and B2 were both derived from a **plasma-based process** using two different sets of process parameters. The carbon content was determined to be 68.6 wt% and 61.7 wt% respectively. Based on EDS and XRD data, the impurity phases Fe and  $\text{Fe}_3\text{O}_4$  were detected. It is assumed that the iron originates from the reactor used for the experiments. Classifying the carbon of samples B1 and B2 was inconclusive. The X-ray diffractograms displayed (002) carbon peaks in between the asymmetric, broad shapes of samples R2 and A and the symmetric, sharp (002) carbon peaks of samples R1 and C. The clearly visible (102) carbon peak indicates graphite, while the rather broad (110) carbon peak indicates turbostratic carbon. Raman spectroscopy revealed a pronounced  $G'(2D)$  peak for both sample B1 and B2 indicating graphite as the major carbon allotrope. The Raman spectrum of sample B1 shows a more dominant D peak compared to B2 indicating more defects in the crystallographic structure. Based on these results, it is assumed that the carbon present in both samples B1 and B2 is a mixture of graphite and turbostratic carbon. It has to be noted that sample B2 displays a higher degree of ordering compared to sample B1 as evidenced by the larger crystallite sizes  $L_a$  and  $L_c$ , the more symmetric (002) carbon peak in the X-ray diffractogram and a stronger

G'(2D) band in the Raman spectrum. In literature, multiple reports focus on the production of carbon black from a plasma process and neglect hydrogen production [41–44]. Kim et al. reported nanostructured sheet-like turbostratic carbons with a BET area of roughly  $45 \text{ m}^2 \text{ g}^{-1}$  in a process optimized for production of solid carbon. SEM micrographs of the carbon microstructure displayed remarkable similarities to the ones obtained for samples B1 and B2. The microstructure was described as coral-like [46]. Tsai and Chen reported spheroidally shaped particles with roughly 50 nm in size, aggregated together to form particles [47]. Muradov et al. reported carbon aerosols obtained in a non-thermal plasma process [48]. The microstructure was described as sponge-like and based on SEM micrographs remarkable similarities in terms of morphology to samples B1 and B2 were found, similarly to the study of Kim et al. [46, 48]. The carbon product obtained by Muradov et al. displayed a BET area of  $130\text{-}150 \text{ m}^2 \text{ g}^{-1}$ . The Raman spectra obtained from the carbon aerosols displayed very weak D and G band peaks. The carbon structure was described as "highly disordered" [48]. The BET area of sample B1 is the largest from the investigated carbon samples derived from methane pyrolysis at  $75.8 \text{ m}^2 \text{ g}^{-1}$  with sample B2 having roughly one third of that BET area at  $28.5 \text{ m}^2 \text{ g}^{-1}$ . Carbons derived from the plasma process are the most promising candidates for applications requiring a large specific surface area, as they displayed the largest BET area investigated within this thesis as well as the largest carbon content. It has to be noted, however, that significantly larger specific surface areas than  $75.8 \text{ m}^2 \text{ g}^{-1}$  are required for multiple high-tech applications including hydrogen storage, selective gas separation, electrochemical energy storage in supercapacitors, and water purification. This may be achieved in a subsequent activation step.

Sample C was derived from a **fixed bed process** utilizing reduced iron ore pellets as a catalyst at  $800 \text{ }^\circ\text{C}$ . The X-ray diffraction pattern shows that iron carbide ( $\text{Fe}_3\text{C}$ ) and iron (Fe) are present besides carbon. A carbon content of only 10.3 wt% was detected for sample C using TGA. The TGA data show an increase in mass prior to carbon combustion that is most likely caused by iron oxide formation. This sample contains the largest quantity of heavy elements and consequently was found to have the largest poured bulk density. The dispersion study showed corrosion of iron in distilled water. SEM micrographs show aggregated particles that appear to have a smooth surface. Gas sorption measurements of sample C yielded the lowest BET area of all investigated samples with just  $4.0 \text{ m}^2 \text{ g}^{-1}$ . Due to the presence of a G'(2D) peak in the Raman spectrum and a symmetric, sharp (002) carbon peak as well as the presence of a mixed (112) carbon peak, the carbon phase of sample C is classified as graphite. The morphology of sample C is described as agglomerated particles. Most studies using Fe-based catalysts in a fixed bed process classified the carbon product as carbon nanotubes [54–57, 60]. It has to be



noted, however, that the catalysts used in those studies contained nanoparticles or finely dispersed metals differing from the reduced iron ore used for the synthesis of sample C. Konieczny et al. prepared a catalyst by reduction of magnetite ( $\text{Fe}_3\text{O}_4$ ) used for the subsequent methane decomposition in a fixed bed reactor at temperatures from 800 to 900 °C [55]. SEM micrographs revealed the formation of carbon nanofibers and smooth, elliptical plates. The BET area of the carbon product was determined to be  $8.6 \text{ m}^2 \text{ g}^{-1}$ , which is in the same order of magnitude as the BET area of sample C [55]. Multiple studies reported the formation of a minor  $\text{Fe}_3\text{C}$  phase fraction [56, 58–60]. Only some studies conducted TGA studies for the carbon product characterization. Awadallah et al. reported a carbon content of roughly 90 wt% for an MgO-based catalyst covered with Fe-Co, and a carbon content of roughly 80 wt% for an MgO-based catalyst covered with Ni-Fe [57]. TGA experiments conducted by Pudukudy and Yaakob revealed a carbon content of roughly 60 wt% and a minor increase in mass prior to the main carbon combustion event [58]. Torres, Pinilla, and Suelves published a carbon content of 82 wt% for experiments conducted with an  $\text{Al}_2\text{O}_3$ -supported catalyst covered in Fe [60]. It has to be noted that in all cases the catalyst was not removed prior to the analysis, no procedure for separating the carbon from the catalyst was proposed, and the remnant remaining after TGA analysis was not analyzed [57, 58, 60]. The most urgent task for the fixed bed methane pyrolysis process is separating the reduced iron ore catalyst from the carbon that is growing on top of it. It does not seem likely that carbon nanotubes or carbon filaments may be obtained from a reduced iron ore catalyst, as synthesizing carbon nanotubes or carbon filaments required finely dispersed metals on the catalysts surface [54–57, 60].

## 4.2 Improved characterization procedure for future work

In this chapter the carbon characterization methodology developed and applied within this thesis is reviewed and areas of improvement are proposed. As research on the various methane pyrolysis processes is planned to continue for years to come, many more samples will have to be investigated in future studies. In order to improve the efficiency of such tasks an optimized protocol for determining the most important structure-property relationships for carbons derived from methane pyrolysis is proposed in this chapter.

The characterization methods employed during this thesis are ranked according to three criteria: Importance (I), availability (A), and measurement time (M). The results are summarized in Table 10.

Defining a ranking criterion is a delicate task and ultimately somewhat arbitrary, as it is based on personal experiences during the work on this thesis. However, it was assumed

that the *importance* of the measurement and the *availability* of measurement equipment at Montanuniversität Leoben are more relevant than the actual *measurement time*. In this context, *importance* of the measurement refers to the relevance of the data obtained through each characterization method. As an example, determining the carbon allotrope is a key research question. This may be done by examining the diffractogram obtained through XRD or by investigating the Raman spectrum. However, XRD gives additional information on other phases present. Thus, XRD was rated with a higher *importance* compared to Raman spectroscopy. It has to be noted that applying complementary techniques (e.g. XRD and Raman spectroscopy) minimizes the risk of misinterpretation of data. The overall ranking criterion was determined to be  $I^2 \times A^2 \times M$ .

Ultimately it is believed that X-ray diffraction is the most important characterization technique as both the phase composition and the carbon allotrope can be estimated based on the diffraction pattern only. XRD is a versatile technique that is quite fast compared to multiple other measurement techniques and measurement equipment is readily available. However, it has to be noted that for high-purity carbon samples the additional information obtained on other phases will be of lesser importance. SEM was found to be indispensable for assessing the morphology while EDS was important for determining the chemical elements qualitatively.

Raman spectroscopy was found to be the an important characterization technique, as it allows to make estimates about the crystallite size, amount of defects, and the carbon allotrope in a non-destructive and quick way. Limited access to the device may pose, however, a significant risk to the project and limits the speed of scientific progress. In order to ensure a quick and efficient scientific working procedure it is heavily recommended to find a solution to the accessibility problem for Raman spectroscopy.

Small angle X-ray scattering did not find structures on the nanometer scale. This is in good agreement with gas sorption experiments that did not show a microporous structure for carbons derived from methane pyrolysis. Carbons with a microporous structure, once obtained either directly from methane pyrolysis or after a subsequent activation process, will require both SAXS and gas sorption analysis for characterization purposes. This was demonstrated by the interesting results for the biomass-derived sample R2.

Differential scanning calorimetry offered complementary information on the carbon combustion process as an addition to the important data obtained from thermogravimetric analysis Poured bulk density measurements and optical microscopy and dispersion studies were found to be less important for future works as the data gained from utilizing those methods is of restricted scientific value in the present context.

During the course of this thesis it was found that the analytical methods employed for

Table 10: Ranking criterion for carbon characterization methods

Ranking	Method	Importance	Availability	Measurement time	Ranking criterion
		I	A	M	$I^2 \times A^2 \times M$
1	X-ray diffraction	10	9	7	56700
2	scanning electron microscopy	10	6	7	25200
3	energy dispersive X-ray spectroscopy	8	6	7	16128
4	Raman spectroscopy	8	5	10	16000
5	small-angle X-ray scattering	5	8	7	11200
6	gas sorption measurement	8	7	3	9408
7	thermogravimetric analysis	10	3	5	4500
8	poured bulk density	2	10	9	3600
9	differential scanning calorimetry	5	4	5	2000
10	Optical microscopy	1	9	9	729
11	dispersion study	2	10	1	400

determining the chemical composition are insufficient or partly even contradictory. Energy dispersive X-ray spectroscopy was applied to obtain the chemical elements present in the sample. However, quantitative statements about the chemical composition cannot be made as the sample is in powder form and has a rough surface. A quantitative measurement using EDS would require a smooth surface and a calibration standard. Additionally, only heavy elements can be measured with reasonable accuracy. Carbon and oxygen contents remain vague and hydrogen cannot be detected at all [95]. Additionally, EDS detects only elements on the surface, so an implicit assumption about a homogeneous chemical composition of individual particles has to be made. This assumption is not adequate as all samples were found to contain significant fractions of impurities which may be distributed heterogeneously within individual particles. In case of sample C carbon grows on top of the iron substrate thereby rendering the results from a surface-sensitive EDS analysis even more questionable.

An alternative method to overcome some of the limitations posed by EDS would be X-ray photoelectron spectroscopy (XPS) which is a surface-sensitive technique that allows to establish the chemical composition and the electronical states of near-surface atoms (typical depths: 1 nm - 20 nm) with greatly improved accuracy. Only hydrogen and helium cannot be measured using this technique. However, cost for analysis is significantly higher and data on the chemical composition of the particle cross-section cannot be obtained. Thus, it is considered unsuitable for the task at hand, as it is not possible to determine the bulk composition [117].

A workaround to overcome this obstacle would be preparing a metallographically polished specimen. A trial run was performed unsuccessfully, as individual particles broke loose from the embedding material. The latter would cause additional issues when trying to determine the chemical composition of samples.

Assessing the carbon content based on TGA experiments has proven to be the most

reliable method. Mass change as a function of temperature yields reliable results. However, mass gain due to metal oxide formation (e.g.  $\text{Fe}_3\text{O}_4$ ) was detected in some samples. If temperature intervals of metal oxide formation and carbon combustion were to overlap, both effects cannot be separated from each other yielding a wrong assessment of the overall carbon content. Future studies will have to tackle this issue by investigating the residue. During this thesis, as only small sample quantities were investigated as the total amounts of residue were not sufficient for an adequate post analysis. However, a furnace in an oxidizing atmosphere may be used to obtain larger quantities of residue under similar heating conditions, allowing to properly assess the residue. By measuring the sample mass before and after oxidation in the furnace, an additional estimate for the carbon content could be obtained, which would be based on larger quantities of sample mass compared to TGA. This would yield a result independent of potential heterogeneity present within individual samples.

Additional techniques that may be used to determine the chemical composition include inductively coupled plasma optical emission spectrometry (ICP-OES) and inductively coupled plasma mass spectrometry (ICP-MS) as well as wet chemical analysis [118].

### 4.3 Outlook

This work investigated four samples derived from different methane pyrolysis processes on the laboratory scale. The carbons derived from methane pyrolysis were found to be turbostratic carbon (sample A, liquid metal process using a mixture of Cu and Ni as catalyst), a mixture of graphite and turbostratic carbon (plasma-process-based samples B1 and B2), and graphite (sample C, fixed bed process using reduced iron ore as a catalyst). While there were some traces of filaments present in samples B1 and B2, no further evidence suggesting the presence of "exotic" carbon allotropes like carbon nanotubes, fullerenes, or single layer graphene was detected.

All carbons contained significant amount of impurities between 31.4 wt% and 89.7 wt%. The impurities stemmed either from the catalyst or from the reactor. For future applications the current carbon purity level is not sufficient and must be improved significantly to allow commercial utilization. For the metal bath process and the plasma-assisted process improved collecting protocols should be investigated. In case of the fixed bed process a method for separating the catalyst and the carbon product should be developed. An additional purification step might be a viable option for all three processes.

Sample B1 displayed a BET area of  $75.8 \text{ m}^2 \text{ g}^{-1}$  and a carbon content of 68.6 wt% and was synthesized using the plasma-assisted process. Based on the results obtained within

this thesis it seems that this methane pyrolysis process is the most promising process for delivering high purity carbons with a large BET area. A well-developed pore structure on the nanometer scale and a significantly increased specific surface area are prerequisites for carbons derived by methane pyrolysis for utilization as a substitute for biochar or in high-tech applications including gas storage, selective gas separation, electrochemical energy storage, and water purification. Based on the available data it appears unlikely that this might be achieved directly through a methane pyrolysis process, as no significant meso- or microporosity was detected and only external surfaces contributed to the detected BET area. Physical or chemical activation might be applied in a subsequent step to yield carbons for more demanding applications. It has to be noted, however, that both chemical and physical activation release significant amounts of burn-off from the carbon product as carbon dioxide and carbon monoxide and thus cannot be considered to be climate-neutral [119, 120].

A successful commercialization of carbons derived from methane pyrolysis along with the large-scale industrial application of the methane pyrolysis process for hydrogen production poses a significant step towards a more sustainable, climate-neutral energy production.

## References

- [1] United Nations. *Adoption of the Paris Agreement*. Tech. rep. 2015.
- [2] European Commission. *The European Green Deal*. Tech. rep. 9. 2019, p. 24. DOI: <https://doi.org/10.1017/CB09781107415324.004>.
- [3] European Commission. *A hydrogen strategy for a climate-neutral Europe*. Tech. rep. European Commission, 2020.
- [4] A. Körner, C. Tam, S. Bennett, and J. Gagné. *Technology Roadmap Hydrogen and Fuel Cells*. Tech. rep. Paris, 2015.
- [5] T. Keipi, K. E. S. Tolvanen, H. Tolvanen, and J. Konttinen. „Thermo-catalytic decomposition of methane: The effect of reaction parameters on process design and the utilization possibilities of the produced carbon“. In: *Energy Conversion and Management* 126 (2016), pp. 923–934. DOI: <https://doi.org/10.1016/j.enconman.2016.08.060>.
- [6] Department of Energy United States and H. Economy. *Roadmap on manufacturing R&D for the hydrogen economy*. Tech. rep. Washington, D.C.: Department of Energy United States, 2005.
- [7] N. Z. Muradov and T. N. Veziroglu. „"Green" path from fossil-based to hydrogen economy: An overview of carbon-neutral technologies“. In: *International Journal of Hydrogen Energy* 33.23 (2008), pp. 6804–6839. DOI: <https://doi.org/10.1016/j.ijhydene.2008.08.054>.
- [8] N. Muradov. „Low to near-zero CO<sub>2</sub> production of hydrogen from fossil fuels: Status and perspectives“. In: *International Journal of Hydrogen Energy* 42.20 (2017), pp. 14058–14088. DOI: <https://doi.org/10.1016/j.ijhydene.2017.04.101>.
- [9] N. Z. Muradov and T. N. Veziroglu. „From hydrocarbon to hydrogen-carbon to hydrogen economy“. In: *International Journal of Hydrogen Energy* 30.3 (2005), pp. 225–237. DOI: <https://doi.org/10.1016/j.ijhydene.2004.03.033>.
- [10] H. F. Abbas and W. M. A. W. Daud. „Hydrogen production by methane decomposition: A review“. In: *International Journal of Hydrogen Energy* 35.3 (2010), pp. 1160–1190. DOI: <https://doi.org/10.1016/j.ijhydene.2009.11.036>.
- [11] Y. Li, D. Li, and G. Wang. „Methane decomposition to CO<sub>x</sub>-free hydrogen and nano-carbon material on group 8-10 base metal catalysts: A review“. In: *Catalysis Today* 162.1 (2011), pp. 1–48. DOI: <https://doi.org/10.1016/j.cattod.2010.12.042>.

- [12] A. Abánades, C. Rubbia, and D. Salmieri. „Technological challenges for industrial development of hydrogen production based on methane cracking“. In: *Energy* 46.1 (2012), pp. 359–363. DOI: <http://doi.org/10.1016/j.energy.2012.08.015>.
- [13] U. P. M. Ashik, W. M. A. Wan Daud, and H. F. Abbas. „Production of greenhouse gas free hydrogen by thermocatalytic decomposition of methane â€“ A review“. In: *Renewable and Sustainable Energy Reviews* 44 (2015), pp. 221–256. DOI: <https://doi.org/10.1016/j.rser.2014.12.025>.
- [14] B. Parkinson, J. W. Matthews, T. B. McConnaughy, D. C. Upham, and E. W. McFarland. „Techno-Economic Analysis of Methane Pyrolysis in Molten Metals: Decarbonizing Natural Gas“. In: *Chemical Engineering & Technology* 40.6 (June 2017), pp. 1022–1030. DOI: <https://doi.org/10.1002/ceat.201600414>.
- [15] V. E. Parfenov, N. V. Nikitchenko, A. A. Pimenov, A. E. Kuz'min, M. V. Kulikova, O. B. Chupichev, and A. L. Maksimov. „Methane Pyrolysis for Hydrogen Production: Specific Features of Using Molten Metals“. In: *Russian Journal of Applied Chemistry* 93.5 (2020), pp. 625–632. DOI: <https://doi.org/10.1134/S1070427220050018>.
- [16] J. X. Qian, T. W. Chen, L. R. Enakonda, D. B. Liu, G. Mignani, J.-M. Basset, and L. Zhou. „Methane decomposition to produce COx-free hydrogen and nano-carbon over metal catalysts: A review“. In: *International Journal of Hydrogen Energy* 45.15 (2020), pp. 7981–8001. DOI: <https://doi.org/10.1016/j.ijhydene.2020.01.052>.
- [17] S. Schneider, S. Bajohr, F. Graf, and T. Kolb. „State of the Art of Hydrogen Production via Pyrolysis of Natural Gas“. In: *Chemie Ingenieur Technik* 92.8 (2020), pp. 1023–1032. DOI: <https://doi.org/10.1002/cite.202000021>.
- [18] E. H. L. Falcao and F. Wudl. „Carbon allotropes: beyond graphite and diamond“. In: *Journal of Chemical Technology & Biotechnology: International Research in Process, Environmental & Clean Technology* 82.6 (2007), pp. 524–531. DOI: <https://doi.org/10.1002/jctb.1693>.
- [19] E. H. L. Falcao. „Carbonaceous materials with exotic morphologies“. PhD thesis. University of California, Los Angeles, 2006.
- [20] K. S. Novoselov, A. K. Geim, S. V. Morozov, D. Jiang, Y. Zhang, S. V. Dubonos, I. V. Grigorieva, and A. A. Firsov. „Electric Field Effect in Atomically Thin Carbon Films“. In: *Science* 306.5696 (Oct. 2004), 666 LP –669. DOI: <https://doi.org/10.1126/science.1102896>.

- [21] A. K. Geim and K. S. Novoselov. „The rise of graphene“. In: *Nanoscience and Technology*. Co-Published with Macmillan Publishers Ltd, UK, Aug. 2009, pp. 11–19. DOI: [https://doi.org/10.1142/9789814287005\\_0002](https://doi.org/10.1142/9789814287005_0002).
- [22] P. Delhaes. *Graphite and precursors*. Ed. by P. Delhaes. Vol. 1. Gordon & Breach Science Publishers, 2001.
- [23] O. Paris. *Structure and Multiscale Mechanics of Carbon Nanomaterials*. Springer, 2016.
- [24] B. E. Warren. „X-Ray Diffraction in Random Layer Lattices“. In: *Phys. Rev.* 59.9 (May 1941), pp. 693–698. DOI: <https://doi.org/10.1103/PhysRev.59.693>.
- [25] V. A. da Silva, M. C. Rezende, V. A. da Silva, and M. C. Rezende. „Effect of the Morphology and Structure on the Microwave Absorbing Properties of Multiwalled Carbon Nanotube Filled Epoxy Resin Nanocomposites“. In: *Materials Research* 21.5 (July 2018). DOI: <https://doi.org/10.1590/1980-5373-mr-2017-0977>.
- [26] H. O. Pierson. *Handbook of carbon, graphite, diamond and fullerenes*. Ed. by H. O. Pierson. Oxford: William Andrew Publishing, 1993, pp. viii–ix. DOI: <https://doi.org/10.1016/B978-0-8155-1339-1.50005-0>.
- [27] D. Tyrer. „Production of hydrogen“. In: *USA Patent US1803221 A* (1931).
- [28] M. Steinberg. „Fossil fuel decarbonization technology for mitigating global warming“. In: *International Journal of Hydrogen Energy* 24.8 (1999), pp. 771–777. DOI: [https://doi.org/10.1016/S0360-3199\(98\)00128-1](https://doi.org/10.1016/S0360-3199(98)00128-1).
- [29] M. Serban, M. A. Lewis, C. L. Marshall, and R. D. Doctor. „Hydrogen Production by Direct Contact Pyrolysis of Natural Gas“. In: *Energy & Fuels* 17.3 (May 2003), pp. 705–713. DOI: <https://doi.org/10.1021/ef020271q>.
- [30] T. Geißler et al. „Hydrogen production via methane pyrolysis in a liquid metal bubble column reactor with a packed bed“. In: *Chemical Engineering Journal* 299 (2016), pp. 192–200. DOI: <https://doi.org/10.1016/j.cej.2016.04.066>.
- [31] M. Plevan, T. Geißler, A. Abánades, K. Mehravaran, R. K. Rathnam, C. Rubbia, D. Salmieri, L. Stoppel, S. Stückrad, and T. Wetzel. „Thermal cracking of methane in a liquid metal bubble column reactor: Experiments and kinetic analysis“. In: *International Journal of Hydrogen Energy* 40.25 (2015), pp. 8020–8033. DOI: <https://doi.org/10.1016/j.ijhydene.2015.04.062>.
- [32] I. Schultz and D. W. Agar. „Decarbonisation of fossil energy via methane pyrolysis using two reactor concepts: Fluid wall flow reactor and molten metal capillary reactor“. In: *International Journal of Hydrogen Energy* 40.35 (2015), pp. 11422–11427. DOI: <https://doi.org/10.1016/j.ijhydene.2015.03.126>.



- [33] B. J. Leal Pérez, J. A. Medrano Jiménez, R. Bhardwaj, E. Goetheer, M. van Sint Annaland, and F. Gallucci. „Methane pyrolysis in a molten gallium bubble column reactor for sustainable hydrogen production: Proof of concept & techno-economic assessment“. In: *International Journal of Hydrogen Energy* 46.7 (2021), pp. 4917–4935. DOI: <https://doi.org/10.1016/j.ijhydene.2020.11.079>.
- [34] G. Wang, X. Shen, B. Wang, J. Yao, and J. Park. „Synthesis and characterisation of hydrophilic and organophilic graphene nanosheets“. In: *Carbon* 47.5 (2009), pp. 1359–1364. DOI: <https://doi.org/10.1016/j.carbon.2009.01.027>.
- [35] D. C. Upham, V. Agarwal, A. Khechfe, Z. R. Snodgrass, M. J. Gordon, H. Metiu, and E. W. McFarland. „Catalytic molten metals for the direct conversion of methane to hydrogen and separable carbon“. In: *Science* 358.6365 (Nov. 2017), pp. 917–921. DOI: <https://doi.org/10.1126/science.aao5023>.
- [36] C. Palmer, M. Tarazkar, H. H. Kristoffersen, J. Gelinas, M. J. Gordon, E. W. McFarland, and H. Metiu. „Methane pyrolysis with a molten Cu-Bi alloy catalyst“. In: *Acs Catalysis* 9.9 (2019), pp. 8337–8345. DOI: <https://doi.org/10.1021/acscatal.9b01833>.
- [37] A. V. Gulevich, P. N. Martynov, V. A. Gulevsky, and V. V. Ulyanov. „Technologies for hydrogen production based on direct contact of gaseous hydrocarbons and evaporated water with molten Pb or Pb-Bi“. In: *Energy Conversion and Management* 49.7 (2008), pp. 1946–1950. DOI: <https://doi.org/10.1016/j.enconman.2007.12.028>.
- [38] N. Rahimi, D. Kang, J. Gelinas, A. Menon, M. J. Gordon, H. Metiu, and E. W. McFarland. „Solid carbon production and recovery from high temperature methane pyrolysis in bubble columns containing molten metals and molten salts“. In: *Carbon* 151 (2019), pp. 181–191. DOI: <https://doi.org/10.1016/j.carbon.2019.05.041>.
- [39] D. Kang, N. Rahimi, M. J. Gordon, H. Metiu, and E. W. Mcfarland. „Catalytic methane pyrolysis in molten MnCl<sub>2</sub>-KCl“. In: *Applied Catalysis B: Environmental* 254. February (2019), pp. 659–666. DOI: <https://doi.org/10.1016/j.apcatb.2019.05.026>.
- [40] D. Kang, C. Palmer, D. Mannini, N. Rahimi, M. J. Gordon, H. Metiu, and E. W. McFarland. „Catalytic Methane Pyrolysis in Molten Alkali Chloride Salts Containing Iron“. In: *ACS Catalysis* 10.13 (July 2020), pp. 7032–7042. DOI: <https://doi.org/10.1021/acscatal.0c01262>.

- [41] L. Fulcheri and Y. Schwob. „From methane to hydrogen, carbon black and water“. In: *International Journal of Hydrogen Energy* 20.3 (1995), pp. 197–202. DOI: [https://doi.org/10.1016/0360-3199\(94\)E0022-Q](https://doi.org/10.1016/0360-3199(94)E0022-Q).
- [42] F. Fabry, G. Flamant, and L. Fulcheri. „Carbon black processing by thermal plasma. Analysis of the particle formation mechanism“. In: *Chemical Engineering Science* 56.6 (2001), pp. 2123–2132. DOI: [https://doi.org/10.1016/S0009-2509\(00\)00486-3](https://doi.org/10.1016/S0009-2509(00)00486-3).
- [43] J. R. Fincke, R. P. Anderson, T. A. Hyde, and B. A. Detering. „Plasma Pyrolysis of Methane to Hydrogen and Carbon Black“. In: *Industrial & Engineering Chemistry Research* 41.6 (Mar. 2002), pp. 1425–1435. DOI: <https://doi.org/10.1021/ie010722e>.
- [44] L. Fulcheri, N. Probst, G. Flamant, F. Fabry, E. Grivei, and X. Bourrat. „Plasma processing: a step towards the production of new grades of carbon black“. In: *Carbon* 40.2 (2002), pp. 169–176. DOI: [https://doi.org/10.1016/S0008-6223\(01\)00169-5](https://doi.org/10.1016/S0008-6223(01)00169-5).
- [45] S. I. Choi, J. S. Nam, J. I. Kim, T. H. Hwang, J. H. Seo, and S. H. Hong. „Continuous process of carbon nanotubes synthesis by decomposition of methane using an arc-jet plasma“. In: *Thin Solid Films* 506-507 (2006), pp. 244–249. DOI: <https://doi.org/10.1016/j.tsf.2005.08.022>.
- [46] K. S. Kim, S. H. Hong, K. Lee, and W. T. Ju. „Continuous Synthesis of Nanostructured Sheetlike Carbons by Thermal Plasma Decomposition of Methane“. In: *IEEE Transactions on Plasma Science* 35.2 (2007), pp. 434–443. DOI: <https://doi.org/10.1109/TPS.2007.892556>.
- [47] C.-h. Tsai and K.-t. Chen. „Production of hydrogen and nano carbon powders from direct plasmalysis of methane“. In: *International Journal of Hydrogen Energy* 34.2 (2009), pp. 833–838. DOI: <https://doi.org/10.1016/j.ijhydene.2008.10.061>.
- [48] N. Muradov, F. Smith, G. Bockerman, and K. Scammon. „Thermocatalytic decomposition of natural gas over plasma-generated carbon aerosols for sustainable production of hydrogen and carbon“. In: *Applied Catalysis A: General* 365.2 (2009), pp. 292–300. DOI: <https://doi.org/10.1016/j.apcata.2009.06.031>.
- [49] H. Zhang, T. Cao, and Y. Cheng. „Preparation of few-layer graphene nanosheets by radio-frequency induction thermal plasma“. In: *Carbon* 86 (2015), pp. 38–45. DOI: <https://doi.org/10.1016/j.carbon.2015.01.021>.

- [50] M. Shavelkina, P. Ivanov, A. Bocharov, and R. Amirov. *Distinctive Features of Graphene Synthesized in a Plasma Jet Created by a DC Plasma Torch*. 2020. DOI: <https://doi.org/10.3390/ma13071728>.
- [51] A. Mašláni, M. Hrabovský, P. Kreněk, M. Hlína, S. Raman, V. S. Sikarwar, and M. Jeremiáš. „Pyrolysis of methane via thermal steam plasma for the production of hydrogen and carbon black“. In: *International Journal of Hydrogen Energy* 46.2 (2021), pp. 1605–1614. DOI: <https://doi.org/10.1016/j.ijhydene.2020.10.105>.
- [52] Y. Y. Tanashev, V. I. Fedoseev, Y. I. Aristov, V. V. Pushkarev, L. B. Avdeeva, V. I. Zaikovskii, and V. N. Parmon. „Methane processing under microwave radiation: Recent findings and problems“. In: *Catalysis Today* 42.3 (1998), pp. 333–336. DOI: [https://doi.org/10.1016/S0920-5861\(98\)00110-2](https://doi.org/10.1016/S0920-5861(98)00110-2).
- [53] D. H. Lee, Y.-H. Song, K.-T. Kim, and J.-O. Lee. „Comparative Study of Methane Activation Process by Different Plasma Sources“. In: *Plasma Chemistry and Plasma Processing* 33.4 (2013), pp. 647–661. DOI: <https://doi.org/10.1007/s11090-013-9456-6>.
- [54] N. Shah, D. Panjala, and G. P. Huffman. „Hydrogen production by catalytic decomposition of methane“. In: *Energy & Fuels* 15.6 (2001), pp. 1528–1534. DOI: <https://doi.org/10.1021/ef0101964>.
- [55] A. Konieczny, K. Mondal, T. Wiltowski, and P. Dydo. „Catalyst development for thermocatalytic decomposition of methane to hydrogen“. In: *International Journal of Hydrogen Energy* 33.1 (2008), pp. 264–272. DOI: <https://doi.org/10.1016/j.ijhydene.2007.07.054>.
- [56] J. L. Pinilla, R. Utrilla, R. K. Karn, I. Suelves, M. J. Lázaro, R. Moliner, A. B. García, and J. N. Rouzaud. „High temperature iron-based catalysts for hydrogen and nanostructured carbon production by methane decomposition“. In: *International Journal of Hydrogen Energy* 36.13 (2011), pp. 7832–7843. DOI: <https://doi.org/10.1016/j.ijhydene.2011.01.184>.
- [57] A. E. Awadallah, A. A. Aboul-Enein, D. S. El-Desouki, and A. K. Aboul-Gheit. „Catalytic thermal decomposition of methane to CO<sub>x</sub>-free hydrogen and carbon nanotubes over MgO supported bimetallic group VIII catalysts“. In: *Applied Surface Science* 296 (2014), pp. 100–107. DOI: <https://doi.org/10.1016/j.apsusc.2014.01.055>.

- [58] M. Pudukudy and Z. Yaakob. „Methane decomposition over Ni, Co and Fe based monometallic catalysts supported on sol gel derived SiO<sub>2</sub> microflakes“. In: *Chemical Engineering Journal* 262 (2015), pp. 1009–1021. DOI: <https://doi.org/10.1016/j.cej.2014.10.077>.
- [59] M. Pudukudy, Z. Yaakob, M. Z. Mazuki, M. S. Takriff, and S. S. Jahaya. „One-pot sol-gel synthesis of MgO nanoparticles supported nickel and iron catalysts for undiluted methane decomposition into CO<sub>x</sub> free hydrogen and nanocarbon“. In: *Applied Catalysis B: Environmental* 218 (2017), pp. 298–316. DOI: <https://doi.org/10.1016/j.apcatb.2017.04.070>.
- [60] D. Torres, J. L. Pinilla, and I. Suelves. „Cobalt doping of  $\alpha$ -Fe/Al<sub>2</sub>O<sub>3</sub> catalysts for the production of hydrogen and high-quality carbon nanotubes by thermal decomposition of methane“. In: *International Journal of Hydrogen Energy* 45.38 (2020), pp. 19313–19323. DOI: <https://doi.org/10.1016/j.ijhydene.2020.05.104>.
- [61] International Biochar Initiative. *Standardized Product Definition and Product Testing Guidelines for Biochar That Is Used in Soil*. Tech. rep. November. 2015, p. 23.
- [62] A. D. Igalavithana et al. „Advances and future directions of biochar characterization methods and applications“. In: *Critical Reviews in Environmental Science and Technology* 47.23 (Dec. 2017), pp. 2275–2330. DOI: <https://doi.org/10.1080/10643389.2017.1421844>.
- [63] N. Kostoglou, A. Tarat, I. Walters, V. Ryzhkov, C. Tampaxis, G. Charalambopoulou, T. Steriotis, C. Mitterer, and C. Rebholz. „Few-layer graphene-like flakes derived by plasma treatment: A potential material for hydrogen adsorption and storage“. In: *Microporous and Mesoporous Materials* 225 (2016), pp. 482–487. DOI: <https://doi.org/10.1016/j.micromeso.2016.01.027>.
- [64] Z. Lin, E. Goikolea, A. Balducci, K. Naoi, P.-L. Taberna, M. Salanne, G. Yushin, and P. Simon. „Materials for supercapacitors: When Li-ion battery power is not enough“. In: *Materials today* 21.4 (2018), pp. 419–436. DOI: <https://doi.org/10.1016/j.mattod.2018.01.035>.
- [65] J. I. Goldstein, D. E. Newbury, J. R. Michael, N. W. M. Ritchie, J. H. J. Scott, and D. C. Joy. *Scanning electron microscopy and X-ray microanalysis*. Springer, 2017.
- [66] B. D. Cullity. *Elements of X-ray Diffraction*. Addison-Wesley Publishing, 1956.
- [67] E. Zolotoyabko. *Basic concepts of X-ray diffraction*. John Wiley & Sons, 2014.

- [68] H. Schnablegger and Y. Singh. *The SAXS guide: getting acquainted with the principles*. 2011, pp. 1–124.
- [69] O. Glatter and O. Kratky. *Small Angle X-ray Scattering*. London: Academic Press, 1982. DOI: <https://doi.org/10.1007/978-1-4757-6624-0>.
- [70] L. A. Feigin and D. I. Svergun. *Structure Analysis by Small-Angle X-ray and Neutron Scattering*. Vol. 1. Springer, 1987. DOI: <https://doi.org/10.1007/978-1-4757-6624-0>.
- [71] M. Szybowicz, A. B. Nowicka, and A. Dychalska. „Chapter 1 - Characterization of Carbon Nanomaterials by Raman Spectroscopy“. In: *Micro and Nano Technologies*. Ed. by S. Mohan Bhagyaraj, O. S. Oluwafemi, N. Kalarikkal, and S. B. T. C. o. N. Thomas. Woodhead Publishing, 2018, pp. 1–36. DOI: <https://doi.org/10.1016/B978-0-08-101973-3.00001-8>.
- [72] A. Ferrari and J. Robertson. „Interpretation of Raman spectra of disordered and amorphous carbon“. In: *Physical Review B - Condensed Matter and Materials Physics* 61.20 (2000), pp. 14095–14107. DOI: <https://doi.org/10.1103/PhysRevB.61.14095>.
- [73] A. C. Ferrari. „Raman spectroscopy of graphene and graphite: Disorder, electron-phonon coupling, doping and nonadiabatic effects“. In: *Solid state communications* 143.1-2 (2007), pp. 47–57. DOI: <https://doi.org/10.1016/j.ssc.2007.03.052>.
- [74] G. A. Zickler, B. Smarsly, N. Gierlinger, H. Peterlik, and O. Paris. „A reconsideration of the relationship between the crystallite size  $L_a$  of carbons determined by X-ray diffraction and Raman spectroscopy“. In: *Carbon* 44.15 (2006), pp. 3239–3246. DOI: <https://doi.org/10.1016/j.carbon.2006.06.029>.
- [75] M. Pawlyta, J.-N. Rouzaud, and S. Duber. „Raman microspectroscopy characterization of carbon blacks: Spectral analysis and structural information“. In: *Carbon* 84 (2015), pp. 479–490. DOI: <https://doi.org/10.1016/j.carbon.2014.12.030>.
- [76] A. Eckmann, A. Felten, A. Mishchenko, L. Britnell, R. Krupke, K. S. Novoselov, and C. Casiraghi. „Probing the nature of defects in graphene by Raman spectroscopy“. In: *Nano letters* 12.8 (2012), pp. 3925–3930. DOI: <https://doi.org/10.1021/nl300901a>.
- [77] Y. Wang, D. C. Alsmeyer, and R. L. McCreery. „Raman spectroscopy of carbon materials: structural basis of observed spectra“. In: *Chemistry of Materials* 2.5 (1990), pp. 557–563. DOI: <https://doi.org/10.1021/cm00011a018>.

- [78] O. Beyssac, B. Goffé, J.-P. Petitet, E. Froigneux, M. Moreau, and J.-N. Rouzaud. „On the characterization of disordered and heterogeneous carbonaceous materials by Raman spectroscopy“. In: *Spectrochimica Acta Part A: Molecular and Biomolecular Spectroscopy* 59.10 (2003), pp. 2267–2276. DOI: [https://doi.org/10.1016/S1386-1425\(03\)00070-2](https://doi.org/10.1016/S1386-1425(03)00070-2).
- [79] A. Cuesta, P. Dhamelinourt, J. Laureyns, A. Martinez-Alonso, and J. M. D. Tascón. „Raman microprobe studies on carbon materials“. In: *Carbon* 32.8 (1994), pp. 1523–1532. DOI: [https://doi.org/10.1016/0008-6223\(94\)90148-1](https://doi.org/10.1016/0008-6223(94)90148-1).
- [80] F. Tuinstra and J. L. Koenig. „Raman Spectrum of Graphite“. In: *The Journal of Chemical Physics* 53.3 (Aug. 1970), pp. 1126–1130. DOI: <https://doi.org/10.1063/1.1674108>.
- [81] M. Thommes, K. Kaneko, A. V. Neimark, J. P. Olivier, F. Rodriguez-Reinoso, J. Rouquerol, and K. S. W. Sing. „Physisorption of gases, with special reference to the evaluation of surface area and pore size distribution (IUPAC Technical Report)“. In: *Pure and applied chemistry* 87.9-10 (2015), pp. 1051–1069. DOI: <https://doi.org/10.1515/pac-2014-1117>.
- [82] N. Kostoglou et al. „Novel combustion synthesis of carbon foam aluminum fluoride nanocomposite materials“. In: 144 (2018), pp. 222–228. DOI: <https://doi.org/10.1016/j.matdes.2018.02.021>.
- [83] P. A. Monson. „Understanding adsorption/desorption hysteresis for fluids in mesoporous materials using simple molecular models and classical density functional theory“. In: *Microporous and Mesoporous Materials* 160 (2012), pp. 47–66. DOI: <https://doi.org/10.1016/j.micromeso.2012.04.043>.
- [84] J. D. Menczel, L. Judovits, R. B. Prime, H. E. Bair, M. Reading, and S. Swier. „Differential scanning calorimetry (DSC)“. In: *Thermal analysis of polymers: Fundamentals and applications* (2009), pp. 7–239.
- [85] R. B. Prime, H. E. Bair, S. Vyazovkin, P. K. Gallagher, and A. Riga. „Thermogravimetric Analysis (TGA)“. In: *Thermal Analysis of Polymers*. Wiley Online Books. Apr. 2009, pp. 241–317. DOI: <https://doi.org/10.1002/9780470423837.ch3>.
- [86] O. Paris, C. Zollfrank, and G. A. Zickler. „Decomposition and carbonisation of wood biopolymers - A microstructural study of softwood pyrolysis“. In: *Carbon* 43.1 (2005), pp. 53–66. DOI: <https://doi.org/10.1016/j.carbon.2004.08.034>.

- [87] T. N. Blanton, T. C. Huang, H. Toraya, C. R. Hubbard, S. B. Robie, D. Louer, H. E. Göbel, G. Will, R. Gilles, and T. Raftery. „JCPDS-International Centre for Diffraction Data round robin study of silver behenate. A possible low-angle X-ray diffraction calibration standard“. In: *Powder Diffraction* 10.2 (1995), pp. 91–95. DOI: <https://doi.org/10.1017/S0885715600014421>.
- [88] D. S. Knight and W. B. White. „Characterization of diamond films by Raman spectroscopy“. In: *Journal of Materials Research* 4.2 (1989), pp. 385–393. DOI: <https://doi.org/10.1557/JMR.1989.0385>.
- [89] M. J. Matthews, M. A. Pimenta, G. Dresselhaus, M. S. Dresselhaus, and M. Endo. „Origin of dispersive effects of the Raman D band in carbon materials“. In: *Physical Review B* 59.10 (1999), R6585. DOI: <https://doi.org/10.1103/PhysRevB.59.R6585>.
- [90] A. Sadezky, H. Muckenhuber, H. Grothe, R. Niessner, and U. Pöschl. „Raman microspectroscopy of soot and related carbonaceous materials: spectral analysis and structural information“. In: *Carbon* 43.8 (2005), pp. 1731–1742. DOI: <https://doi.org/10.1016/j.carbon.2005.02.018>.
- [91] M. P. Allen and D. J. Tildesley. *Computer Simulation of Liquids*. Oxford University Press, 2017.
- [92] C. L. Barrie, P. C. Griffiths, R. J. Abbott, I. Grillo, E. Kudryashov, and C. Smyth. „Rheology of aqueous carbon black dispersions“. In: *Journal of colloid and interface science* 272.1 (2004), pp. 210–217. DOI: <https://doi.org/10.1016/j.jcis.2003.12.004>.
- [93] S. Stankovich, R. D. Piner, X. Chen, N. Wu, S. T. Nguyen, and R. S. Ruoff. „Stable aqueous dispersions of graphitic nanoplatelets via the reduction of exfoliated graphite oxide in the presence of poly (sodium 4-styrenesulfonate)“. In: *Journal of Materials Chemistry* 16.2 (2006), pp. 155–158. DOI: <https://doi.org/10.1039/b512799h>.
- [94] S. Tanvir, S. Biswas, and L. Qiao. „Evaporation characteristics of ethanol droplets containing graphite nanoparticles under infrared radiation“. In: *International Journal of Heat and Mass Transfer* 114 (2017), pp. 541–549. DOI: <https://doi.org/10.1016/j.ijheatmasstransfer.2017.06.059>.
- [95] D. E. Newbury and N. W. M. Ritchie. „Is scanning electron microscopy/energy dispersive X-ray spectrometry (SEM/EDS) quantitative?“ In: *Scanning* 35.3 (2013), pp. 141–168. DOI: <https://doi.org/10.1002/sca.21041>.

- [96] C. E. Brewer. „Biochar characterization and engineering“. PhD thesis. Iowa State University, 2012.
- [97] N. M. Jaafar, P. L. Clode, and L. K. Abbott. „Microscopy observations of habitable space in biochar for colonization by fungal hyphae from soil“. In: *Journal of Integrative Agriculture* 13.3 (2014), pp. 483–490. DOI: [https://doi.org/10.1016/S2095-3119\(13\)60703-0](https://doi.org/10.1016/S2095-3119(13)60703-0).
- [98] P. A. Tipler. *Physics for Scientists and Engineers*. Third Edit. New York: Worth Publishers Inc., 1991.
- [99] D. Y. Kim, C.-M. Yang, Y. S. Park, K. K. Kim, S. Y. Jeong, J. H. Han, and Y. H. Lee. „Characterization of thin multi-walled carbon nanotubes synthesized by catalytic chemical vapor deposition“. In: *Chemical Physics Letters* 413.1 (2005), pp. 135–141. DOI: <https://doi.org/10.1016/j.cplett.2005.07.064>.
- [100] D.-Y. Kim, Y. S. Yun, S.-M. Kwon, and H.-J. Jin. „Preparation of Aspect Ratio-Controlled Carbon Nanotubes“. In: *Molecular Crystals and Liquid Crystals* 510.1 (Sept. 2009), pp. 79–86. DOI: <https://doi.org/10.1080/15421400903058338>.
- [101] J. H. Lehman, M. Terrones, E. Mansfield, K. E. Hurst, and V. Meunier. „Evaluating the characteristics of multiwall carbon nanotubes“. In: *Carbon* 49.8 (2011), pp. 2581–2602. DOI: <https://doi.org/10.1016/j.carbon.2011.03.028>.
- [102] N. Kostoglou, C. Tampaxis, G. Charalambopoulou, G. Constantinides, V. Ryzhkov, C. Doumanidis, B. Matovic, C. Mitterer, and C. Rebholz. *Boron Nitride Nanotubes Versus Carbon Nanotubes: A Thermal Stability and Oxidation Behavior Study*. 2020. DOI: <https://doi.org/10.3390/nano10122435>.
- [103] O. M. Dunens, K. J. MacKenzie, and A. T. Harris. „Synthesis of Multiwalled Carbon Nanotubes on Fly Ash Derived Catalysts“. In: *Environmental Science & Technology* 43.20 (Oct. 2009), pp. 7889–7894. DOI: <https://doi.org/10.1021/es901779c>.
- [104] D. M. Crumpton, R. A. Laitinen, J. Smieja, and D. A. Cleary. „Thermal analysis of carbon allotropes: an experiment for advanced undergraduates“. In: *Journal of chemical education* 73.6 (1996), p. 590. DOI: <https://doi.org/10.1021/ed073p590>.
- [105] F. Rodriguez-Reinoso, J. de D. Lopez-Gonzalez, and C. Berenguer. „Activated carbons from almond shells-I: Preparation and characterization by nitrogen adsorption“. In: *Carbon* 20.6 (1982), pp. 513–518. DOI: [https://doi.org/10.1016/0008-6223\(82\)90088-4](https://doi.org/10.1016/0008-6223(82)90088-4).



- [106] H. de Jonge and M. C. Mittelmeijer-Hazeleger. „Adsorption of CO<sub>2</sub> and N<sub>2</sub> on Soil Organic Matter: Nature of Porosity, Surface Area, and Diffusion Mechanisms“. In: *Environmental Science & Technology* 30.2 (Jan. 1996), pp. 408–413. DOI: <https://doi.org/10.1021/es950043t>.
- [107] S. Dantas, K. C. Struckhoff, M. Thommes, and A. V. Neimark. „Pore size characterization of micro-mesoporous carbons using CO<sub>2</sub> adsorption“. In: *Carbon* 173 (2021), pp. 842–848. DOI: <https://doi.org/10.1016/j.carbon.2020.11.059>.
- [108] C. E. Brewer, V. J. Chuang, C. A. Masiello, H. Gonnermann, X. Gao, B. Dugan, L. E. Driver, P. Panzacchi, K. Zygourakis, and C. A. Davies. „New approaches to measuring biochar density and porosity“. In: *Biomass and Bioenergy* 66 (2014), pp. 176–185. DOI: <https://doi.org/10.1016/j.biombioe.2014.03.059>.
- [109] P. I. Ravikovitch, A. Vishnyakov, R. Russo, and A. V. Neimark. „Unified approach to pore size characterization of microporous carbonaceous materials from N<sub>2</sub>, Ar, and CO<sub>2</sub> adsorption isotherms“. In: *Langmuir* 16.5 (2000), pp. 2311–2320. DOI: <https://doi.org/10.1021/1a991011c>.
- [110] S. J. Gregg, K. S. W. Sing, and H. W. Salzberg. *Adsorption, Surface Area and Porosity*. Vol. 114. 11. IOP Publishing, 1967, p. 279C.
- [111] K. C. Kim, T.-U. Yoon, and Y.-S. Bae. „Applicability of using CO<sub>2</sub> adsorption isotherms to determine BET surface areas of microporous materials“. In: *Microporous and Mesoporous Materials* 224 (2016), pp. 294–301. DOI: <https://doi.org/10.1016/j.micromeso.2016.01.003>.
- [112] R. Guil-Lopez, J. A. Botas, J. L. G. Fierro, and D. P. Serrano. „Comparison of metal and carbon catalysts for hydrogen production by methane decomposition“. In: *Applied Catalysis A: General* 396.1-2 (2011), pp. 40–51. DOI: <https://doi.org/10.1016/j.apcata.2011.01.036>.
- [113] V. I. Zaikovskii, V. V. Chesnokov, and R. A. Buyanov. „The Relationship between the State of Active Species in a Ni/Al<sub>2</sub>O<sub>3</sub>Catalyst and the Mechanism of Growth of Filamentous Carbon“. In: *Kinetics and catalysis* 42.6 (2001), pp. 813–820. DOI: <https://doi.org/10.1023/A:1013235300777>.
- [114] T. V. Reshetenko, L. B. Avdeeva, Z. R. Ismagilov, A. L. Chuvilin, and V. A. Ushakov. „Carbon capacious Ni-Cu-Al<sub>2</sub>O<sub>3</sub> catalysts for high-temperature methane decomposition“. In: *Applied Catalysis A: General* 247.1 (2003), pp. 51–63. DOI: [https://doi.org/10.1016/S0926-860X\(03\)00080-2](https://doi.org/10.1016/S0926-860X(03)00080-2).

- [115] M. N. Uddin, W. M. A. W. Daud, and H. F. Abbas. „Co-production of hydrogen and carbon nanofibers from methane decomposition over zeolite Y supported Ni catalysts“. In: *Energy Conversion and Management* 90 (2015), pp. 218–229. DOI: <https://doi.org/10.1016/j.enconman.2014.10.060>.
- [116] A. C. Lua and H. Y. Wang. „Hydrogen production by catalytic decomposition of methane over Ni-Cu-Co alloy particles“. In: *Applied Catalysis B: Environmental* 156 (2014), pp. 84–93. DOI: <https://doi.org/10.1016/j.apcatb.2014.02.046>.
- [117] J. D. Andrade. „X-ray Photoelectron Spectroscopy (XPS)“. In: *Surface and Interfacial Aspects of Biomedical Polymers*. Ed. by J. D. Andrade. Boston, MA: Springer, 1985. Chap. X-ray Phot, pp. 105–195. DOI: <https://doi.org/10.1007/978-1-4684-8610-0>.
- [118] J. W. Olesik. „Elemental analysis using ICP-OES and ICP/MS“. In: *Analytical Chemistry* 63.1 (Jan. 1991), 12A–21A. DOI: <https://doi.org/10.1021/ac00001a001>.
- [119] F. Schüth, K. S. W. Sing, and J. Weitkamp. *Handbook of Porous Solids*. Vol. 4. Wiley-VCH, 2002.
- [120] C. Bouchelta, M. S. Medjram, O. Bertrand, and J.-P. Bellat. „Preparation and characterization of activated carbon from date stones by physical activation with steam“. In: *Journal of Analytical and Applied Pyrolysis* 82.1 (2008), pp. 70–77. DOI: <https://doi.org/10.1016/j.jaap.2007.12.009>.